ACTIVE INTEGRATED MIMO ANTENNA DESIGN

BY

SAGAR KUMAR DHAR

A Thesis Presented to the
DEANSHIP OF GRADUATE STUDIES

KING FAHD UNIVERSITY OF PETROLEUM & MINERALS

DHAHRAN, SAUDI ARABIA

In Partial Fulfillment of the
Requirements for the Degree of

MASTER OF SCIENCE

In

ELECTRICAL ENGINEERING

MARCH 2015

KING FAHD UNIVERSITY OF PETROLEUM & MINERALS
DHAHRAN 31261, SAUDI ARABIA

DEANSHIP OF GRADUATE STUDIES

This thesis, written by **SAGAR KUMAR DHAR** under the direction of his thesis adviser and approved by his thesis committee, has been presented to and accepted by the Dean of Graduate Studies, in partial fulfillment of the requirements for the degree of **MASTER OF SCIENCE IN ELECTRICAL ENGINEERING**.

Thesis Committee

Dr. Mohammad S. Sharawi (Adviser)

Dr. (Co-adviser)

Shikh Sharif
Dr. Sheikh Sharif Iqbal (Member)

Dr. Oualid Hammi (Member)

Dr. (Member)

3/3/15
Dr. Ali Ahmad Al-Shaikhi
Department Chairman

Dr. Salam A. Zummo
Dean of Graduate Studies

15/3/15
Date

To My Best Friends Mitu, Bijoy and Bappu.

ACKNOWLEDGMENTS

While writing this acknowledgment, I realize that the work in my hand could have never been finished without the help of numerous friends and colleagues. I want to express my gratitude to all of you who made this thesis possible.

I am heartily thankful to my Supervisor, Dr. Mohammad. S. Sharawi, for his invaluable suggestions, encouragement, time and support. It was quite an excellent experience to work under his supervision and I like to mention the optimistic approach he always tries to pass to us. It was quite a fascinating learning experience. I am delighted to be a part of his research group- Antennas and Microwave Structure Design Lab (AMSDL). Without the resources of AMSDL, it was not possible to complete this thesis work.

I am thankful to Dr. Sheikh S. Iqbal and Dr. Oualid Hammi for their valuable comments and discussions. Without their critics, it was difficult to address different aspects of my thesis work.

Special thanks to my AMSDL group members Dr. Umar Khan and Dr. Rifaqat Hussain. I can remember their time in helping me during my first fabrication process at AMSDL. Without their help and experience, it would have been difficult to master the experimental process involved in my thesis work and to *finish my work timely. I am heartily thankful also to Mr. Sameir Deif for his cordial cooperation from the very beginning of my time at AMSDL. Thanks to all other AMSDL group members for their encouragement and expectations which kept me motivated towards my work.*

I would also like to acknowledge the resource and support by the Electrical Engineering Department, KFUPM. Special thanks to Mr. Amjad and Mr. Irfan, Lab Engineers, for their cordial cooperation.

Finally and most importantly, I would like to thank my friends Mitu, Bijoy, Bappu, Saikat and Shuvashis for their perpetual support towards my work. Without their endless encouragement, it was so difficult to keep me motivated towards my work. Every time, I feel so lucky to have such good friends.

Last, I offer my thanks and regards to all of those, not mentioned by name, who supported me in any aspect during the completion of this thesis work.

TABLE OF CONTENTS

LIST OF TABLES

LIST OF FIGURES

THESIS ABSTRACT

NAME:	Sagar Kumar Dhar
TITLE OF STUDY:	Active Integrated MIMO Antenna Design
MAJOR FIELD:	Electrical Engineering
DATE OF DEGREE:	March, 2015

Printed multiple-input-multiple-output (MIMO) antennas are of significant interest and are highly demanded because of their exotic features like providing high data throughput, better transmission quality and increased coverage due to its spatial multiplexing gain, diversity gain and array gain. Following the recent trends of communication technology, it is obvious that MIMO antennas are not only predominant in today's 4G radio systems, they are also going to be adopted in future 5G radio systems. However, designing printed MIMO antennas incorporates a lot of parameters like size, gain, efficiency, bandwidth, isolation, envelop correlation coefficient (ECC) and so on. These parameters are highly inter-related and fierce trade-offs exist among them which makes MIMO antenna design very challenging. In this work, an ultra-wideband (UWB) active integrated MIMO antenna is presented. A new approach of port isolation is introduced by the integration and *co-design of the radio frequency (RF) amplifier with the passive antennas. Better antenna performance in terms of matching, gain and efficiency is achieved through such active integrated antenna (AIA) approach. The features of this AIA approach are investigated with a patch and a semi-ring MIMO antenna for narrowband, wideband and ultrawideband scenarios.*

Initially, the features of antena miniaturization are investigated with a patch antenna through co-design with RF amplifiers. This approach relaxes the standalone antenna matching requirement which is of interest in miniaturized antenna designs. The amplifiers and the antennas are co-designed so that optimum performance is achieved concurrently in terms of gain, noise figure and efficiency. The antenna has the size of $0.033\lambda_0^2$ *at 2.45 GHz where* λ_0 *is the free space wavelength at 2.45 GHz. It is miniaturized from its natural resonance frequency of 3.5 GHz to 2.45 GHz which provides 51% of size reduction.*

A feasibility study of bandwidth enhancement of a narrowband MIMO antenna using simplified real frequency technique (SRFT) is presented. It is observed that the SRFT (although can be used to design wideband matching network) cannot improve the bandwidth of a narrow band structure.

Finally, improvement of port isolation of MIMO antennas through the integration of active devices (RF amplifier) is presented. Thus, a UWB two-element MIMO antenna geometry is presented. Each element of the MIMO antenna system has the size of $12 \times 24mm^2$ *on a substrate of* $90 \times 50mm^2$ *which is suitable for standard mobile terminals. Then, the MIMO antenna is co-designed with an RF amplifier* *as a transmitting front-end which brings a port isolation improvement of 7 dB. Better antenna matching and consequently, improved efficiency and gain of the antenna are observed. Both simulation and measurement results are presented which are in well agreement.*

مُلخّص الرسالة

الاسم الكامل: شاغر كومار دار

عنوان الدراسة: الهوائيات المدمجة ذات المنافذ المتعددة

التخصص: الهندسة الكهربائية

تاريخ الدرجة العلمية: مارس 2015

تعتبر الهوائيات المطبوعة ذات المنافذ المتعددة (MIMO) من أنواع الهوائيات المهمة لخصائصها المتميزة، مثل معدلات نقل البيانات العالية، جودة الإرسال والتغطية الأشمل. إن المتابع لأنظمة الاتصالات الحديثة، يلاحظ أن هوائيات MIMO ليست فقط منتشرة في الجيل الحالي من أجهزة الاتصالات (الجيل الرابع 4G) بل ويتوقع أن تنتشر بصورة أكبر في الجيل القادم (الجيل الخامس 5G) . إن تصميم هوائيات (MIMO) يحتاج إلى موازنة عدد من خواص الهوائي مثل: الحجم، الكسب، الكفاءة، عرض النطاق ومعامل ترابط أنماط البث لعناصر الهوائية. إن العوامل المذكورة آنفا ترتبط فيما بينها ارتباطا وثيقا، يتطلب من مصمم الهوائي المفاضلة فيما بينها، مما يعقد عملية التصميم.

هذه الأطروحة تقدم هوائيا ذا نطاق عريض جدا (UWB) من نوع (MIMO). كما وتتضمن الأطروحة طريقة جديدة لعزل منافذ الهوائي بدمج المضخم (RF-Amplifier) والهوائي. باستخدام هذا الدمج نتحصل على خصائص أفضل للنظام مثل الموائمة (matching) و الكسب (gain) و الكفاءة (efficiency). أيضا نقدم دراسة لخصائص عملية الدمج من خلال نموذجين من هوائيات MIMO: هوائي patch وهوائي نصف دائري للنطاقات الضيقة والعريضة بالإضافة إلى النطاقات العريضة جدا.

هذه الأطروحة تقدم أيضا دراسة لعملية تصغير الهوائيات (miniaturization) من خلال دمج تصميم المضخم والهوائية. يقلل هذا التصميم من دقة متطلبات الموائمة بين الهوائي والمضخم مما يسهل تصميم هوائيات أصغر. يتم تصميم الهوائيات والمضخمات بحيث يتم الحصول على أفضل كسب وكفاءة ومعامل ضجيج في نفس الوقت. حجم الهوائي المصمم هو 0.033 من الطول الموجي عند تردد 2.45 جيجا هرتز. تم تصغير الهوائي من تردده الأصلي عند 3.54 جيجا هرتز إلى 2.45 جيجا هرتز مما وفر تصغيرا بمقدار 51%.

تقدم هذه الأطروحة أيضا دارسة لإمكانية تحسين عرض النطاق لهوائي MIMO ذا نطاق ضيق باستخدام طريقة (SRFT). وخلصت الدراسة إلى أن طريقة (SRFT) تصلح للهوائيات ذات النطاق العريض بينما لا يمكن بواسطتها تحسين النطاق لهوائيات ذات نطاق ضيق ابتداء.

أخيرا تتطرق الاطروحة لدراسة تحسين عزل المنافذ لهوائيات MIMO من خلال دمجها مع المضخمات. لذلك تم عرض تصميم لهوائي مكون من عنصرين لهما نطاق عريض. يشغل كل عنصر حيزا مقداره 12×24 مم مربع على لوح دارة مساحته 90×50 مم مربع مما يجعله مناسبا للهواتف المحمولة الحديثة. تتم عملية تصميم هوائي MIMO بالترافق مع تصميم المضخم مما يؤدي إلى تحسن عزل المنافذ بمقدار 7dB. تم ملاحظة تحسن في المواءمة للهوائي وبالتالي في الأداء والكسب. تم عرض جميع النتائج والتي تظهر توافقا بين نتائج المحاكاة النموذجية ونتائج القياسات المعملية.

CHAPTER 1

INTRODUCTION

Wireless mobile communication has a remarkable history that is more than a century of technological innovations which was ignited by the first demonstration by *Sir J. C. Bose* in 1895 [1] and thrived through the transatlantic transmission by *G. Marconi* in 1899. Wireless technology, the most pervasive core technology, has become the integral part of modern life for varieties of computing and applications ranging from third/fourth generation (3G/4G) wireless devices, broadband access, embedded sensors, radio frequency identification (RFID) and many others. However, the field of information and communication technology is currently undergoing a fundamental transformation from the era of personal computers and wired internet services to a new paradigm based on portable devices connecting wireless devices to the emerging mobile network.

Mobile data services are currently experiencing rapid growth because of the popularity of internet applications on massive mobile users through smartphones, tablets, netbooks and laptops. According to a report by Cisco, it is predicted that the mobile generated traffic will exceed that of the fixed personal computers by 2015. This forecasts the fact that most information and communication services are expected to migrate to the mobile devices by the next few years. On the other hand, such shift in paradigm inevitably calls for the large scale delivery of internet applications on mobile devices which will require faster radio access bit rates, improved spectrum efficiency, robustness and so on [2]. One of the enabling technologies is multiple-input-multiple-output (MIMO) [3, 4]. Moreover, for sake of mobility, miniaturization of wireless devices is crucial which inevitably calls for miniaturization of antennas (the largest part in any RF system). Considering all these requirements and concerns, active integrated antennas (AIAs) are investigated in this work. AIAs refer to the antennas intimately designed/integrated with active elements so that performance improvement can be achieved. In this work, the target application was in the range of 1.8-6GHz for mobile hand-held devices. Improvment of different fundamental limits like size, bandwidth and port isolation of passive antennas are mainly investigated through active integration in narrowband, wideband and ultra-wideband scenarios. Detailed procedures of simulation, implementation and measurements are presented.

1.1 Wireless Communication Evolution

Wireless communication implies transfer of information between two or more points that are not connected by an electrical conductor. Over the past decade, wireless communications had thrived remarkably from 2G to 4G. A roadmap of wireless communications is described in [2] which follows up the evolution in four layers: radio hardware technology, wireless physical layer technologies, network protocols, and software and applications. At the hardware level, a proliferation of wireless devices has happened through the evolution of 2G, 3G, 4G, Wi-Fi, Bluetooth and recently cognitive radio. Moving to the network protocol, the trend of wireless communications has been more internet protocol (IP) based as in 4G systems such as long term evolution(LTE). The Wi-Fi technology that started with limited coverage has extended to the ad-hoc and mesh networking protocols for wide area outdoor deployments. At the mobile system and application levels, an evolution from early 3G cellular, WLAN and personal area network to public WLAN and mesh, ad hoc, peer to peer (P2P) and sensor network applications has been observed. Finally, in terms of radio physical layer, the cellular radio link speed has increased from about 2Mbps with early 3G systems in the year of 2000 to 100Mbps with 4G (LTE and WiMax) systems using MIMO technology. Similarly, short range WLAN speed is expected to be 1Gbps in the next few years compared to 11Mbps in the year 2000. The Moore's law for wireless communication is shown in Fig. 1.1 which shows the exponential increase in both WLAN and Cellular data speed where most prospective radio technology is expected to be based on MIMO [2]-[4].

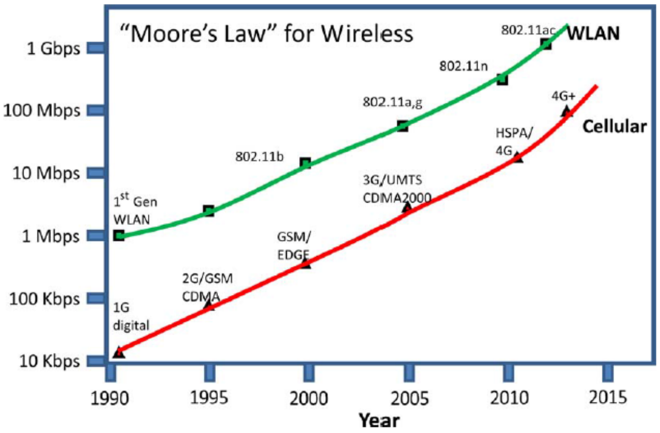

Figure 1.1: Wireless access speed. [2]

1.2 Multiple Antenna Technology

Due to the requirement of high data throughput and reliability within a limited spectrum, multiple antenna technologies are getting popular day by day. There are different approaches of multiple antenna technology like single-input-multiple-output (SIMO), multiple-input-single-output (MISO) and multiple-input-multiple-output (MIMO). A generic system diagram of multiple antenna technologies is shown in Fig. 1.2. In SIMO, a signal transmitted by a single antenna is received through several antennas that provides receiver diversity, in other words, improves the performance under fading. Such a system although cannot increase the data speed directly, can work under low signal-to-noise ratio (SNR). Similarly, in MISO, which is commonly referred to a transmit diversity system, the same signal is sent on multiple transmitting antennas but is coded in such a way that the receiver can identify each transmitter. Transmit diversity makes the signal more resistant to fading and can improve performance under

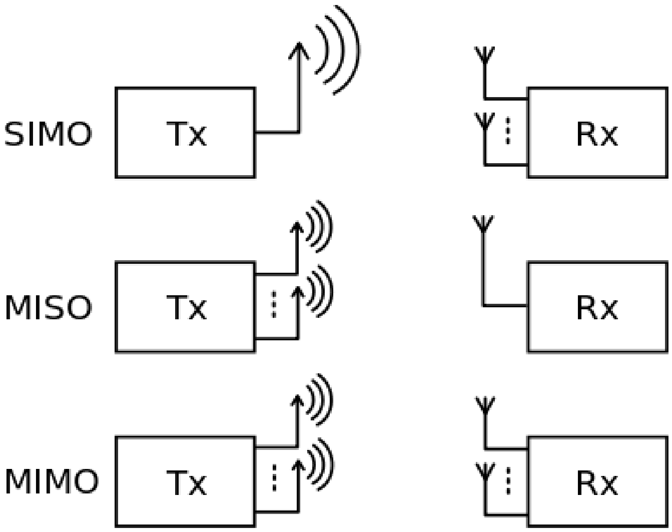

Figure 1.2: Multiple antenna technologies.

low SNR. Again, this technique does not directly increase data rates but rather supports current data rates with less power and or SNR.

On the other hand, multiple transmitting and receiving antennas are used in MIMO technology although it is not a straightforward superposition of MISO and SIMO since different data at the same frequency and time are transferred. In MIMO, multiple data streams are transmitted through multiple antennas and are received and decoded using MIMO algorithms which provides higher data rate with reliability at the cost higher computational power and complexity. Definitely, MIMO uses spatial diversity as a key to higher data throughput. The increase in channel capacity with respect to the transmitting and receiving antenna can be expressed as in (1.1) where N is the number of antennas, and B is the bandwidth. The capacity variation with respect to the number of MIMO antennas is shown in Fig. 1.3. It can be seen that if the number of transmitting/receiving antenna N is increased, the channel capacity can be increased proportionally keeping other parameters fixed. However, the cost of the increased data rates is the computational power, complexity, transmitting power over multiple antennas and the size occupied by multiple antennas for MIMO. Again, from a system point of view, it is not MIMO which just incurs multiple antennas both in transmitter and receiver but it is necessary to have ideally uncorrelated wireless channels to have the ideal capacity increase illustrated in Fig. 1.3. In practice, the antennas are required to be designed such that they can provide the spatial diversity required by the MIMO system which is generally ensured by high isolation and low correlation coefficient.

$$C = NB\log_2(1 + SNR) \tag{1.1}$$

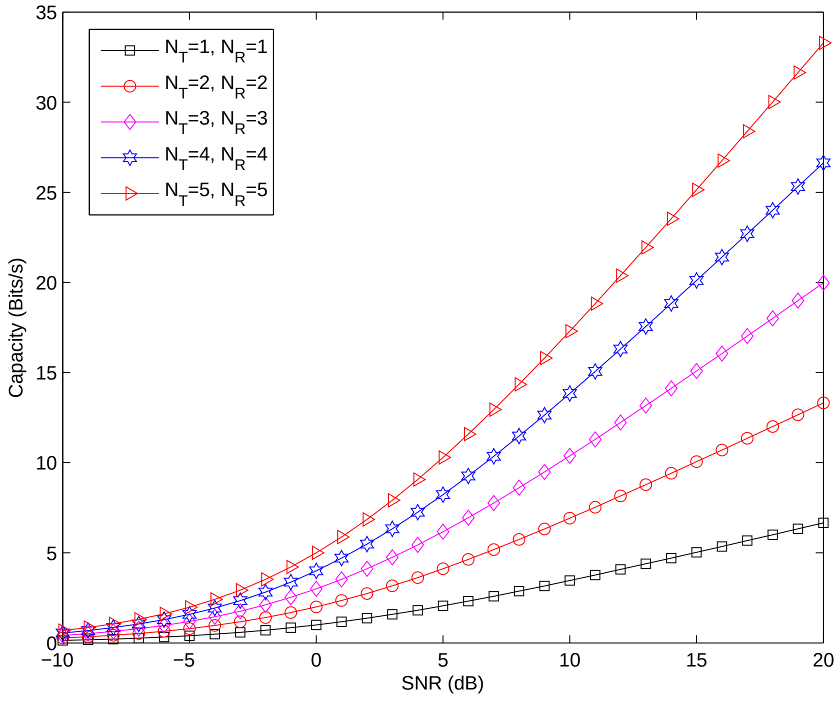

Figure 1.3: Illustration of capacity increase in MIMO.

1.3 Active Integrated Antenna (AIA)

In general, AIA refers to the antennas intimately integrated with active devices so that performance enhancement of passive antennas can be achieved. As shown in Fig. 1.4, active circuits and the antenna are part of each other and are to be designed together as a whole unit in a true AIA. So, neither the antenna nor the active circuits need to be designed for 50 Ω except at the AIA input/output port. The first AIA (although not truly integrated/co-designed) was proposed in 1928 when a small antenna with electron tube was used for radio broadcast receivers around 1MHz [5]. In 1960s and 1970s, due to the invention of high frequency transistors, AIA thrived and got more attention because of its some possible features anticipated in [6]-[8] like:

- Increasing the effective length for short antennas (antenna miniaturization).
- Increasing the bandwidth.
- Improving the noise factors.
- Improving the gain of the antenna.

1.4 Motivation

Portability, high data throughput and small size are the key driving factors of modern wireless communication devices. In addition, multiband/wideband operation is highly desirable for multitasking and covering different wireless standards.

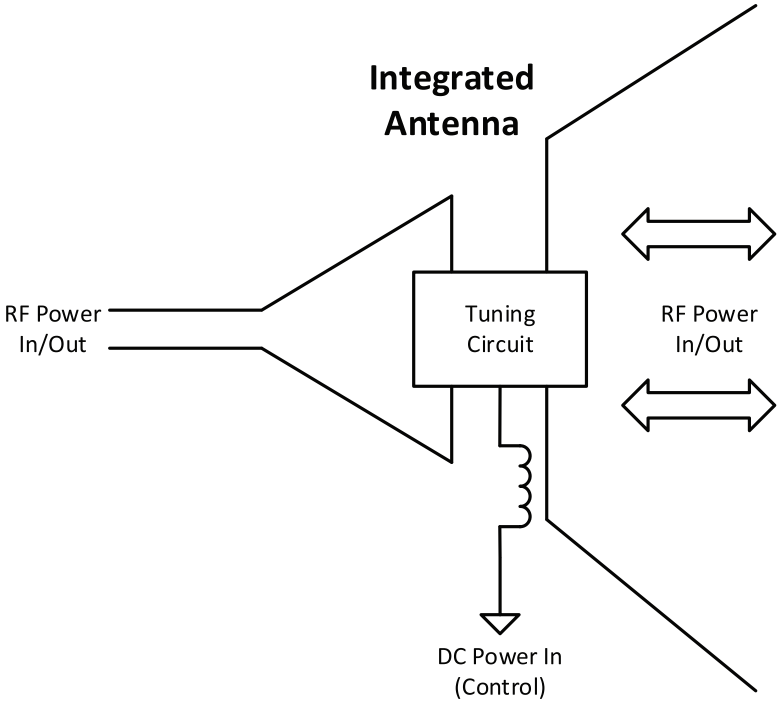

Figure 1.4: Active integrated antenna.

Considering these requirements, compact multiband/wideband MIMO antennas are of interest. However, MIMO antennas require multiple antenna elements and it is challenging to find the space for multiple elements in modern compact mobile devices. Moreover, trade-offs among different antenna parameters especially size, bandwidth, gain, isolation and correlation coefficient exist [9]. For example, if the size of an antenna is reduced, bandwidth, gain, isolation and correlation coefficient are affected unless some techniques are used to mitigate the trade-offs. Thus, designing multiband/wideband compact MIMO antennas are highly challenging and desirable.

A simplified RF front-end block diagram is shown in Fig. 1.5. A duplexer is generally used to provide isolation or selection of transmitting and receiving path which is not shown in Figure 1.6 for simplicity. In typical RF systems, the amplifiers and the antenna are individually matched to 50 Ω. However, an antenna design calls for enormous computational (simulation) efforts since a closed form relation among different structure parameters rarely exists. Thus, a systematic design procedure for reducing antenna design steps is highly appreciated.

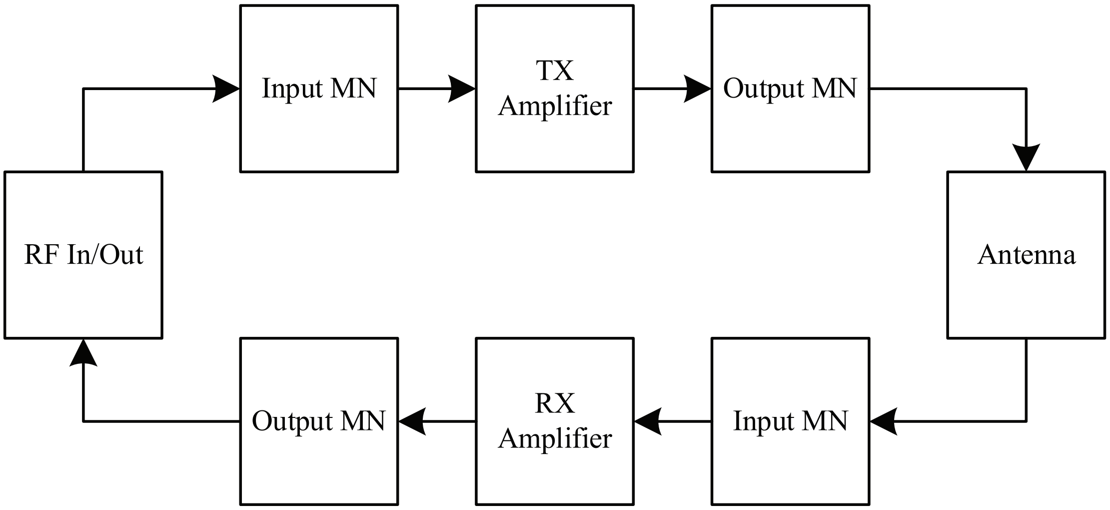

Figure 1.5: RF front-end block diagram.

Following Moore's law over the past several decades, electronic devices are getting miniaturized seamlessly. Although, problems due to reduced transistor length such as lower intrinsic gain and other different short channel effects like threshold voltage variation and mobility degradation are introduced [10], smart circuit techniques are figured out for mitigating short channel effects. RF transceivers in 90 nm and 32 nm technology operating in 2.4 GHz WLAN are presented in [11],[12] where the maximum chip size occupied was 15.5 mm^2 in 90 nm technology whereas a typical single element antenna size in 2.4 GHz band will occupy around 24×24 mm^2 with good gain and bandwidth [13]. For MIMO antenna systems, the size will be more than two times including the separation between antenna elements which is required for better correlation coefficient value. Thus, antenna miniaturization is of uttermost importance. There are different techniques for antenna miniaturization in literature like bending, folding and meandering, but, miniaturized antennas possess high quality factor and difficulties are often faced when matching such miniaturized antennas to the following RF subsystems. In this regard, antenna miniaturization along with their matching procedures is of high interest to antenna and system designers.

Considering all these concerns and challenges, AIAs are investigated in this work as a prospective solution for antenna miniaturization, matching and port isolation in MIMO antenna systems.

1.5 Thesis Contributions

In this work, different prospects of AIAs are investigated. Detailed design procedures, simulation and experimental results are presented. The thesis contributions can be listed as follows:

1. A generic technique of antenna miniaturization is investigated. The miniaturization of antenna is achieved through the co-design of antenna and amplifier. Instead of 50 Ω, both the amplifier and antenna are designed together so that conjugate matching at the desired frequency is achieved which in other words provides antenna miniaturization. The concept is examined in narrowband and wideband scenarios for both transmitting and receiving RF

systems. One most important feature of such miniaturization technique is that it can be equally applicable for any sort of structure since it depends on its port characteristics.

2. A study on the feasibility of bandwidth enhancement of passive antennas using the simplified real frequency technique (SRFT) is conducted. The technique is presented with different loads having low and high quality factors.

3. A UWB two element MIMO antenna covering 1.8-10.6 GHz is designed. Analysis and measurement results are presented. The antenna occupies a substrate size of $90 \times 50mm^2$ with good characteristics having each antenna element of $12 \times 24mm^2$. Such antennas are suitable for integrated communication and UWB sensor applications.

4. The concept of active integrated MIMO antenna is presented which has not appeared before in the literature. The concept is examined with a UWB antenna integrated with RF amplifiers covering 1.8-5.5 GHz and occupying a small portion of the user mobile terminals.

5. Port isolation enhancement of a UWB MIMO antenna is reported through the integration of amplifiers. Better impedance matching characteristics of the passive antenna is also observed by the co-designed active integrated MIMO antenna which also improves antenna total radiation efficiency and realized gain.

CHAPTER 2

BACKGROUND

2.1 Basic Antenna Performance Metrics

An antenna can be considered as a transducer that converts radio signal to electrical energy or vice versa. In other words, it can be defined as a mean for radiating or receiving radio waves. Although there are different types of antennas, microstrip antennas are of high interest because of their numerous advantages such as light weight, low volume, low cost, and most importantly the compatibility with integrated circuits. Although the concept of microstrip antennas was first proposed in 1953 by Deschamps [14], it was not before the 1970s when research in this area got accelerated due to the availability of good substrates with low loss tangent and attractive thermal and mechanical properties. In recent days, fabrication, materials and technology got well developed and obtaining compact size devices utilizing microstrip antennas became a reality.

In this chapter, the basic parameters that characterize the behavior of the antennas and MIMO antenna systems are discussed. The definitions and governing equations along with physical meanings are presented. In addition, some basic RF amplifier metrics are discussed.

2.1.1 Resonance

The resonance of an antenna refers to the condition when the reactive part of its input impedance is zero. In other words, at the point of resonance, the input impedance of an antenna is real. Every antenna structure has at least one resonant frequency which is defined according to its structure and material properties [15].

2.1.2 Radiation Pattern

The radiation pattern of an antenna describes the spatial distribution of the radiated energy. These patterns are used to characterize an antenna coverage. These patterns are generally measured in the far field of the antenna. It is customary to show the gain patterns or electric field patterns as the radiation patterns of the antenna under test. For example, 3-d radiation pattern of a mobile phone antenna at two GSM bands (at 900 and 1800 MHz) are shown in Fig. 2.1 [16].

2.1.3 Directivity

The directivity of an antenna indicates how much of the radiated energy is directed towards a specific region surrounding the antenna with respect to an isotropic

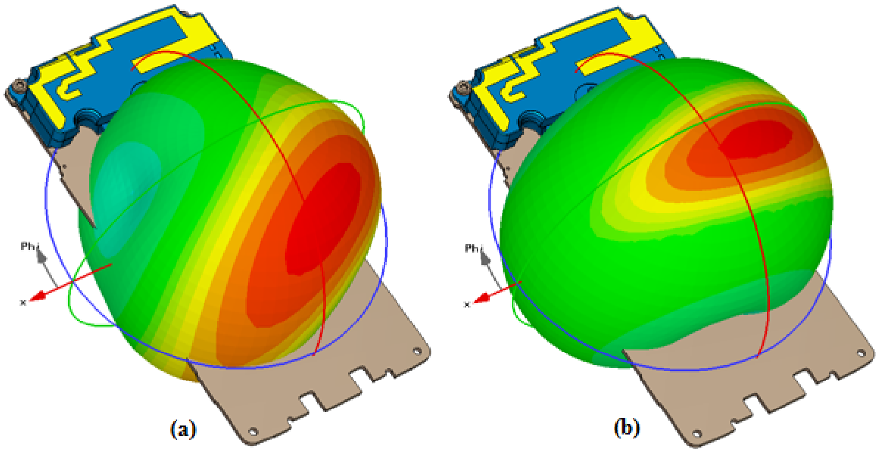

Figure 2.1: 3-d radiation pattern of a mobile antenna: (a) at 900 MHz and (b) 1800 MHz. [16]

radiator. The directivity is defined as the ratio of the radiation intensity in a given direction to the radiation intensity averaged over all directions. The average radiation intensity can be defined as the total power radiated by the antenna divided by 4 as shown in (2.1) where D is the directivity, U is the radiation intensity (Watts/unit solid angle), U_0 is the radiation intensity of isotropic source and P_{rad} is the total radiated power [17].

$$D(\theta,\phi) = \frac{U(\theta,\phi)}{U_0} = \frac{U(\theta,\phi)}{P_{rad}/4\pi} = \frac{4\pi U(\theta,\phi)}{P_{rad}} \tag{2.1}$$

2.1.4 Efficiency

The efficiency of an antenna is a percentage that shows the ratio between the amount of radiated power to the amount of power supplied to the antenna. It includes the loss due to the impedance mismatch at the input of the antenna as well as the loss in the antenna structure. The overall efficiency can be defined as in (2.2) where η_0 is the total radiation efficiency, η_r is the reflection (mismatch) efficiency, Γ is the reflection coefficient, η_c is the conduction efficiency and η_d is the dielectric efficiency.

$$\eta_0 = \eta_r \times \eta_c \times \eta_d = (1 - |\Gamma|^2) \times \eta_c \times \eta_d \tag{2.2}$$

2.1.5 Gain

The gain is another parameter of a passive antenna which defines the limit of miniaturization along with other parameters like bandwidth and efficiency. Gain of a passive antenna is of course a relative quantity which measures the power gain in a specific direction compared to an ideal lossless isotropic antenna. Gain of an antenna in a specific direction is defined as the ratio of the intensity in a given direction to the radiation intensity that would be obtained if the power accepted by the antenna were radiated isotropically [17]. Gain of an antenna can be related to the antenna efficiency and directivity as in (2.3).

$$Gain = \eta_0 \times Directivity \tag{2.3}$$

2.1.6 Bandwidth

The bandwidth of an antenna is defined as the range of frequencies within which the performance of the antenna satisfies specific standards. In practice, the bandwidth is determined by the -10dB or -6dB points of the reflection coefficient. For narrowband antennas, it is customary to express the bandwidth as a difference of upper to lower frequencies and for wideband antennas, bandwidth is expressed by the fractional bandwidth i.e. the percentage of the frequency difference (upper and lower) over the center frequency [15].

2.2 MIMO Antenna Metrics

2.2.1 Total Active Reflection Coefficient (TARC)

To properly characterize the MIMO antenna efficiency and bandwidth, the scattering parameters are not sufficient [18]. Thus, TARC is defined for better characterization of MIMO antennas (multi-port) and it is the ratio of the square root of the total reflected power to the square root of the total incident power [19]. For an N-element MIMO antenna, it is given by (2.4) where a_i and b_i are the incident and reflected signals, respectively. For a two-element MIMO antenna system, TARC can be evaluated from the scattering parameters by (2.5) where θ is the input feeding phase, S_{xx} is the reflection coefficient and Sxy is the transmission coefficient [20].

$$\Gamma_a^t = \frac{\sqrt{\sum\limits_{i=1}^{N} |b_i|}}{\sqrt{\sum\limits_{i=1}^{N} |a_i|}} \tag{2.4}$$

$$\Gamma_a^t = \frac{\sqrt{|S_{11} + S_{12}e^{j\theta}|^2 + |S_{21} + S_{22}e^{j\theta}|^2}}{\sqrt{2}} \tag{2.5}$$

2.2.2 Isolation

Isolation in MIMO antenna systems measures the power coupled between antenna elements through the substrate, ports and ground plane. The transmission coefficient S_{xy} measures this quantity. Isolation (or port isolation) does not take care of the coupling of radiators in the air or through the radiation pattern. It is customary to see isolation values of at least 10 dB among different antenna elements in a MIMO system. To enhance the isolation, different techniques such as defected ground structure (DGS), lumped components and neutralization line (NL) can be used depending on the causes of coupling [9].

2.2.3 Correlation Coefficient

The isolation of MIMO antenna accounts for the coupling in the structure (through substrate and ground plane). But for better MIMO performance, the antennas should have to show uncoupled behavior (ideally) over the air (channel). The correlation coefficient measures the coupling between the antenna elements by their radiation patterns as well as the effect of the environment. The lower the correlation coefficient, the better the wireless channel diversity performance of the MIMO antenna. The square of the correlation coefficient is known as the envelop correlation coefficient (ECC). The ECC can be calculated from the radiation patterns by (2.6) where $\vec{F_i}(\theta, \phi)$ is the three dimensional radiation field pattern of the antenna when i-th port is excited and an isotropic channel is assumed. An alternate method of calculating the correlation coefficient from s-parameters is derived in [22] as shown in (2.7). However, the derivation in [22] assumes that the radiated power is equal to input power which makes (2.7) valid for highly efficient antennas only. So, care should be taken while calculating correlation coefficient of low efficient antennas and thus it is imperative to evaluate ECC from radiation patterns irrespective to antenna efficiency.

$$\rho_e = \frac{\left| \iint_0^{4\pi} \left[\vec{F}_1(\theta,\phi) \times \vec{F}_2(\theta,\phi) \right] d\Omega \right|^2}{\iint_0^{4\pi} \left| \vec{F}_1(\theta,\phi) \right|^2 d\Omega \iint_0^{4\pi} \left| \vec{F}_1(\theta,\phi) \right|^2 d\Omega} \tag{2.6}$$

$$\rho_{eij} = \left| \frac{|S_{ii}^* S_{ij} + S_{ji}^* S_{jj}|}{\sqrt{(1 - |S_{ii}^2| - |S_{ji}^2|)(1 - |S_{jj}^2| - |S_{ij}^2|)}} \right|^2 \tag{2.7}$$

2.2.4 Diversity Gain

Diversity is usually achieved when multiple versions of a transmitted signal is received. When wireless channels are uncorrelated, the combined signal at the receiver will provide higher SNR level and thus better signal reception. Diversity gain (DG) measures the effect of diversity on the communication system. DG is defined as the difference between the SNR of the combined signals of a diversity antenna system and that of a single antenna system. DG can be evaluated from ECC as described in (2.6) [21] by the expression shown in (2.8).

$$DG = 10\sqrt{1 - \rho_e} \tag{2.8}$$

2.2.5 Mean Effective Gain

The standalone gain of a MIMO antenna system presented in Section 2.1.5 is generally measured in an anechoic chamber. Thus, it cannot reflect the effect of the environment. But it is important to see the effect of environment on MIMO antenna gain. The mean effective gain (MEG) evaluates the diversity antenna gain under environment effect like urban, rural and so forth. A mathematical expression is presented in [22] as shown in (2.9) satisfying (2.10) where XPD is the cross-polarization power ratio (the ratio between the vertical mean incident power to the horizontal mean incident power), $G_\theta(\theta, \phi)$ and $G_\phi(\theta, \phi)$ are the antenna gain components and $P_\theta(\theta, \phi)$ and $P_\phi(\theta, \phi)$ represent channel model (power distribution).

$$MEG = \int_0^{2\pi}\int_0^{\pi} \left[\frac{XPD}{1+XPD} G_\theta(\theta,\phi) P_\theta(\theta,\phi) + \frac{1}{1+XPD} G_\phi(\theta,\phi) P_\phi(\theta,\phi) \right] \tag{2.9}$$

$$\begin{gathered} \int_0^{2\pi}\int_0^{\pi} [G_\theta(\theta,\phi) + G_\phi(\theta,\phi)] sin\theta d\theta d\phi = 4\pi \\ \int_0^{2\pi}\int_0^{\pi} P_\theta(\theta,\phi) sin\theta d\theta d\phi = \int_0^{2\pi}\int_0^{\pi} P_\phi(\theta,\phi) sin\theta d\theta d\phi = 1 \\ XPD = \frac{P_V}{P_H} \end{gathered} \tag{2.10}$$

A number of channel models are available in the literature. A general model of channel reported in [22] and expressed in (2.11) can be used to evaluate MEG from (2.9). This channel model assumes a uniform distribution for the signals in the azimuth direction and a Gaussian distribution in the elevation direction considering a regular Rayleigh fading channel.

$$\begin{aligned} P_\theta(\theta,\phi) &= A_\theta\ exp\left[-\frac{[\theta-(\frac{\pi}{2}-m_V)]^2}{2\sigma_V^2}\right], (0\leq\theta\leq\pi) \\ P_\phi(\theta,\phi) &= A_\phi\ exp\left[-\frac{[\theta-(\frac{\pi}{2}-m_H)]^2}{2\sigma_H^2}\right], (0\leq\theta\leq\pi) \end{aligned} \tag{2.11}$$

2.3 RF Amplifiers Design Considerations

Amplifiers at microwave frequency range differ significantly from the conventional low frequency circuit approach and consequently special considerations are necessary. First of all, voltage and current applied should be considered as waves which necessitates appropriate matching at both the input and output of the amplifiers to reduce the voltage standing wave ratio (VSWR) and avoid undesirable oscillations. For this reason, stability analysis is the first step for RF amplifier design. Also, gain, efficiency, linearity and noise figure are the key requirements of RF amplifiers. As a driving stage in a transmitter, RF amplifiers are intended to have good flat gain over the bandwidth of operation with good power efficiency. On the other hand, in the receiving chain, low noise RF amplifiers are intended to design for low noise figure with maximum possible gain which decides the ultimate system noise figure as they are the first stage in a receiver. A generic RF amplifier system block diagram is shown in Fig. 2.2 [23] where the amplifier is described by the scattering parameters at a certain bias condition. To check the amplifier for unconditional stability, the Rollett factor k needs to be greater than 1 and $|\Delta|$ to be less than 1 which are defined as in (2.12).

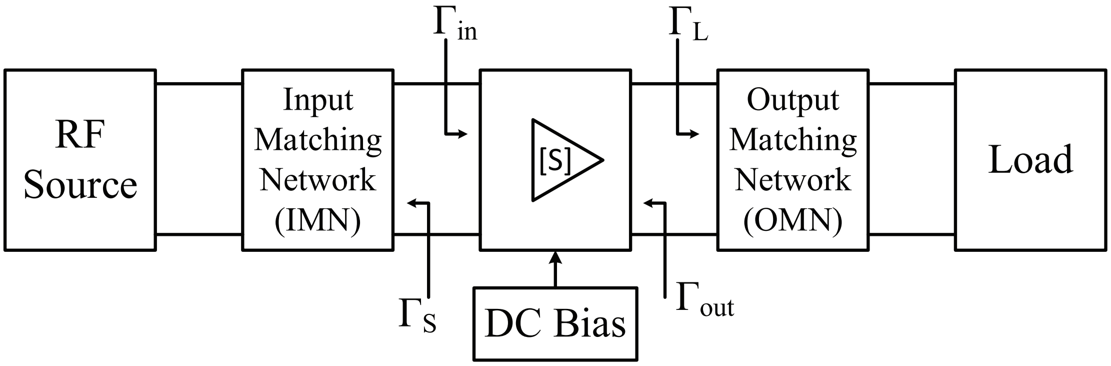

Figure 2.2: Generic RF amplifier system. [23]

$$\begin{aligned} |\Delta| &= |S_{11}S_{22} - S_{21}S_{12}| < 1 \\ k &= \frac{1 - |S_{11}|^2 - |S_{22}|^2 + |\Delta|^2}{2|S_{21}||S_{12}|} > 1 \end{aligned} \tag{2.12}$$

If the output to input feedback of the amplifier $S_{12} = 0$, the Rollett factor k approaches infinity which indicates the amplifier is unconditionally stable. However, if the amplifier is potentially unstable, stabilization methods needs to be used. This is done by introducing some losses either at the input or output ports so that the oscillation gets diminished. This can be done by adding series resistance or shunt conductance as shown in Fig. 2.3 and Fig. 2.4, respectively [24],[25]. Adding such resistance/conductance in the input or output port has the advantage of wideband stabilization but this procedure suffers from power loss and extra thermal noise introduced by the lossy component. From this perspective, it will be prudent to use the lossy component at the output port instead of input since there is a chance of noise amplification which will worsen the noise performance of the amplifier.

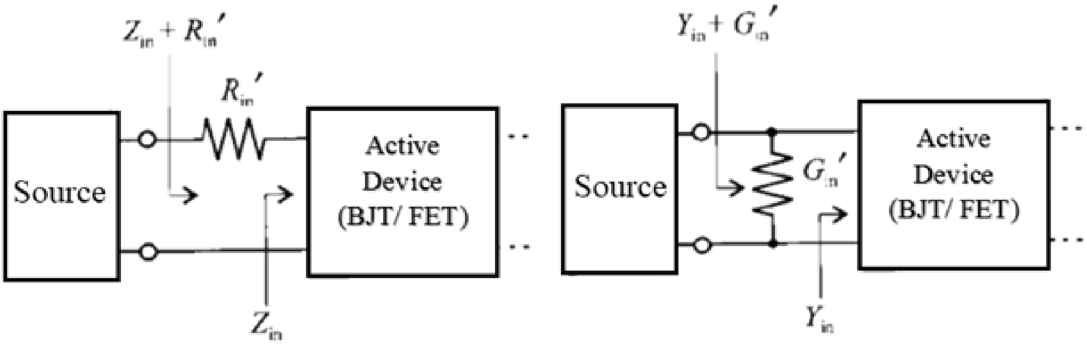

Figure 2.3: Stabilization adding lossy component in the input port. [24],[25]

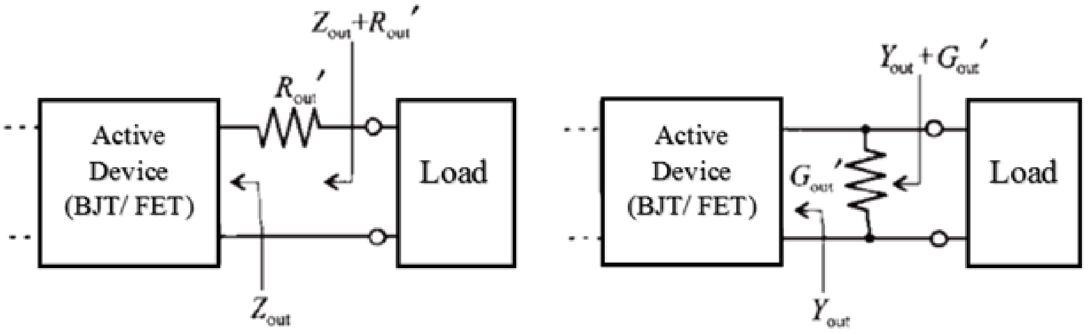

Figure 2.4: Stabilization adding lossy component in the output port. [24],[25]

One simple possible solution in this perspective can be the source degenerative inductance configuration which emulates an input resistance of $R_{in} = L_{degen}\frac{g_m}{C_{gs}}$ as shown in Fig. 2.5 [24],[25] where g_m is the transconductance of the transistor under certain bias condition and C_{gs} is the gate-to-source capacitance.

After stabilizing the raw device, the amplifier system is designed for specific requirements of gain, linearity, noise figure, bandwidth and VSWR. Obviously,

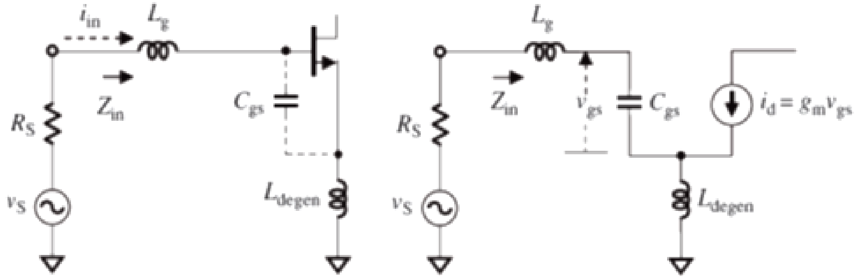

Figure 2.5: Source degenerative inductance for transistor stabilization. [24],[25]

there is no topology that can provide the best results of all these parameters. In fact, they are highly correlated and intense optimization is required. For example, if the gain of an amplifier is set to the highest value, dynamic range, noise figure and bandwidth are going to suffer. In general, depending on the situation and specific requirements, gain circles, noise circles and VSWR circles are plotted on a Smith chart and optimized values are chosen for which the amplifier system is designed. In general, the RF driving amplifiers are optimally designed for better gain, efficiency, linearity at the desired frequency band while the LNAs are designed for optimized gain and noise figure.

Several power gain relations are used in the design of microwave amplifiers. The transducer power gain G_T, operating power gain G_P and the available power gain G_A are defined in (2.13). Amplifier design based on operating gain and available power gain are accomplished considering conjugate matching at the source and load planes, respectively. Thus, mismatch and gain trade-off is considered in the load and source plane, respectively, for G_P and G_A and design process starts by selecting Γ_L and Γ_S, respectively. In general, determination of Γ_L and Γ_S are performed by trading-off gain, noise figure and VSWR which can be achieved by constant gain, noise and VSWR circles. Detailed procedures for the expressions of gain, noise and VSWR circles can be found in [23], [26].

$$
\begin{aligned}
G_T &= \frac{1-|\Gamma_S|^2}{|1-\Gamma_{in}\Gamma_S|^2}|S_{21}|^2\frac{1-|\Gamma_L|^2}{|1-S_{22}\Gamma_L|^2} \\
G_T &= \frac{1-|\Gamma_S|^2}{|1-S_{11}\Gamma_S|^2}|S_{21}|^2\frac{1-|\Gamma_L|^2}{|1-\Gamma_{out}\Gamma_L|^2} \\
G_P &= \frac{1}{1-|\Gamma_{in}|^2}|S_{21}|^2\frac{1-|\Gamma_L|^2}{|1-S_{22}\Gamma_L|^2} \\
G_A &= \frac{1-|\Gamma_S|^2}{|1-S_{11}\Gamma_S|^2}|S_{21}|^2\frac{1}{1-|\Gamma_{out}|^2}
\end{aligned}
\tag{2.13}
$$

2.4 Summary

In this chapter, different parameters of antenna and MIMO antenna system are discussed such as gain, directivity, efficiency, TARC, ECC, MEG, and DG. These parameters are generally used to characterize and evaluate a MIMO antenna system. In addition, design consideration of an RF amplifier are discussed briefly.

CHAPTER 3

LITERATURE REVIEW

There are different types of AIAs that appeared in the literature and can be categorized as:

1. Oscillator type AIA
2. Amplifier type AIA
3. Mixer or frequency conversion type AIA
4. Transceiver type AIA
5. Non-fostering AIA and
6. Other AIAs- frequency and polarization agile

Oscillator type AIAs are discussed and compared in Section 3.1. In this type of antenna, active devices (either two or three terminal) can be used and biased in their unstable regions for oscillation start-up and gain is set for stable oscillation. From any oscillator type AIAs, features like low phase noise, higher DC to

RF conversion efficiency, higher antenna gain, higher effective isotropic radiated power (EIRP) and antenna miniaturization via active loading are recommended. Moreover, multiband and MIMO compatibility are also highly desired.

Amplifier type AIAs are classified in two categories as well: 1) power amplifier (PA) AIA and 2) low noise amplifier (LNA) AIA. In PA type AIA, higher power added efficiency (PAE) is desired along with multiband operation. On the other hand, low noise figure (NF) is expected from the LNA type AIA. Both of these two AIA types are discussed in Sections 3.2.1 and 3.2.2, respectively, considering their performance metrics. Mixer and transceiver type AIAs are discussed in Sections 3.3 and 3.4, respectively. Other applications based AIAs are generally for polarization or frequency agile antennas, discussed in the Section 3.6.

Overall, very few works are reported that considers antenna miniaturization through active device integration. And the AIA works that consider antenna miniaturization are oscillator type which are not suitable for two way communication. Moreover, no AIA has been reported yet considering MIMO applications which are the main motivators for this work.

3.1 Oscillator Type AIAs

In this section, different types of AIA oscillators are discussed and compared. A patch antenna based AIA oscillator appreared in [27] as early as in 1988 where an unstable field effect transistor (FET) was used for oscillation start-up and sustained operation as shown in Fig. 3.1. Active integration was achieved by placing the antenna element in the feedback loop and considering it as an immittance at the desired band of operation. In this work, a power output of 17 mW was achieved at 5.7 GHz. Single band operation was reported with a patch antenna in the feedback path of an oscillator. In this work, antenna size miniaturization using active or passive loading, multiband operation, MIMO performance and simultaneous transmit and receive function are not considered which are highly recommended for modern wireless handheld devices.

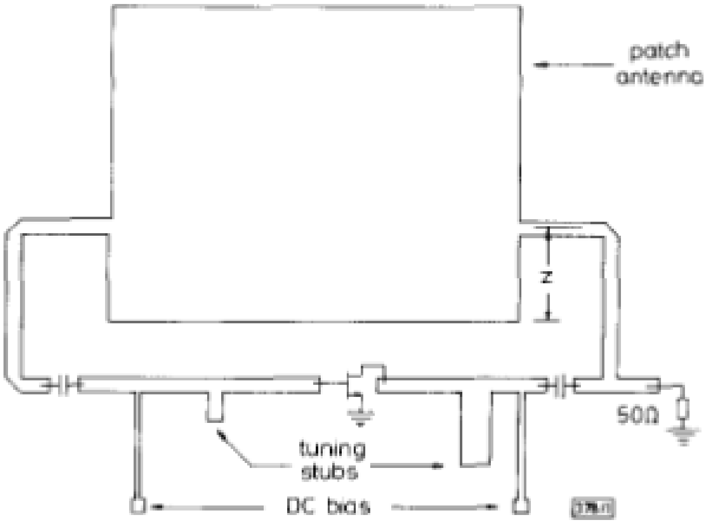

Figure 3.1: AIA patch antenna oscillator configuration. [27]

A semi-ring frequency configurable self-oscillating AIA is presented in [28]. The proposed design is shown in Fig. 3.2. The antenna system uses a PIN diode, a varactor diode and a FET for the realization of the oscillator and frequency reconfigurability. It offers two bands of operations alternatively in the range of 4.474.85 and 5.035.33 GHz by PIN diode switching. When the PIN diode is ON, the inner ring provides a shorter current path which increases the resonant frequency and operates at the higher frequency band. On the other hand, when the diode is OFF, the outer ring acts as the resonator while the inner ring acts as the stub which loads the outer ring as it behaves as a capacitor which offers miniaturization by slow wave loading. This time, the current follows a longer path which causes the resonant frequency to be lower than before. In both cases, the varactor diode provides frequency tuning of 17.7 and 16.4 MHz/V. The FET transistor is biased properly in the unstable region for oscillation to be built up and sustained. The antenna has the size of $L = 35mm$ and $W = 35mm$. However, it reports antenna gain of -0.77 and 2.28 dBi, directivity of 7.07 and 6.95 dBi and consequently, low efficiency of 16.5% and 34.1% for ON and OFF states, respectively. The DC to RF efficiency is 11.7 and 12.4% which is low. The antenna in [28] offers a truly integrated active antenna oscillator having compact size of $0.046\lambda_0^2$ where λ_0 is the free space wavelength at the lowest operating frequency.

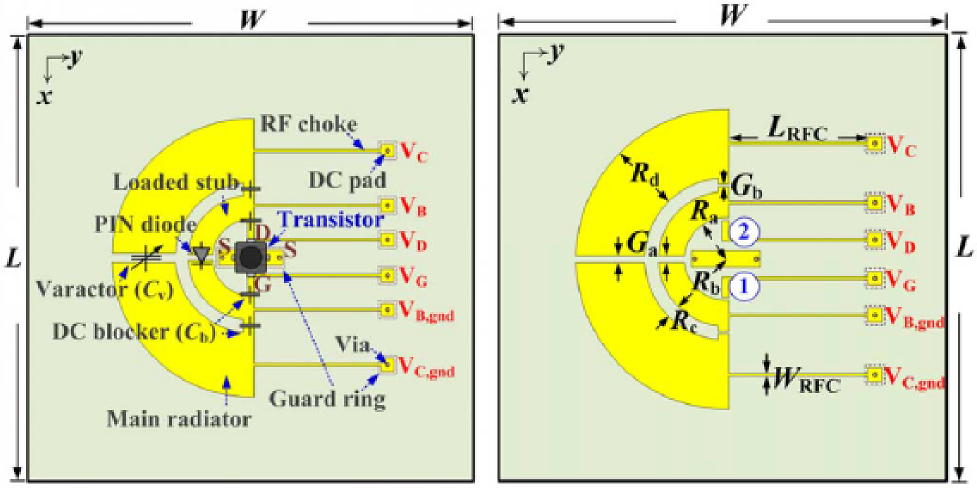

Figure 3.2: AIA patch antenna oscillator configuration. [28]

Similarly, a self-oscillating C-shaped annular antenna with integrated oscillator and voltage controlled oscillator (VCO) compatibility of 48.7 MHz/V is presented in [29] as shown in Fig. 3.3. The AIA oscillator utilizes the parasitic capacitance of the FET transistor to load the C-shaped antenna and thus reduces the resonant frequency from 6.95 to 5.65 GHz by slow wave loading. Consecutively, the size of the antenna is reduced and found to be $0.041\lambda_0^2$. The outer and inner ring dimension of the antenna is 3.9 mm and 2 mm, respectively and offered high DC to RF efficiency of 25.9%, low antenna gain of -4.6 dBi, phase noise -91.93 dBc/100 kHz, and EIRP of 7.3 dBm. The efficiency of the antenna is lower although provides good scale of miniaturization. In [30], a V-band on-chip $1 \times 1.5mm^2$ AIA oscillator is presented around a differential pair with the VCO operation in the range of 69.5-69.7 GHz targeting the application of personal area network as shown in Fig. 3.4. Higher frequency of operation makes it feasible for on-chip integration. A planer Yagi antenna is used in this work with differential voltage controlled oscillator where two varactor diodes (D1 & D2) are used to control the frequency of oscillation at the two inputs.

A self-oscillating dual ring active antenna oscillator having the size of $35 \times 35mm^2$ is presented in [31]. It reports single frequency oscillator antenna at 5.267 GHz. The DC block capacitor if replaced by a varactor diode, VCO operation is obtained. Here, no active component loading is investigated. However, it gets a better DC to RF efficiency of 31.3% compared to [29]. So, it might be a trade-off between antenna miniaturization and efficiency that also affects the

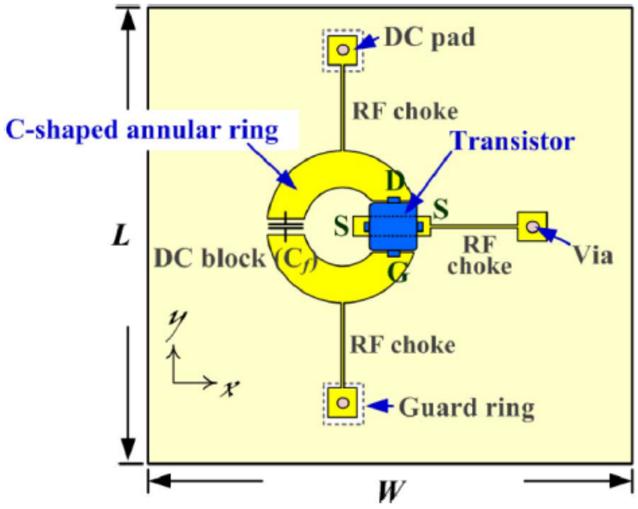

Figure 3.3: AIA patch antenna oscillator configuration. [29]

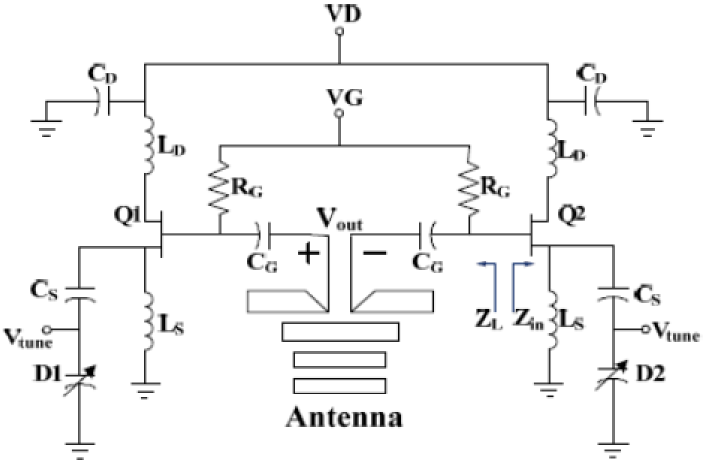

Figure 3.4: AIA patch antenna oscillator configuration. [30]

EIRP.

An aperture coupled active antenna oscillator with VCO operation where an active push-pull oscillator is designed first and the oscillation power is electromagnetically coupled to a patch radiator is presented in [32] . The patch antenna is designed to radiate at 2 GHz with the size of $51mm \times 40mm \times 0.5mm$ having the DC to RF efficiency of 32.8% and maximum EIRP of 23.5 dBm. VCO operation is also reported from 1 GHz to 4 GHz varying the DC supply voltage but EIRP gets down when the frequency of operation is decreased. Since, the push-pull oscillator cannot be affected by the absence of the antenna, this cannot be said to be an integrated active antenna oscillator.

A 36.72 mm^2 square ring active Clapp oscillator antenna at 1 GHz is presented in [33] which can be operated at high temperature. The antenna can be said to be truly integrated because the radiating element acts inseparably as a circuit element and a radiating element. An AIA oscillator that operates below 1 GHz (915 MHz) is reported in [34]. It uses a diamond shaped microstrip ring patch having size of $65mm \times 66.5mm$. Besides, VCO featured integrated oscillating antenna built around rectangular patch antennas which do not consider antenna miniaturization using active loading are presented in [35]-[37]. On the other hand, a circular patch active oscillating antenna build around a push-pull oscillator is presented in [38]. The frequency of oscillation can be controlled using the bias voltage. The antenna radiates at 2.1 GHz with a circular patch radius of 23.33 mm which is large and can be miniaturized if active component loading is considered. MIMO configuration or performance was not considered. An attractive active antenna oscillator having dual-band of operation- one at 4.7 GHz and another at 3.6 GHz is reported in [39]. It uses a dual ring microstrip patch antenna. The outer ring gives the lower resonant frequency (3.6 GHz) and the inner ring gives the higher resonant frequency (4.7 GHz) and one acts as the parasitic of the other band which increases the bandwidth at each operating frequency. The radii of the rings are reported as

5.2 mm and 8 mm, respectively. On the other hand, A multiband active antenna oscillator covering 0.8 GHz, 2.4 GHz and 3.15 GHz which is highly desirable with the dimensions of $32 \times 16.7 \times 0.6\ mm^3$ was presented in [40]. Although the antenna is co-designed with the oscillator (the antenna equivalent impedance is placed in the feedback path of a Clapp oscillator), antenna miniaturization using active loading is not considered.

To conclude, very few active oscillator antennas for multiband operation (only two [39] and [40]) are presented and no work has yet been reported regarding MIMO construction or performance of active antenna oscillators. On the other hand, antenna miniaturization using active component loading is reported by only two recent works [28] and [29] and is highly recommended. However, the main drawback of such miniaturization along oscillator functionality is that they can not be applied for two way communication systems. Possible applications are limited to the wireless power transmission for radio frequency identification (RFID) systems.

3.2 Amplifier Type AIAs

Amplifier type AIAs are generally designed for signal amplification either using a PA in the transmitting path or an LNA in the receiving path. From microwave circuit point of view, these amplifier type AIAs can be considered as two-port active devices with a passive microstrip antenna either at output or input port for the purpose of signal amplification and/or system noise performance improvement, respectively. The basic difference between the oscillator type AIA antenna and the amplifier type AIA antenna is the region of operation of the active device. The active device is operated in the unstable region for the oscillators while operated in the stable region for amplifier type AIAs. In this section, works on PA and LNA type AIAs that appeared in literature are discussed and compared.

3.2.1 PA Type AIAs

A power amplifying linearly polarized AIA operating at 2.4 GHz is shown in Fig. 3.5 [41]. The PA and the antenna in this work are designed separately (50 Ω based) and the antenna was then used as a load to the PA which yielded larger size again and cannot be said truly AIA. If the PA and antenna are designed as a single unit and the antenna is loaded by the amplifiers output or input impedances, the size could be reduced. However, the work reports 5% better power added efficiency with the integration of antenna with PA. This improvement in PAE is due to the harmonic suppression by the antenna which is inherently a load of high quality factor and generally presents either short or open to the out of band frequencies. Another PA type broadband AIA with a PAE of 60% operating in the range of 1.84 to 2.01 GHz is shown in Fig. 3.6 [42]. It occupies a large area of 8.7×11 cm^2. In this work, a circular patch with cross slot antenna is used for circular polarization.

A meshed patch antenna along with a class B amplifier shown in Fig. 3.7 that improved power added efficiency to 49% operating at 2.48 GHz is reported in [43].

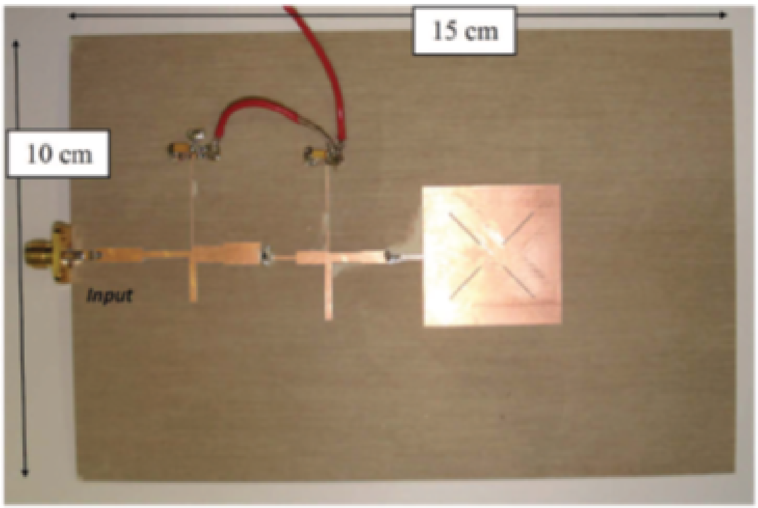

Figure 3.5: Power amplifying active antenna. [41]

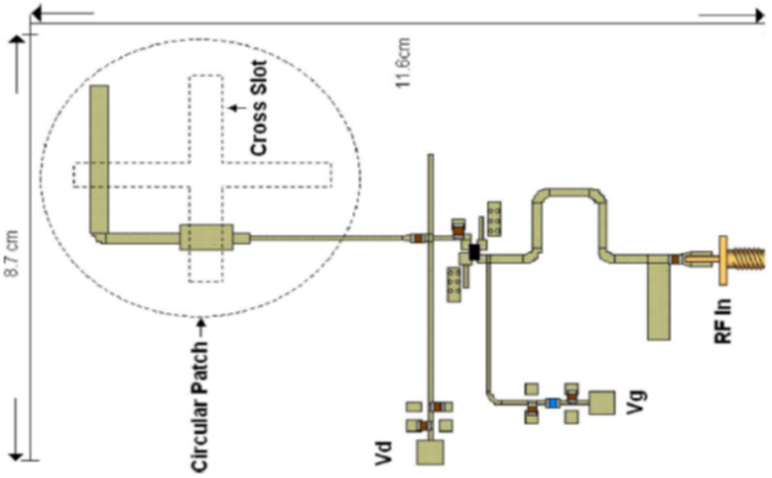

Figure 3.6: Power amplifying active antenna. [42]

But the antenna and the PA are designed separately. For impedance matching, transmission line is used and altogether occupies a large size and cannot be said a truly AIA. Improvement in size could be possible using active loading. Multiband and MIMO performance are not addressed.

In [44]-[48], different power amplifier based AIAs are presented none of which

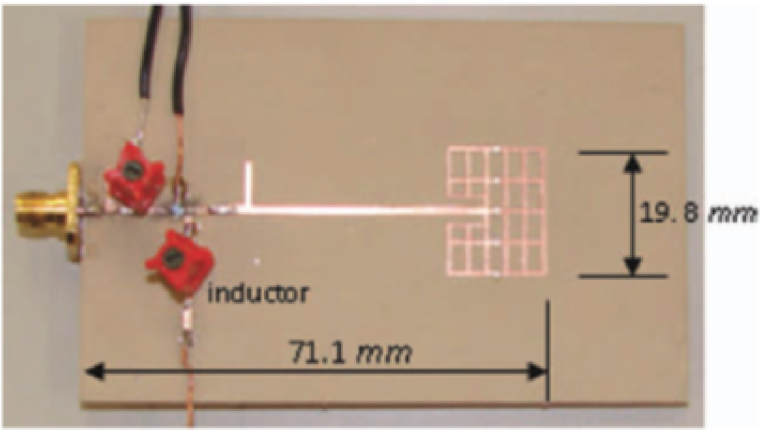

Figure 3.7: Power amplifying active antenna. [43]

can actually consider co-designing. In every case, the power amplifier and the antenna are separately designed (50 Ω based) and later the antenna is used as a load to the PA. On the other hand, an integration approach for improving PA performance by designing antenna structure is addressed in [49]. In this work, the antenna geometry is modified so that it presents optimum load to the PA to maximize PAE found from load pull analysis. Besides, the antenna also suppresses harmonics by its inherent bandstop filter characteristics. However, to achieve the maximum PAE of the PA in [49], mismatch at the input of the antenna is allowed which will deteriorate the overall radiation efficiency of the transmitting system. In this regard, comments can be made such that the design presented in this work takes care of the PA performance only. Since, the antenna is the interfacing unit to the air, mismatch loss will degrade antenna efficiency and gain as discussed in Sections 2.1.4 and 2.1.5.

To conclude, the works presented in [41]-[49] report PA type integrated antennas. None of these reports MIMO or multiband operation/configuration. Moreover, all of these works, occupy large areas. Regarding the size, the PA and antenna can be designed as a single unit and can be loaded as well so that the size can be reduced.

3.2.2 LNA Type AIAs

In the receiving path of any wireless device, obtaining a low noise figure is one of the important design objectives since it has the dominant effect on the noise performance of the overall system. Usually a trade-off between gain and noise figure goes on since high gain and low noise factor cannot be achieved simultaneously.

LNA based AIAs have appeared in literature in [50]-[61]. An AIA for receiving performance enhancement at 1.575 GHz for a GPS antenna module was presented in [50]. The achieved noise figure of the system was less than 2 dB at operating frequencies greater than 1.5 GHz. A wearable active integrated antenna for GPS and satellite phones is presented in [51]. The active part of the antenna has an LNA chip Max2659 which is directly placed with the microstrip antenna. The antenna gain of this AIA system is reported as 25.1 dBi compared to the 5.2 dBi without the LNA at 1.6 GHz. The LNA based AIA system exhibits good noise performance as well within the range 1.4 to 1.8 GHz while the antenna operates between 1.5 to 1.7 GHz range having a size of the integrated system as $100 \times 100\ mm^2$. Another LNA based AIA for FM applications is presented in [52] but with a very large reflector size of $500 \times 500\ mm^2$. [53] presents a high gain omnidirectional receiving AIA for wireless local area network (WLAN) compared to the gain of the standalone antenna 2.4 GHz. Again, the LNA and the passive antenna here are designed separately (50 Ω based) and the LNA is applied as a load to the antenna within the same substrate which is no more different than a traditional receiving path except sharing same substrate. The same comment is also valid for all other works reported by [54]-[61] as well. But as suggested before, a true AIA needs more than only sharing the same substrate requiring that the antenna and the LNA are to be designed as a single unit. If the antenna is considered for the loading the amplifier through its parasitics, the size and performance improvement could be possible.

3.3 Mixer Type AIAs

A mixer type AIA translates the input frequency either to an upper or to a lower frequency which is defined as an up or down conversion mixer, respectively. Because of its frequency conversion nature, mixer type AIAs are often called frequency conversion type AIA. The conversion efficiency is the most important performance parameter of the mixer type AIA. In general, mixer type AIAs use the non-linearity of the active components for frequency conversion. Two terminal devices such as Gunn diodes, PIN diodes and three terminal devices such as high-electrol-mobility-transistor (HEMT) or metal-semiconductor-field-effect-transistor (MESFET) are generally used. The main advantage of the three terminal devices is their conversion gain and compatibility with monolithic-microwave-integrated-circuit (MMIC) but with an extra cost of circuit complexity.

In mixer type AIAs, the active devices are biased in the non-linear region and the device non-linearity along with a filter provides the frequency conversion either up or down. Very few works are reported in this type of AIA although they have good potential in transceiver modules. A mixer type AIA is presented in [62] using a circular patch and a Gunn diode. The mixer in in this work reports conversion gain over 2 dB from 200-450 MHz. Active antenna VCO operation is also reported by varying the Gunn diode biasing voltage from 7.7 V to 10 V. Other related works found in the literature [63]-[66] are more or less similar in principle and use two terminal devices but can be improved for more conversion efficiency using three terminal devices such as BJT, FET, HEMT etc. None of these works considered antenna mniaurization through active device integration.

3.4 Transceiver Type AIAs

AIA providing simultaneous transmit and receive capability can be of great demand and interest which can implement true duplex operation. Moreover, a compact miniaturized antenna is also required for handheld MIMO system operation. Considering all these factors, duplexer-less AIA transceivers are highly recommended. But for a duplexer-less AIA transceiver, isolation between transmitting and receiving path is the main challenge to overcome. [67] presents a technique for performance improvement of non-duplexer active transceiver antenna with defected ground structure (DGS). Using DGS, the work reported -40 to -50 dB isolation between transmitting and receiving path. But the size of the antenna is large, around 80 mm×80 mm at GSM 1800 MHz as shown in Fig. 3.8. However, size can be reduced using active loading and using different antenna structures.

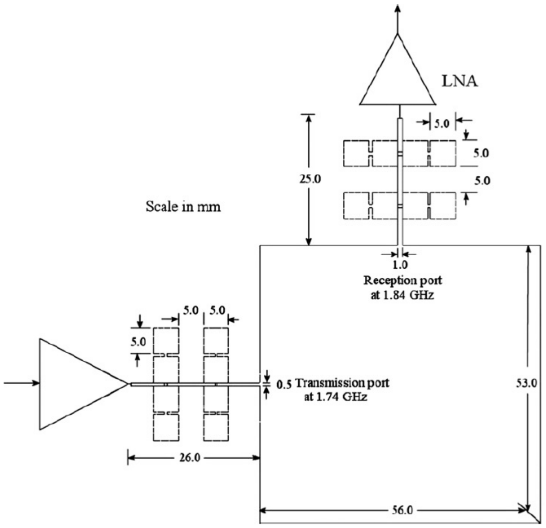

Figure 3.8: Duplexer less AIA transceiver. [67]

Another duplexer-less or isolator-less port isolation technique is presented in [68] and can be used for transmitting and receiving simultaneously as shown in Fig. 3.9. On the other hand, an AIA with simultaneous transmit and receive operations is presented in [69] where a rat race coupler is used for isolation between transmitting and receiving path as shown in Fig. 3.10. It operates at 2.4 GHz. An AIA with simultaneous transmit and receive operation at 4.05 GHz is reported in [70]. This work reports transmitting and receiving path isolation of 45 dB with an output power of 5.4 dBm and a receiving gain of 8.2 dBi. The antenna architecture is shown in Fig. 3.11. In this work, the isolation between transmitting and receiving path is provided by developing an active isolator around the antenna based on the phase cancellation technique. However, isolation without an isolator is expected which can reduce the overall size of the RF system.

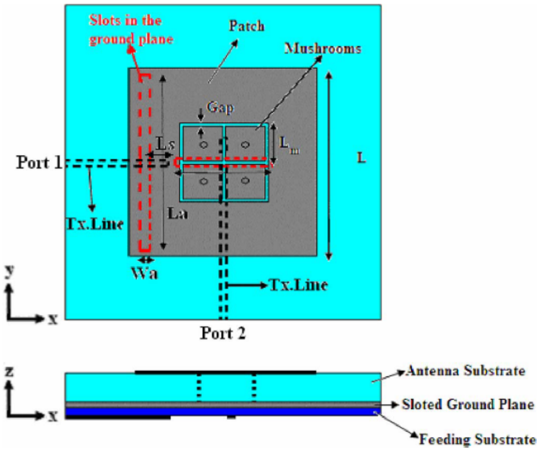

Figure 3.9: Duplexer less AIA transceiver with slotted ground structure. [68]

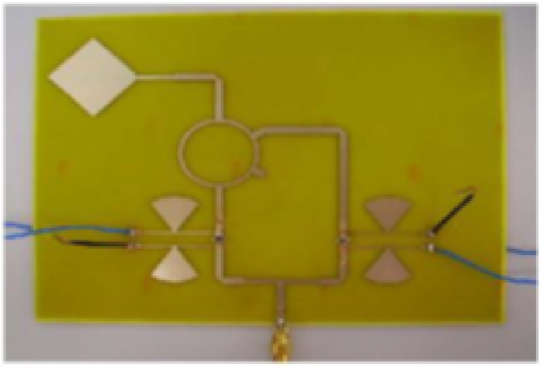

Figure 3.10: AIA transceiver with rat-race coupler. [69]

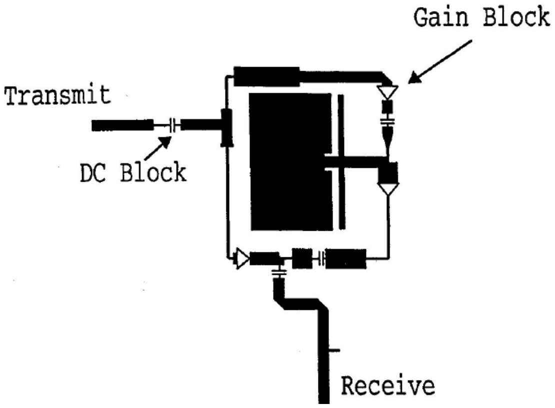

Figure 3.11: Simultaneous transmit-receive antenna with phase cancellation technique. [70]

3.5 Non-fostering AIAs

One of the fundamental limits of electrically small passive antennas in terms of impedance matching is their high quality factor which affect their bandwidth of operation. Antennas possess larger reactances as their size decreases. Thus, miniaturized antennas show narrow impedance bandwidth as their size get reduced. This fostered reactance of the miniaturized antennas cannot be compensated in a wideband fashion by traditional lossless matching networks as shown in Fig. 3.12 [71]. This is mainly because of the opposite slope of positive inductance and capacitance with respect to frequency. As can be observed from Fig. 3.12 that the impedance due to a capacitance is decreased while it is increased when frequency is increased. Thus for a highly reactive load, compensation cannot be achieved for a wider band. On the contrary, the fostered reactance can be perfectly compensated by a negative reactance and theoretically for infinite bandwidth as can be seen from Fig. 3.12 where a reactance by a capacitance is shown to be perfectly compensated by a negative capacitance. Thus, it is obvious that the bandwidth limit of small antennas can be successfully overcome by negative reactances.

Generally, a negative reactance can be realized by the negative impedance converter (NIC) as shown in Fig. 3.13. Implementation of NICs can be accomplished around MOS or Bipolar technology. First transistor based NIC was appeared in 1953 by Linvill [72] with BJTs as shown in Fig. 3.14. Applying such NICs, different non-fostering antennas are reported in [71]-[78]. A patch antenna based non-fostering antenna as shown in Fig. 3.15 is presented in [77]

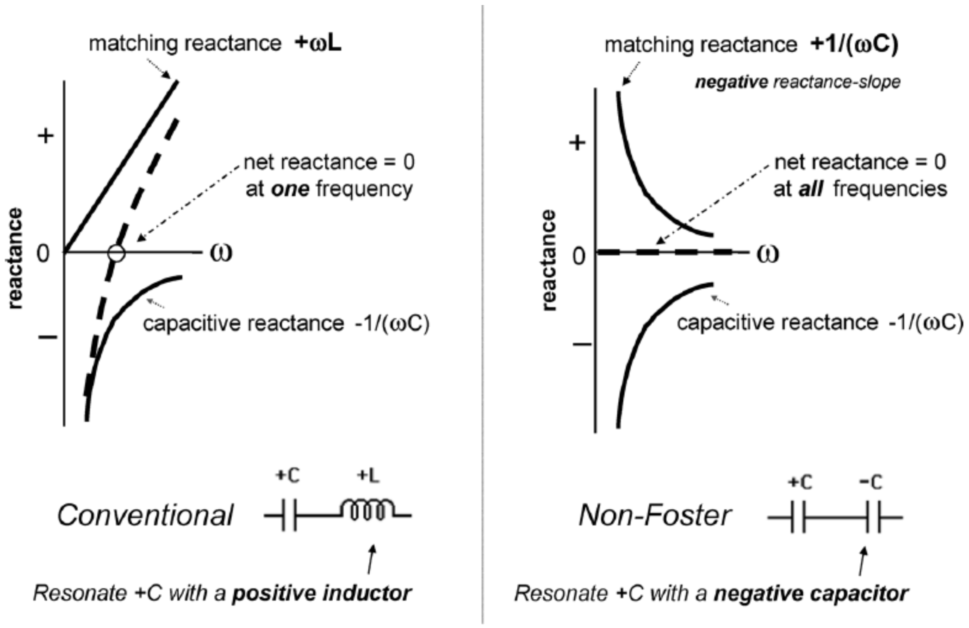

Figure 3.12: Conventional and non-fostering impedance matching. [71]

which shows a maximum 275% of bandwidth improvement (compared to their natural impedance bandwidth) operating at the center frequency of 377 MHz. On the other hand, an ultra-wideband non-fostering antenna designed with PIFA is reported in [76] operating in the range of 100-500 MHz with a capacitive NIC. Originally, the standalone antenna was showing a bandwidth of 100 MHz in the range of 550-650 MHz. Thus, use of non-fostering network shows 400% improvement in impedance matching.

To conclude, all the works presented in [71]-[78] report at least 100% of bandwidth enhancement. However, it was expected to be infinity as shown in Fig. 3.12. This limit is mainly because of the non-linearity of the active devices. It is also observed that all the works presented in [71]-[78] were examined below 500 MHz. Ultra-wideband operation by non-fostering networks at GHz range might be limited by the unstable behavior of NICs. In higher frequencies of operation, due to the higher effect of parasitic capacitance which increases positive feedback from output to input, the potential of unstable behavior increases. Thus, care should be taken while designing NICs at higher frequencies.

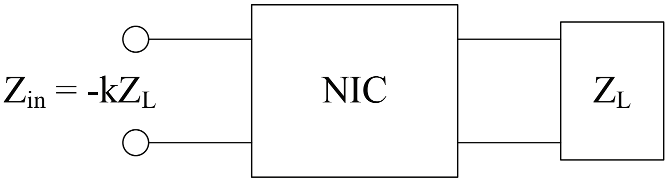

Figure 3.13: Negative impedance converter (NIC), k>0.

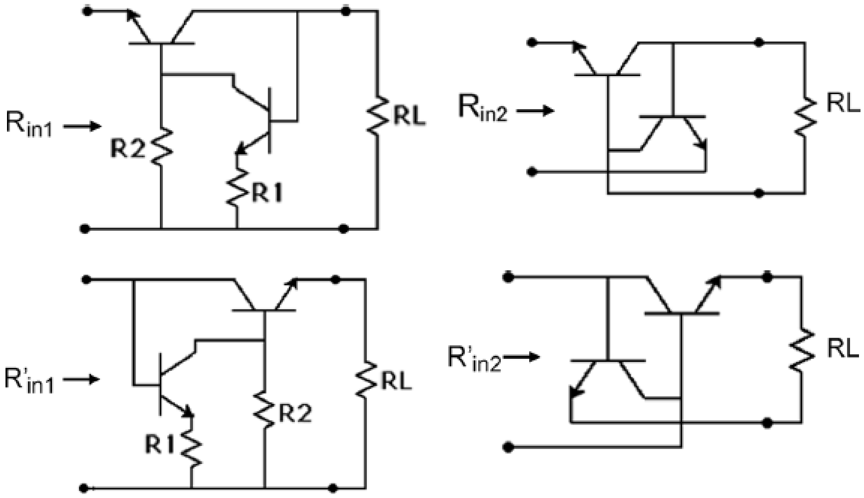

Figure 3.14: Linvill's ideal NICs. [72]

3.6 Frequency and Polarization Agile AIAs

Other antennas integrated with active devices to achieve attractive antenna features that have drawn more attention in recent years can be categorized as frequency and polarization agile antennas. Polarization and frequency agile anten-

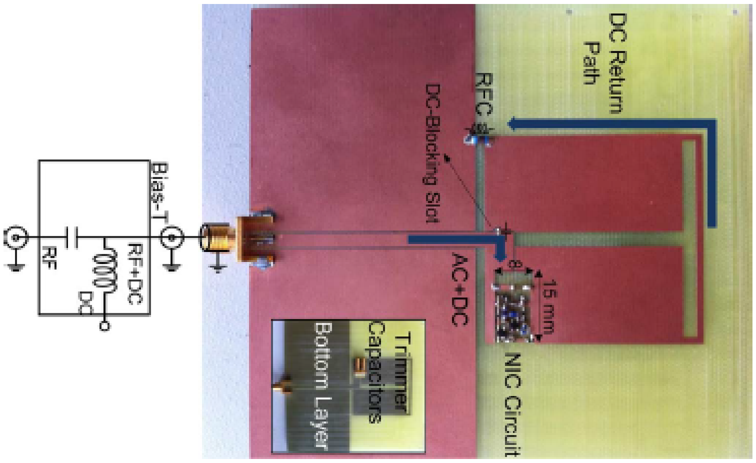

Figure 3.15: Patch antenna based non-fostering antenna. [77]

nas are types of antennas for which polarization state and operating frequency are dynamically controlled or changed. Because of the advancement in semiconductor technology, devices like PIN diode, varactor diode, BJT, FET, radio frequency micro-electromechanical systems (RF MEMS) and optical controls are widely used for the realization of frequency and polarization agile antennas. Polarization agile antennas (PAA) can have either linear (horizontal or vertical) or circular (left hand or right hand) polarization depending on the application requirements. These PAAs are very useful for many applications that provides mitigation to the multipath fading and frequency reuse for higher data throughput by means of polarization diversity. By using a single polarization agile antenna that is orthogonally polarized, a transceiver unit is possible which can have simultaneous transmit and receive functionality. The basic idea for PAAs is to change the current path in the antenna which are generally achieved by 1) adaptive reactive loading which changes the current distribution, 2) RF switches which alter the current path of the antenna, 3) RF MEMS which mechanically modify the geometry of the antenna and 4) phase shifters which provides different phase angles between two orthogonally polarized components.

On the other hand, frequency agile antennas (FAA) provide tuning over a continuous range of frequencies or can switch between a set of discrete frequencies. Because of the increase in the number of handheld devices, new applications and services, currently allocated spectrum is getting filled up rapidly which has led to the development of technologies for improving channel capacity such as MIMO systems, polarization and spatial diversity techniques, ultra-wideband and cognitive radio systems. Many of these approaches generally require multiple antennas and/or antenna with multiband or wideband functionalities. But limitation in size of the handheld compact portable devices precludes potential use of wideband or UWB antennas. Moreover, such antennas can have negative impact on the signal to noise ratio and addition filtering for suppressing unwanted noise is required. Considering all of these issues, FAAs can be a potential alternative where the operating frequency can be easily controlled. Methods for achieving FAAs can be grouped into three categories [79]: 1) mechanical actuation, 2) material actuation and 3) integrated electronic device actuation. However, in this work, realization using integrated electronic device such as diodes and transistor for both PAAs and FAAs are of interest. In this section, different FAAs and PAAs are discussed and compared considering their AIA performance.

FAA type AIAs are generally built by loading the antenna with different switches such as PIN diode, varactor diodes, FET and BJTs. In [80]-[84], FAA type AIAs using PIN diode were presented. A compact, widely tunable slotted patch FAA operating in the range of 620 to 1150 MHz is presented in [80] as shown in Fig. 3.16. The size of the radiating antenna is 24mm×20mm excluding the bias network and substrate. In this work, three PIN diodes are used to load the antenna with shorting pins which provides different radiation frequency at different combination of diode ON and OFF conditions. The reflection coefficient at different diode switching mode is shown in Fig. 3.17.

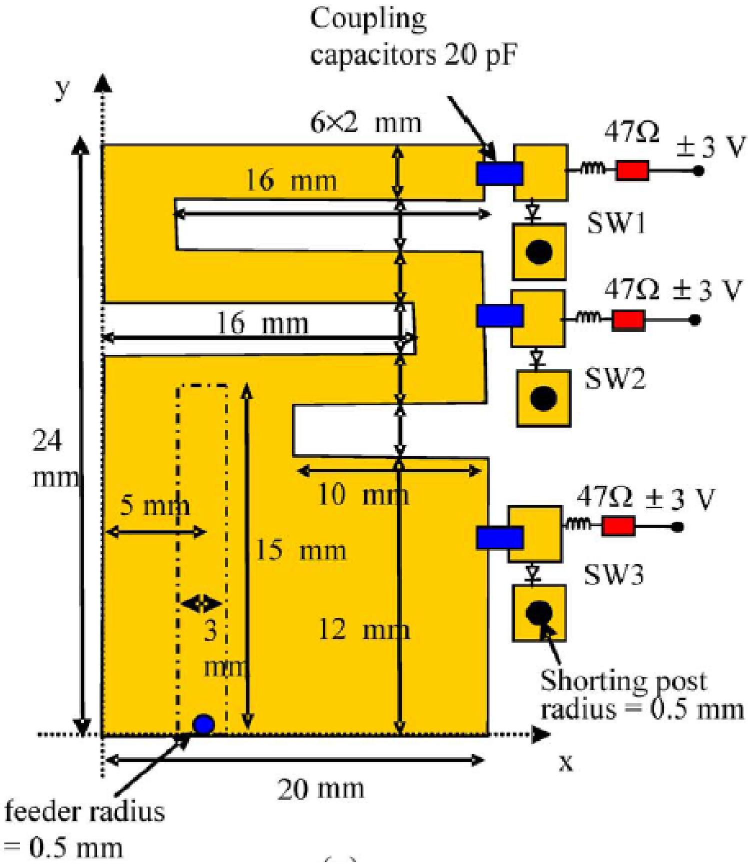

Figure 3.16: FAA type AIA using PIN diode. [80]

In [81], four PIN diodes are alternatively switched to achieve frequency agility over the range 540-890 MHz but occupies large size of 12.7cm×12.7cm. In [82], PIN diode based FAA type AIA are presented using planar inverted-F antenna (PIFA). It can switch at two discrete frequencies: 1.8 GHz and 745 MHz to cover both the GSM 800 and 1800 MHz. The size of the antenna is 100mm×50mm. A varactor diode based printed loop FAA type AIA were presented in [85] having operating range of 470-672 MHz and size of $300 \times 300 \times 4\ mm^3$. In [86], FAA type AIA for circular polarization were presented as shown in Fig. 3.18. In this work, two varactor diodes were used for frequency tuning over the range 1.3 to 1.97 GHz. The size of the antenna was reported as $50 \times 50\ mm^2$. In [87, 88, 89], a FET and optoelectronic switch based FAA type AIA are presented, respectively. Obviously, none of these works reports antenna miniaturization through active device integration.

In [90], a review of different PAAs were presented and compared. Although, many PAAs are reported but very few of them are realized by true integration of active components. Very often, PAA type antennas are realized by using a feed network for phase shifting to realize dynamic polarization. In [91]-[95], different PAA type AIAs are reported. A novel compact reconfigurable microstrip antenna with agile polarization is reported in [91] using a PIN diode in the operating range of 5.27 to 5.74 GHz as shown in Fig. 3.19. Two PIN diodes are used for the realization of different polarization as shown in Fig. 3.19. In [94], a PAA type AIA is reported where the antenna gain is enhanced using an LNA and the polarization agility is achieved using two 3 dB power splitters which alternatively provided

State	Sw1	Sw2	Sw3
(1)	on	off	off
(2)	off	on	off
(3)	on	on	off
(4)	off	on	on

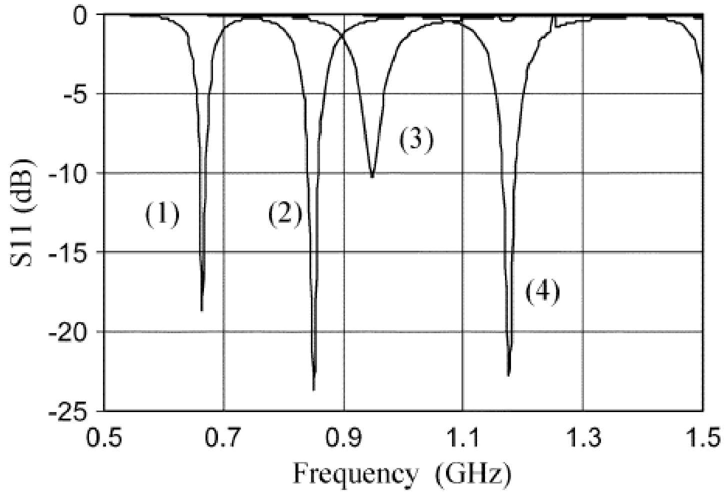

Figure 3.17: Reflection coefficient at different switching states. [80]

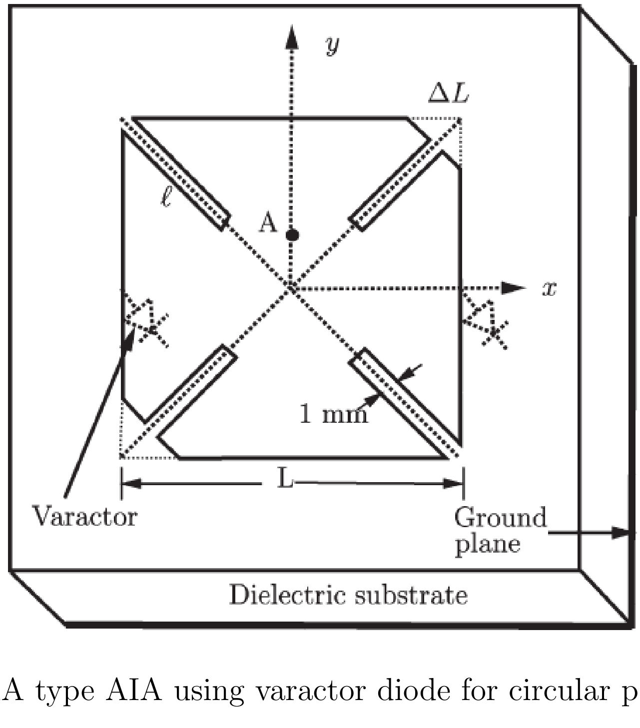

Figure 3.18: FAA type AIA using varactor diode for circular polarization. [86]

phase shifting from 0 to 90°. Because of using power splitters, the antenna occupies a large size although the radiating patch only have $15 \times 17mm^2$ at the operating frequency of 5.8 GHz.

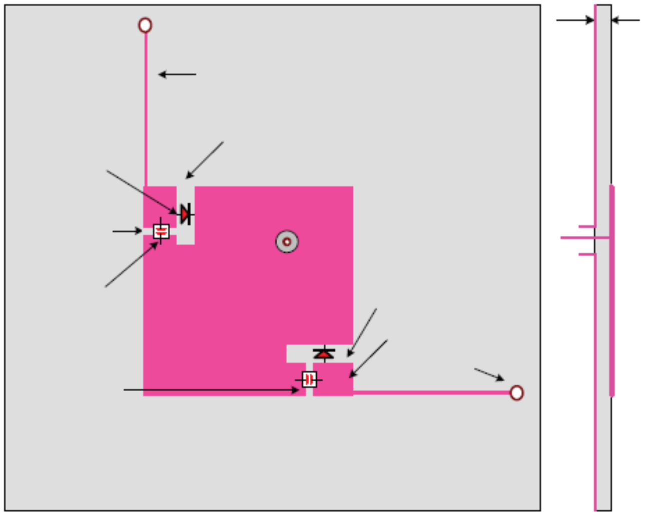

Switch 1	off	off	on
Switch 2	off	on	off
Polarization	linear	left-hand	Right-hand

Figure 3.19: PAA type AIA with PIN diode switching. [91]

To conclude, although different mechanical and electronic device actuation for both FAA and PAA type AIAs are found in literature, no work has yet been reported considering antenna miniaturization. Co-design/integration of active devices as presented in this thesis work can be effectively applied for antenna size reduction.

To summarize, a tree of AIAs categorized under different criteria is shown in Fig. 3.20. Very few works have been reported in AIAs which operate at multiple bands or ultra-wideband. Although few oscillator based active antenna miniaturization approach appeared in recent days, no work is found in literature that presents antenna miniaturization through the integration of RF amplifiers. This is of utermost importance because such miniaturization approach can be achieved by already existing amplifiers in RF front ends and thus more compact and higher degree of integration between antenna and active devices is possible. Besides, active integrated MIMO antenna has not appeared in the literature so far.

3.7 Conclusions

In this chapter, a comprehensive literature review of previous works in the area of active antennas has been presented. It has been explored that the concept of antenna miniaturization through RF amplifier integration and active MIMO antennas have not been appeared in the literature. Thus, this work introduces two novel features in antenna and RF system design paradigm: 1) antenna miniaturization via RF amplifier integration and 2) active integrated MIMO antennas. In the following chapters, these two features are discussed in details with simulation and experimental results.

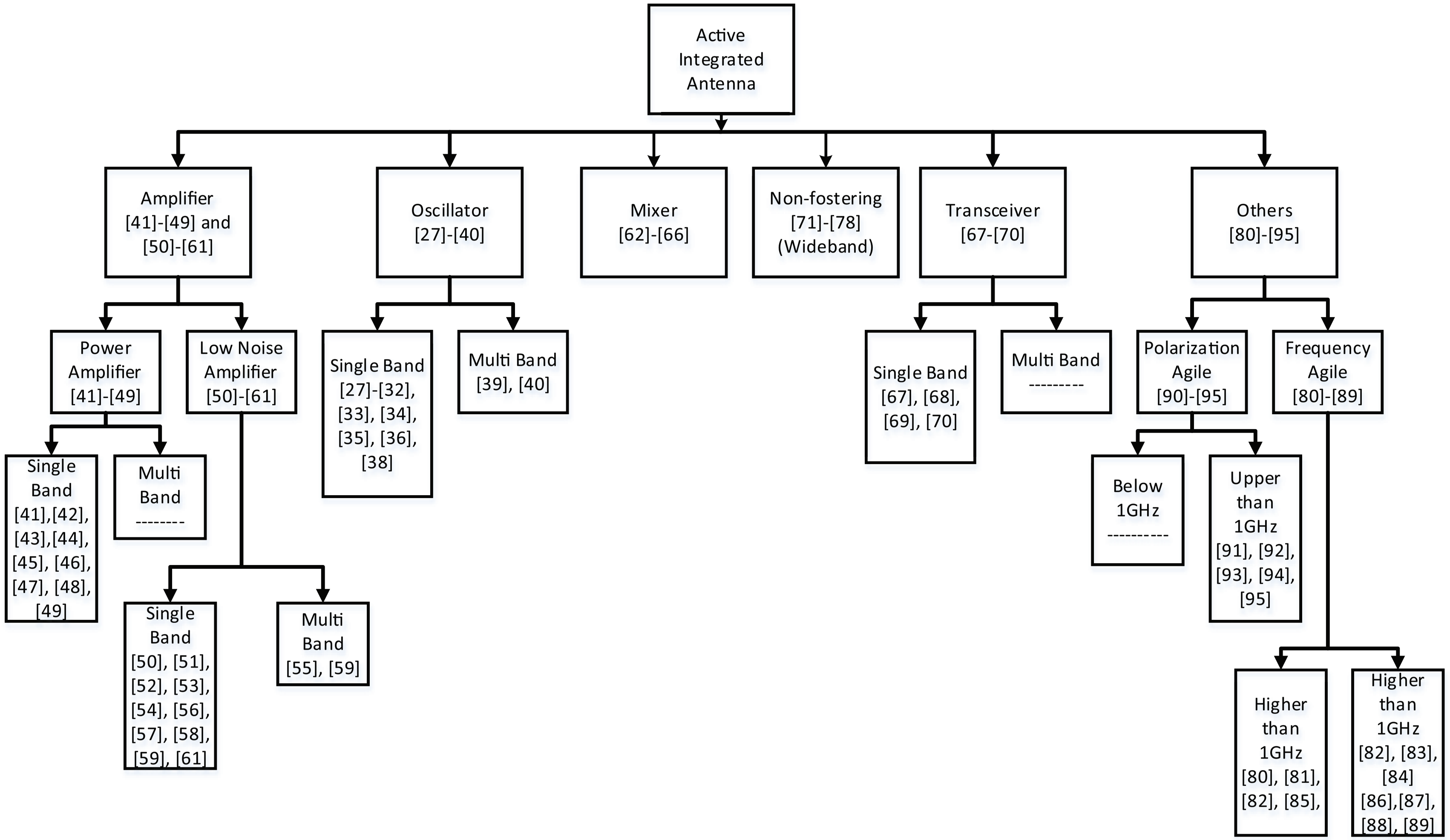

Figure 3.20: Tree of AIAs categorized under different criteria

CHAPTER 4

SIMPLIFIED REAL FREQUENCY TECHNIQUE

Bandwidth of miniaturized antennas are of significant interest for antenna designers. Thus, broadband antenna matching network (MN) design and a systematic procedure to do so is of great interest. In general, analytical approach of MN design can be deployed where closed form expressions for load and matching networks are developed and then the values of the elements in the MN are calculated, for example, L or PI or T network design. However, such analytical MN design approach cannot be carried out for complex networks. And more importantly, for antennas considered as complex frequency dependent loads, closed form expressions are not applicable most of the times. Thus, one possible brute force method can be followed by selecting an arbitrary MN and then to tune its elements for optimized matching performance. But such approach may not guarantee the best matching performance. Moreover, in this approach, one needs to select an initial

MN topology first and there is no systematic procedure for selecting such MN topology. Thus, a technique for broadband MN design is of interest which can overcome the shortcomings discussed above. In this chapter, the simplified real frequency technique (SRFT) is discussed which can be applied for broadband antenna MN design which was introduced by *B. S. Yarman*. The main advantages of SRFT are claimed to be [96]-[100]:

1. Compared to the analytical theory of broadband matching, SRFT does not require a model for the load network (antenna). Thus, this technique is more suitable for broadband antenna matching network design for today's complex antenna structures.
2. In SRFT, it is not required to select a matching circuit topology at the beginning. The best topology is derived by the technique itself based on the required matching requirement.
3. Final results are not sensitive to the initial assumptions which is of significant interest in any computer aided design technique.

4.1 Wideband MN Design

4.1.1 Description of Lossless Two-Port Network in S-parameters

Linear two port networks can be described by scattering parameters (S-parameters). A two port network with 50 Ω source and load termination is shown in Fig. 4.1. Power avalable at port1 and 2 can be described as $P_1 = |a_1|^2 - |b_1|^2$ and $P_2 = |a_2|^2 - |b_2|^2$, respectively. Thus, the total power delivered to the network will be zero since the network is lossless and can be expressed as in (4.1). By solving (4.1), the S-parameter relations are found as shown in (4.2) where p is the Laplace variable.

$$P_T = P_1 + P_2 = \begin{bmatrix} a_1^* & a_2^* \end{bmatrix} \begin{bmatrix} a_1 \\ a_2 \end{bmatrix} - \begin{bmatrix} b_1^* & b_2^* \end{bmatrix} \begin{bmatrix} b_1 \\ b_2 \end{bmatrix} = 0 \tag{4.1}$$

$$\begin{aligned} S_{11}(p)S_{11}(-p) &= 1 - S_{12}(p)S_{12}(-p) \\ S_{22}(p)S_{22}(-p) &= 1 - S_{21}(p)S_{21}(-p) \\ S_{22}(p) &= -\frac{S_{21}(p)}{S_{12}(-p)} S_{11}(-p) \end{aligned} \tag{4.2}$$

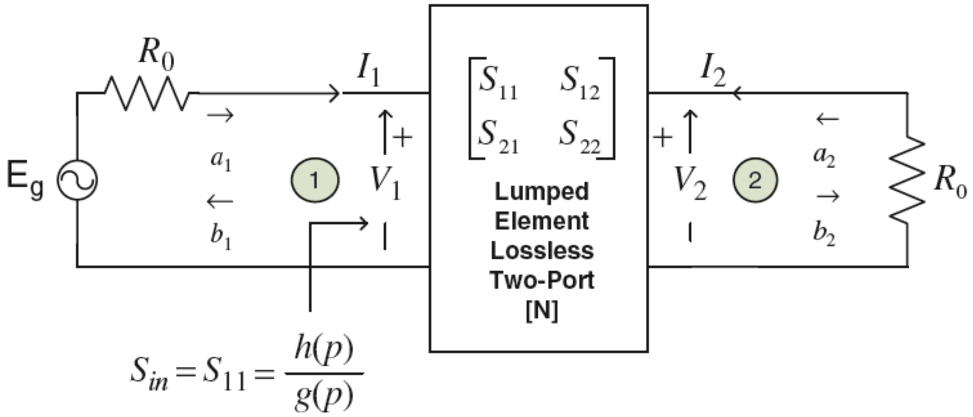

Figure 4.1: S-parameters for two port MN network.

For 50 Ω termination, $S_{in} = S_{11}$ and $S_{out} = S_{22}$. Now, if $S_{11} = \frac{h(p)}{g(p)}$ ($h(p)$ and $g(p)$ are two polynomials of Laplace variable p, then other S-parameters can be expressed in terms of $h(p)$ and $g(p)$ as expressed in (4.3) where $f_{12}(p)$ is obtained on the selected roots of $F(p^2) = G(p^2) - H(p^2) = f_{12}(p)f_{12}(-p)$, apparently which will not be a unique solution. However, by this relations, it is obvious that S-parameters can be derived from the definition of a lossless two port network from the definition $S_{11} = \frac{h(p)}{g(p)}$. It means by defining S_{11}, a lossless two port network can be described (it should be noted that the description is not unique). Actually, from this concept, SRFT is evolved. In this technique, the definition of a two port network by S_{11} is fit and optimized so that its transmission coefficient S_{21} meets the matching requirement. Afterwards, the network is retrieved from the optimized $S_{11} = \frac{h(p)}{g(p)}$.

$$\begin{aligned} S_{12}(p)S_{12}(-p) = 1 - S_{11}(p)S_{11}(-p) = 1 - \frac{h(p)h(-p)}{g(p)g(-p)} \\ = \frac{g(p)g(-p) - h(p)h(-p)}{g(p)g(-p)} = \frac{F(p^2)}{G(p^2)} \\ S_{22}(p) = -\frac{f_{12}(p)}{f_{12}(-p)}\frac{h(-p)}{g(p)} \\ where\ G(p^2) = g(p)g(-p)\ and\ F(p^2) = G(p^2) - H(p^2) \end{aligned} \tag{4.3}$$

4.1.2 Simplified Real Frequency Technique (SRFT)

As described in [96]-[100], two types of matching problems can exist: 1) single matching and 2) double matching. Single matching refers to the situation when the lossless MN is terminated with a complex load in source or load sides. Another side of the MN is terminated with a resistive load. On the contrary, MN is terminated with two complex loads in double matching problem. An example of a single matching problem is shown in Fig. 4.2 where an antenna is considered as a complex load. The basis of SRFT is to define the equalizer network in terms of its unit normalized reflection coefficient $E_{22} = h(p)/g(p)$ so that optimized transducer power gain can be achieved. Later on, the matching network (equlaizer) components are derived from the systematic procedure.

The transducer power gain $T(\omega)$ can be defined by (4.4). By replacing the S-parameters of the equalizer network defined by (4.3), the final expression of the transducer power gain (TPG) is given by (4.5). Observing (4.5), it is clear that (4.5) can be determined if L_{11}, $f(p)$ and $h(p)$ are known. For an antenna structure, L_{11} is generally known directly by its port parameters. Thus, TPG solely depends on $f(p)$ and $h(p)$ where $f(p)$ defines the transmission zeros and $h(p)$ are to be found based on the optimized TPG. For example, for a low pass LC ladder matching network, $f(p) = 1$ and for bandpass LC ladder network of k components, $f(p) = 1$. Once, $f(p)$ is selected and h(p) is arbitrarily selected then $T(\omega)$ can be determined.

$$T(\omega) = \frac{|E_{21}|^2 |L_{21}|^2}{|1 - E_{22} L_{11}|^2} \tag{4.4}$$

$$T(\omega) = \frac{|f(p^2)|^2 (1 - |L_{11}|^2)}{|h(p^2)|^2 (1 + |L_{11}|^2) + |f(p^2)|^2 - 2\ Re[L_{11} |h(p^2)|^2]} \tag{4.5}$$

At this stage, it is required to tune $h(p)$ for a target TPG which in other

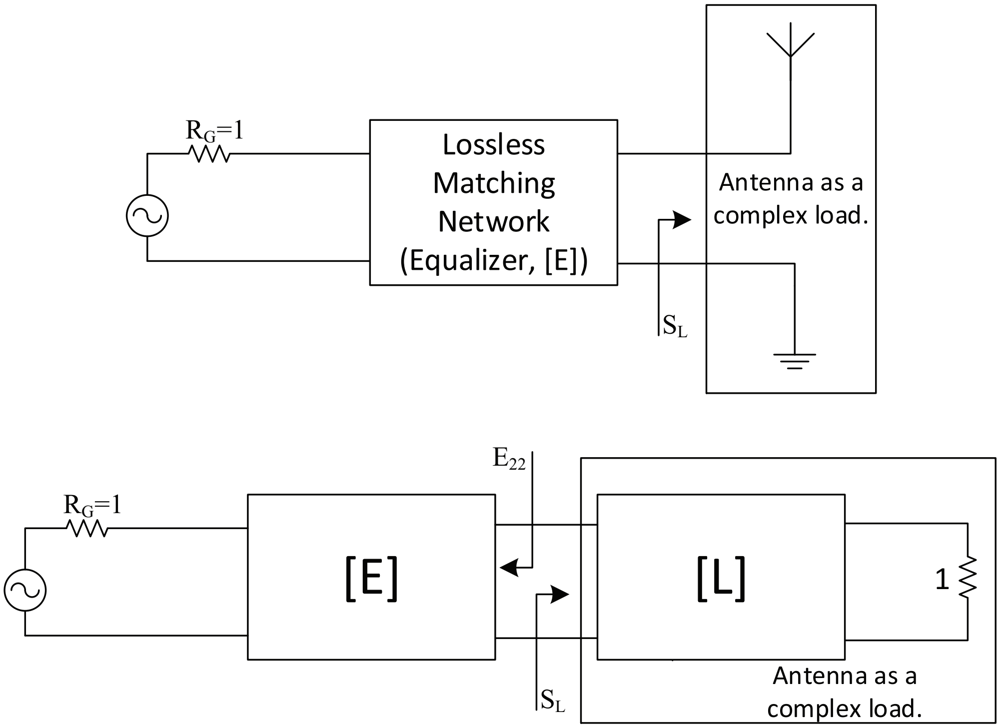

Figure 4.2: Antenna matching problem via SRFT.

words defines the antenna matching. A direct relation between TPG and input reflection co-efficent can be defined by (4.6). After finding $h(p)$ for a target TPG for a desired band of operation, the number of LC components can be decided. For, example, if a four element LC ladder MN is selected, $h(p)$ will be a polynomial of order 4 and can be initiated as $h(p) = p^4 + p^3 + p^2 + p + 1$ or in a vector form $h(p) = [11111]$. The non-linear curve fitting optimization technique will set the coefficient so that the targeted TPG is met.

$$|S_{11}| = 20\log_{10}\sqrt{1 - TPG} \tag{4.6}$$

Now, if satisfactory gain and bandwidth are achieved by $h(p)$, we can proceed to determine $g(p)$ to find $E_{22} = \frac{h(p)}{g(p)}$. However, if the determined $h(p)$ does not satisfy the required TPG and bandwidth, the number of LC elements can be increased and the optimization routine can be run again. This way, the optimum $h(p)$ is selected. After finalizing $h(p)$, $g(p)$ is to be determined by (4.7) by factorization (it should be noted that the result will not be unique). However, $g(p)$ should have all of its poles in the left half plane so that $E_{22} = \frac{h(p)}{g(p)}$ does not cause any oscillation. After determining $g(p)$, we can define the matching network in terms of $h(p)$ and $g(p)$ from the definition of E_{22} by long division. The procedure is tested with two examples and verified with the simulation results in Advanced Design System (ADS) software tool.

$$g(p)g(-p) = h(p)h(-p) + f(p)f(-p) \tag{4.7}$$

Example: Single Matching Problem

The SRFT is examined for an RLC complex load as shown in Fig. 4.3 for a single matching problem. In SRFT, the element values are normalized with respect to 50 Ω and highest operating frequency. This normalization makes the calculation easy and compact. In this example, an ultra-wideband matching network is intended to design using SRFT from DC-10GHz. Thus, the RLCs in the load network are normalized with 50 Ω and 10 GHz. The normalized values are found to be $R1 = 1; C1 = 4; L1 = 0.61$. Thus, the load can be formed as $Z_L = 0.61p + \frac{1}{1+4p}$. And load reflection coefficient can be found from $S_L = \frac{Z_L - 1}{Z_L + 1}$. The SRFT technique is begun by defining $f(p) = 1$ for low pass MN (since the matching network is supposed to work as a low pass filter). For TPG greater than 0.8 (which is equivalent to about -7dB load reflection coefficient), $h(p)$ is determined from non-linear curve fitting technique in Matlab according to (4.5). For a 4 element matching network design, $h(p)$ is initialized as [1 1 1 1 1] and found to be [-1.6822 -2.8029 -3.2100 -1.9552 -0.5564] by the optimization routine developed in Matlab. Then applying polynomial factorization, $g(p)$ is found according to (4.7) which is [1.6822 3.4638 4.4410 3.2272 1.1444]. For this $g(p)$ and $h(p)$, the TPG and matching is found as shown in Fig. 4.4 and 4.5. It can be seen that input reflection coefficient perfectly meets the -6dB matching requirement over the range DC-10GHz (normalized to 0-1) which was the design target.

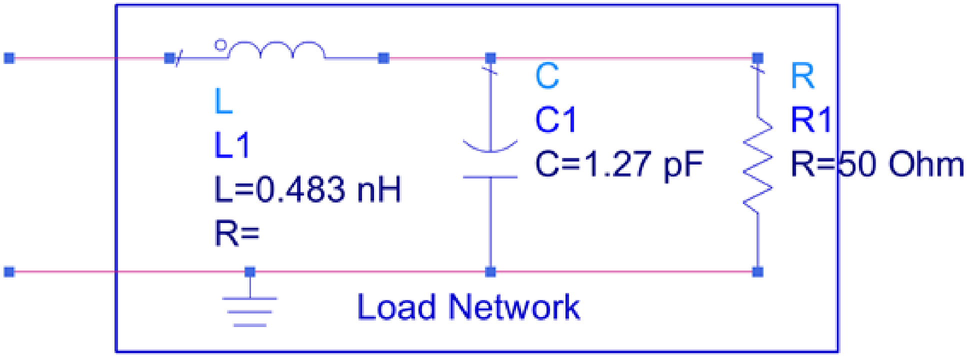

Figure 4.3: Antenna matching problem via SRFT: load network.

Now, to check the performance of the designed matching network, the circuit is simulated in ADS. To do so, first of all, the circuit components are to be estimated from $E_{22} = \frac{h(p)}{g(p)}$. This is accomplished in Matlab by polynomial division technique on $Z_M = \frac{1+E_{22}}{1-E_{22}} = \frac{g(p)+h(p)}{g(p)-h(p)}$ (implemented using 'conv' and 'deconv' functions). The finalized circuit with MN and load network is shown in Fig. 4.6. The elements of

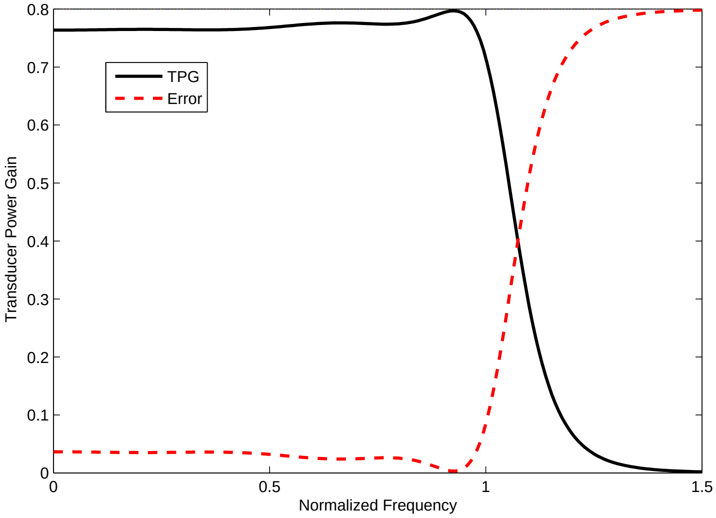

Figure 4.4: Estimated TPG by the matching network.

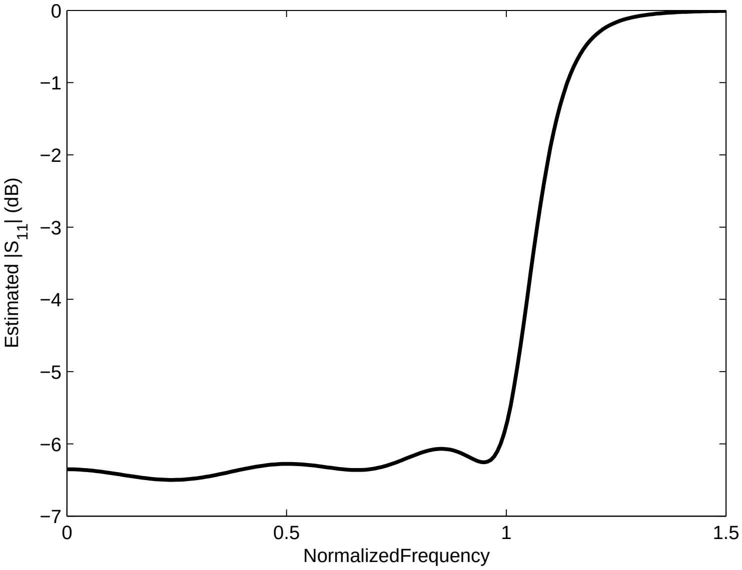

Figure 4.5: Estimated matching via SRFT.

the MN are found to be C2=1.6 pF, C3=1.185 pF, L2= 0.447 nH and L3=0.15 nH. The simulated reflection coefficient is shown in Fig. 4.7. It can be seen that the simulated reflection coefficient meets the design specification (-6 dB matching) in the region of DC-10 GHz. It should be noted that the input port is taken as 17 Ω which is found from the SRFT itself. However, a transformer can be used so that

50 Ω input can be applied. And it should not affect the matching performance.

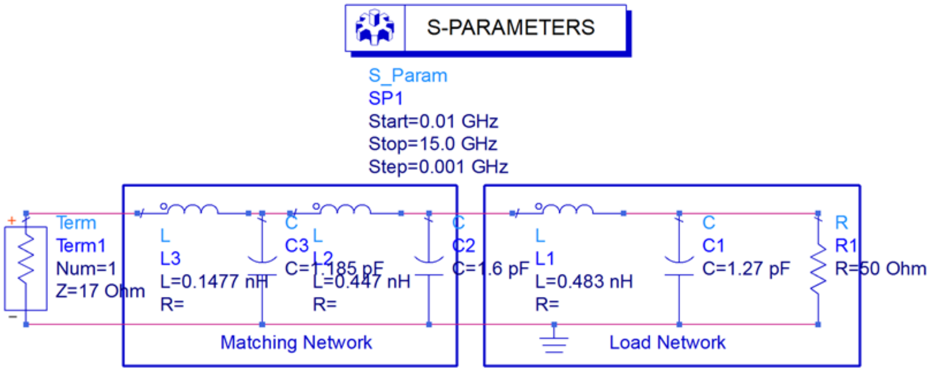

Figure 4.6: Finalized circuit simulated in ADS.

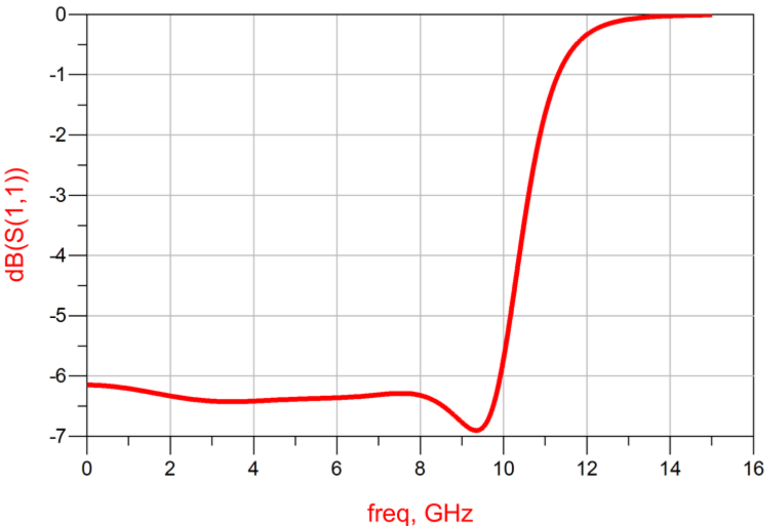

Figure 4.7: Reflection coefficient of the designed MN using SRFT.

In previous example, single matching problem is examined in details. However, double matching problem arises in integrated designs. A double matching problem is shown in Fig. 4.8. The SRFT technique steps remain the same as for the single matching problem except the expressions E_{22} and E_{11} which will be replaced by Γ_{out} and Γ_{in}, respectively. Γ_{out} and Γ_{in} can be determined from the S-parameters

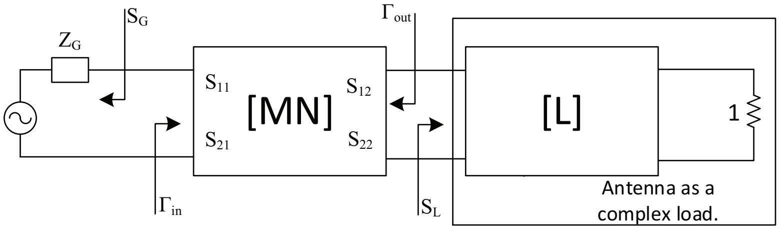

Figure 4.8: Double matching problem.

of the equalizer (MN) by the expressions (4.8) and (4.9). The TPG for double matching problem can be defined by (4.10) both from source and load sides. Still the procedure is started by defining $E22 = \frac{h(p)}{g(p)}$ and following the optimization procedure described for single matching problems.

$$\Gamma_{out} = S_{22} + \frac{S_{12}S_{21}}{1 - S_{11}S_G} S_G \tag{4.8}$$

$$\Gamma_{in} = S_{11} + \frac{S_{12}S_{21}}{1 - S_{22}S_L} S_L \tag{4.9}$$

$$\begin{gathered} T_\omega = \frac{(1 - |\Gamma_{out}|^2)(1 - |S_L|^2)}{|1 - \Gamma_{out}S_L|^2} \\ T_\omega = \frac{(1 - |\Gamma_{in}|^2)(1 - |S_G|^2)}{|1 - \Gamma_{in}S_G|^2} \end{gathered} \tag{4.10}$$

Example: Double Matching Problem

A double matching problem is considered as shown in Fig. 4.9. It can be see that the input and output complex loads are comprised of an RL load and antenna, respectively. The matching network is designed using SRFT for the bandpass transfer function in the normalized frequency range of 0.15-0.45. The target TPG was 0.75 which is for -6dB input matching. To design a 4-element LC matching network, similar to single matching problem, initial $h(p)$ is selected to be [11111]. And following the similar procedure as discussed in the single matching problem, $g(p)$ is determined by which equalizer property is define by $E_{22} = \frac{h(p)}{g(p)}$. The MN was then comprised of LC elements by similar process of polynomial division (performed in Matlab using built in ”conv” and ”deconv” function). The input reflection coefficient is shown in Fig. 4.10. It can be seen that the matching network can provide -6 dB bandwidth covering normalized frequency of 0.13-0.45 which meets the design specification targeted initially.

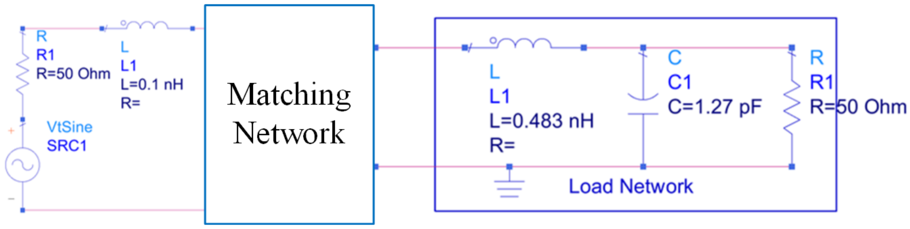

Figure 4.9: Double matching problem- schematic.

To summarize, it is obvious that SRFT can be applied to design wideband matching networks. However, it is observed that the solutions come from SRFT are not unique. And also, convergence is not guaranteed in the design procedure especially when local minimas in non-linear curve fitting are found. Intelligent genetic/neural network based algorithms can be applied in this perspective. However, it is of interest if SRFT can be used to design wideband matching networks for narrow band antenna structures. To investigate this issue, SRFT is tested with a two element narrow band MIMO antenna- described in the subsequent sections.

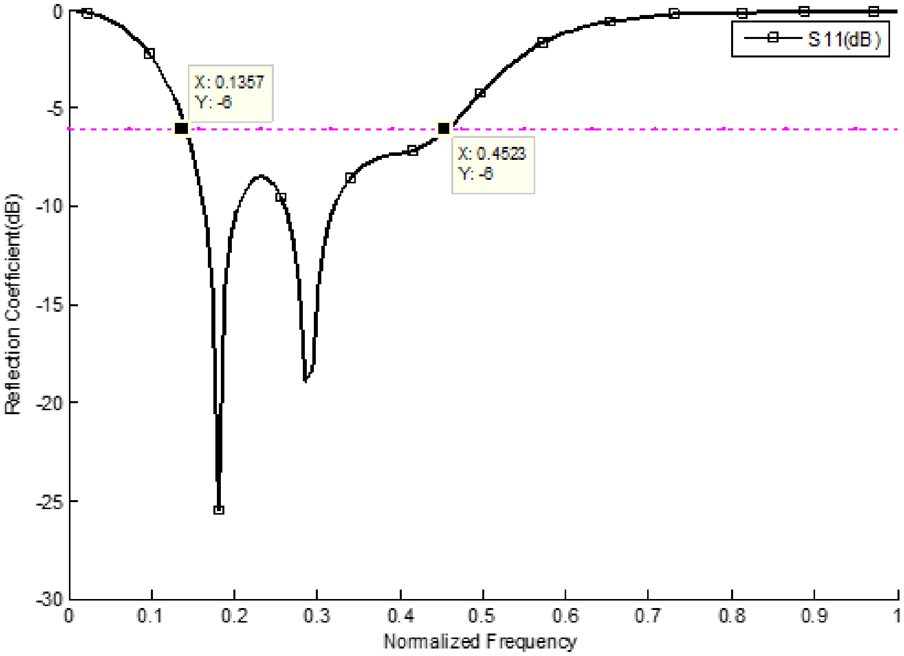

Figure 4.10: Double matching problem- estimated reflection coefficient.

4.2 Narrow Band MIMO Antenna

In this section, a detailed design description of a narrow band two element MIMO antenna is presented. Different antenna parameters are investigated. Both the measurement and simulation results are compared.

4.2.1 Antenna Geometry and Design Procedures

The proposed loaded semi-ring antenna is a derivative of the ring antenna shown in Fig. 4.11, which generally has smaller size compared to rectangular and circular patches. The fundamental resonant frequency of a ring antenna can be generally found using (4.11) where f_{11} is the fundamental frequency of resonance, C is the speed of light, ϵ_{re} is the effective relative permittivity of the substrate and X_{11} is defined as $2a_e/(a_e + b_e)$. Here, a_e and b_e are the effective inner and outer radii which are defined as $a_e = a - 3h/4$ and $b_e = b + 3h/4$ where h is the height of the substrate [101]. Thus, it is possible to set the resonant frequency of a ring antenna by changing the inner or outer ring radius. The antenna efficiency depends on the effective antenna aperture set by the effective width $W_e = b_e - a_e$ and as the W_e increases, antenna efficiency also increases [101]. However, the ring antenna shows similar resonance behavior if it is halved as shown in Fig. 4.11(b). This way, the aperture of the antenna (the semi-ring) can be increased to get higher efficiency at a specific frequency band while the total size of the semi-ring is still smaller than the full ring antenna. This leads to a compact two semi-ring MIMO antenna design without significant degradation in the antenna radiation efficiency.

$$f_{11} = \frac{X_{11} \times C}{2\pi a_e \sqrt{\epsilon_{re}}} \tag{4.11}$$

The ring antennas shown in Fig. 4.11 are generally $\lambda/2$ radiators at the fundamental frequency. The average current length can be calculated by (4.12) for the ring antenna shown in Fig. 4.11 which leads to the value of a and b approximately as 9 mm and 15 mm for a semi-ring antenna at 2.4 GHz. The input impedance of the semi-ring antenna with RO3003 substrate having $\epsilon_r = 3$, $h = 1.52\ mm$ and $\tan\delta = 0.0013$ is shown in Fig. 4.12.

$$L_{avg} \approx 2\pi(\frac{1}{3}b + \frac{2}{3}a) \tag{4.12}$$

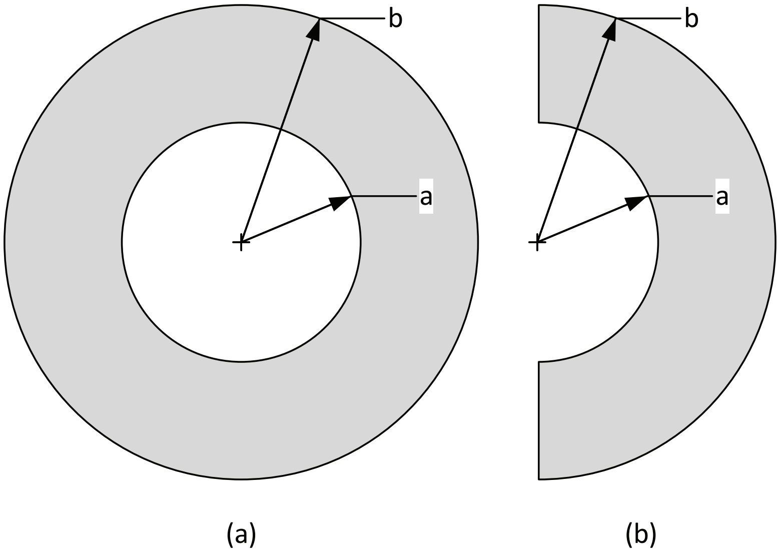

Figure 4.11: Ring antenna geometry: (a) full ring, (b) semi-ring.

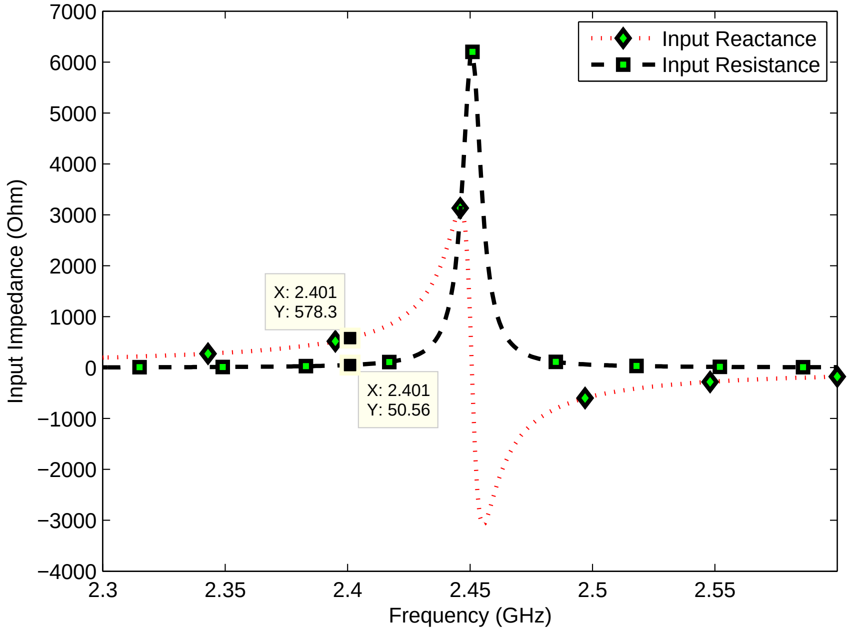

Figure 4.12: Input Impedance of a semi-ring antenna.

It can be seen that the input resistance of a semi-ring antenna is rather high at the resonance. One possible way to match the antenna to a 50 Ω input port is to move the operating frequency away from the antenna's natural frequency. However, this will require compensating the antennas reactance with a capacitive load noting that the input resistance goes down at frequencies lower than the resonance where the input reactance is inductive. As shown in Fig. 4.12, the input resistance and reactance at 2.4 GHz are 50.56 Ω and 578.3 Ω, respectively. Obviously, if the input reactance is compensated using an input capacitance, the antenna will be matched to the 50 Ω input port at 2.4 GHz.

To make the semi-ring antenna resonating at dual bands, a shorting post is introduced at the middle of the semi-ring which loads the antenna with an inductance and creates a new current path. This causes another resonance at 1.9 GHz band as shown in Fig. 4.13. At 1.9 GHz, the semi-ring acts as a $\lambda/4$ radiator which can be confirmed by looking at the current distribution and calculating the length.

However, the input resistance at the 1.9 GHz band is also very high at resonance. And at frequencies below the 1.9 GHz, the input reactance is again inductive. But the inductive reactance at 2.4 GHz and at 1.9 GHz are not equal and one input capacitance cannot match at both bands simultaneously. To have another degree of freedom in matching, an inner semi-ring is introduced as shown in Fig. 4.14. The inner semi-ring behaves like a stub matching network at both bands. The required dimension of $R3$, $R4$, W_L and P are set via a parametric study in HFSS to match a 50 Ω input port at both bands along with the value of input capacitance. Fig. 4.14b shows the input impedance behavior of the an-

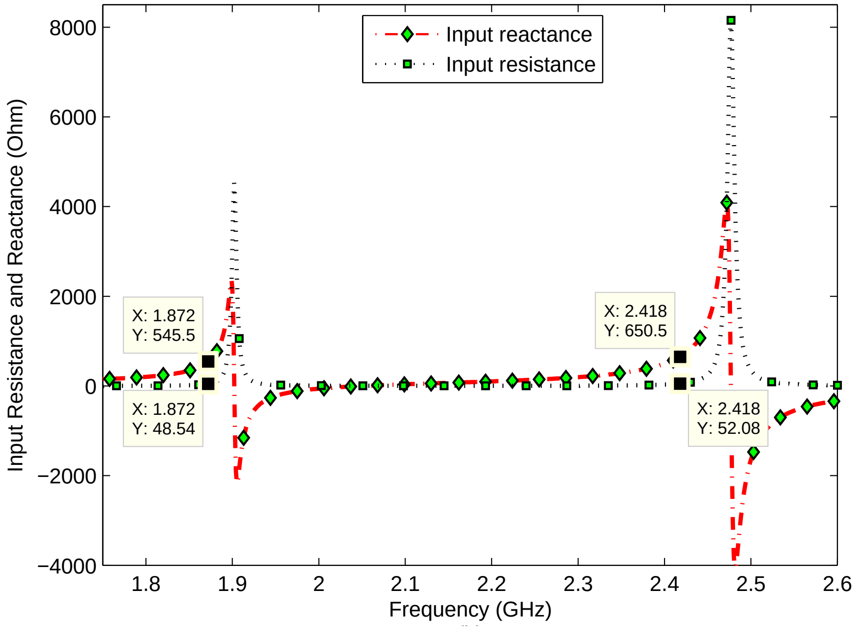

Figure 4.13: Input Impedance of a semi-ring antenna with a shorting post.

tenna structure shown in Fig. 4.14a, when the input reactance is compensated by capacitance loading and matched using the inner semi-ring. It is clear that the input capacitor will limit the operating bandwidth of the dual-band antenna system.

The current distributions of the semi-ring antenna shown in Fig. 4.14a are shown in Fig. 4.15a and 4.15b at both 1.87 GHz and 2.4 GHz, respectively. The length of the current paths are measured and found to be around 24 mm (feed point to shorting post) at 1.87 GHz and 37 mm (feed point to another end of outer semi-ring) at 2.4 GHz which are $\lambda/4$ and $\lambda/2$, respectively.

Having optimized the dimensions for a single element, the semi-ring antenna is configured in a two element MIMO structure as shown in Fig 4.16. The antenna is designed on an RO3003 substrate same as the one used for a single element.

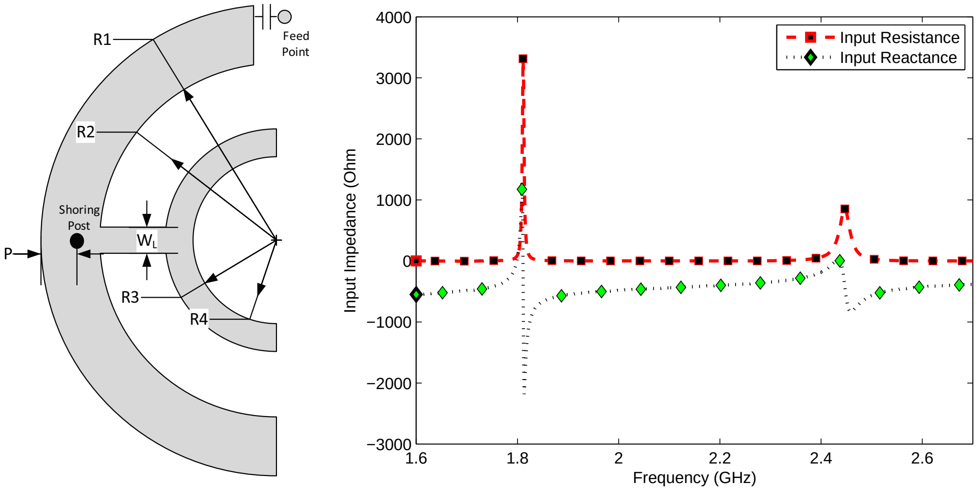

(a)

(b)

Figure 4.14: Single dual-band semi-ring antenna, (a) geometry, (b) input impedance.

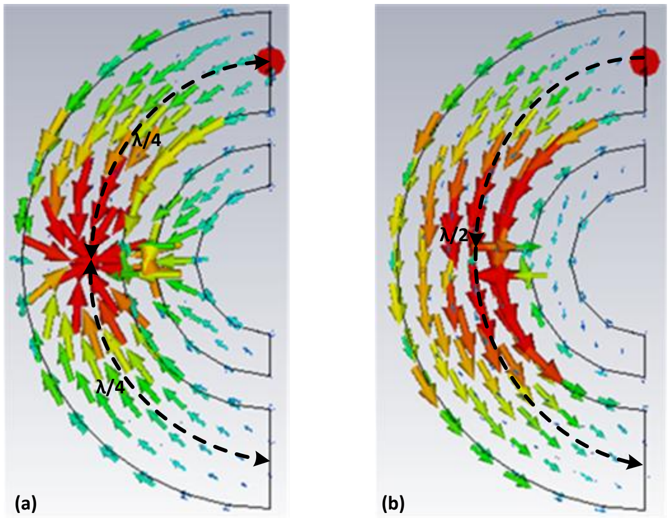

Figure 4.15: Current distribution of the dual band semi-ring antenna: (a) at 1.87 GHz and (b) at 2.4 GHz.

The substrate size of the two element MIMO antenna is $32 \times 43 \times 1.52\ mm^3$. The antenna dimensions are: $R1 = 15mm, R2 = 9mm, R3 = 7mm, R4 = 4.5mm, P = 5mm, G = 0.5mm, Gs = 1mm$ and $W_L = 1.2mm$. The separation of the two elements is optimized to be $S = 11mm$ through parametric study in HFSS for optimum isolation performance. The diameter of the shorting post is 0.6 mm. The 50 Ω feed point is matched to the high impedance half ring with an input lumped capacitance value of 0.1pF as shown in Fig. 4.16a.

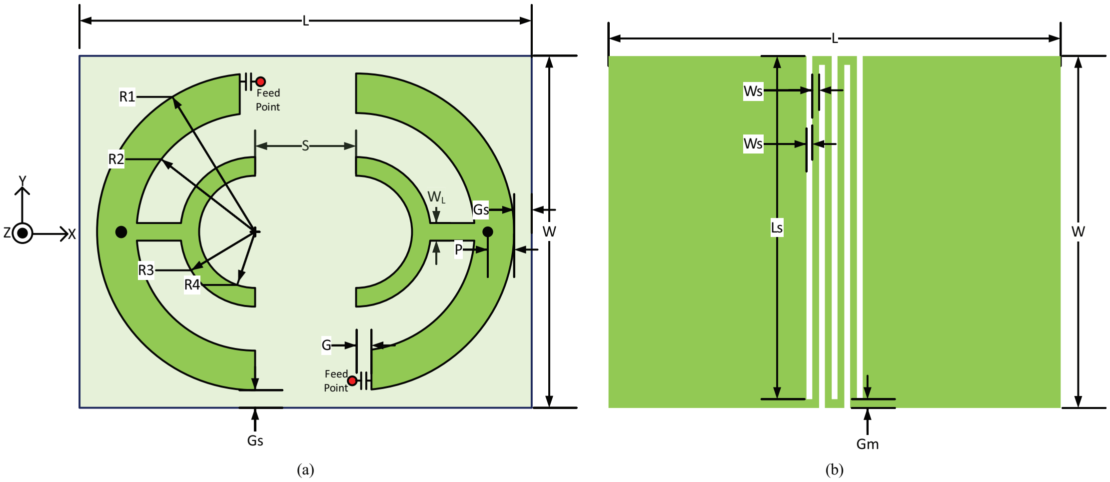

Figure 4.16: Two-element dual band MIMO semi-ring antenna with DGS: (a) top view and (b) bottom view.

To increase the isolation between the two antenna elements especially at 1.87 GHz, a meandered line DGS is designed and optimized so that the isolation at both bands is enhanced. This meander-line based DGS provides isolation enhancement at two bands when designed properly. This is to be compared with single band DGS that are usually employed. In addition, this DGS keeps the GND plane continuous between the antennas, thus, providing a common DC GND for IC biasing and return current paths.

A test setup with a transmission line for a meandered DGS structure is analyzed depending on the transmission coefficient of the structure while varying the length Ls and width Ws as shown in Fig. 4.17. Depending on the Ws and Ls

values, notches in the transmission coefficient can be placed at different frequencies. In general, Ws determines the separation between two notches while the Ls determine the frequency of the notches. If Ws is increased, the higher notch gets closer to 1.8 GHz and more separation is achieved if decreased. The parametric behavior of the DGS structure with respect to the change in Ws is shown in Fig. 4.17a. On the other hand, if Ls is increased keeping Ws constant, the two notch frequencies move to higher bands while keeping their separation almost constant and vice versa. This behavior can be observed from the parametric simulation results of the DGS structure shown in Fig. 4.17a when Ls is varied and Ws is kept constant. Moreover, the DGS is asymmetric with respect to the two feed points which causes a mutual shift in the resonance at both frequency bands especially at 1.8GHz. Such shift is a function of Ws, Ls and the separation S of the two antenna elements. Having such behavior, the dimensions of the meandered DGS is optimized as $Ws = 0.7mm$ and $Ls = 31mm$ with an optimal separation of $S = 11mm$ for better isolation at 1.87 and 2.4 GHz simultaneously.

4.2.2 Results and Discussions

The fabricated prototype of the two-element MIMO antenna is shown in Fig. 4.18. The S-parameters of the two-element antenna are measured using an Agilent N9918A vecotor network analyzer (VNA). The reflection coefficients of the two antenna elements for both simulation and measurement with the DGS are shown in Fig. 4.19. As seen from the figure, the measured results match the simulated

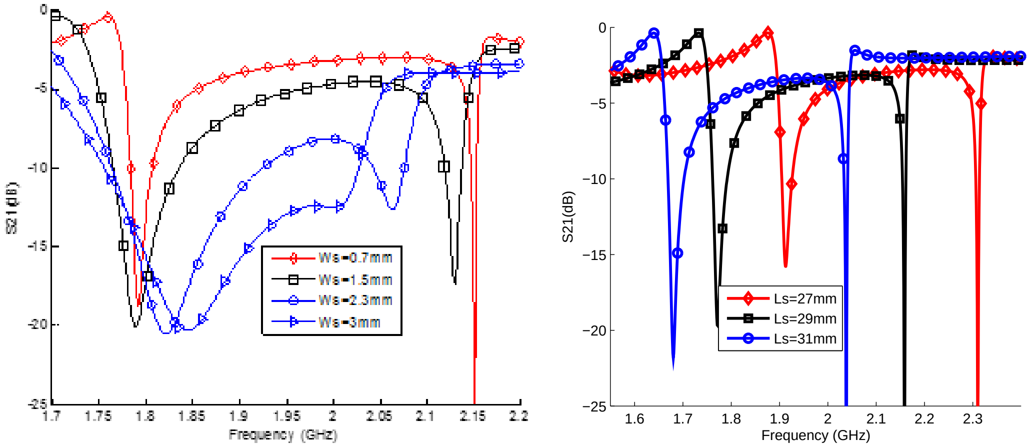

(a) (b)

Figure 4.17: (a) Effect of Ws variation on the notch frequencies, (b) Effect of Ls variations.

ones.

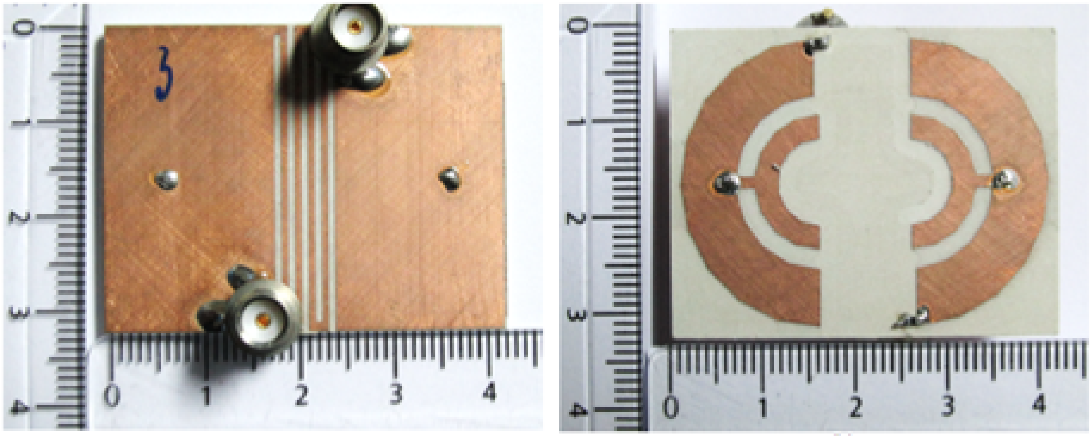

(a) (b)

Figure 4.18: Fabricated antenna model: (a) bottom, (b) top.

The measured isolation behavior between the two ports of the antenna with and without the DGS is shown in Fig. 4.20. Having the DGS, the isolation between the two ports is improved at both 1.87 and 2.45 GHz band from 3.2 dB to 13dB and from 7dB to 14.5dB, respectively. This slightly shifted the operating

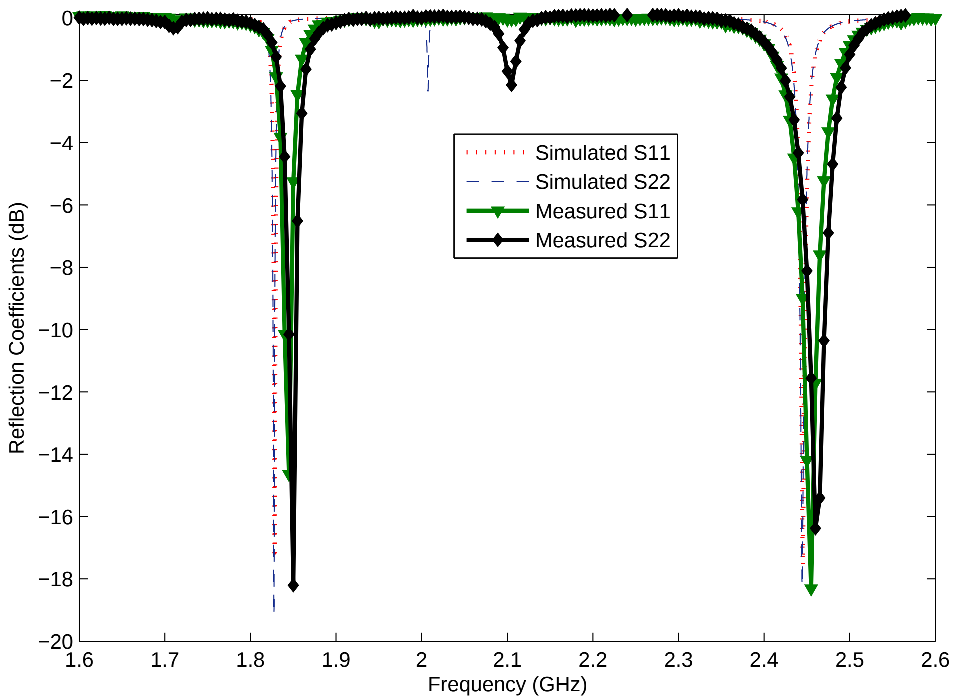

Figure 4.19: Simulated and measured reflection coefficient with DGS.

frequency. The ground plane current density plots of the antenna with and without DGS structure are shown in Fig. 4.21 when antenna element 1 is excited. The ground plane current distributions are found by keeping one port terminated with 50 Ω and exciting the other. The DGS structure significantly reduces the coupling between the two antenna elements at both bands which improves the isolation.

The measured bandwidth is found to be 15MHz at the lower band and 30MHz at the higher one. It should be noted that the antenna structure itself provides a narrow operating bandwidth (the ring antenna has a narrow operating bandwidth similar to that of a patch) and is electrically small at the lower operating band due to the miniaturization technique used, in addition the two antennas are very closely placed to minimize the overall size of the antenna system. Moreover, the

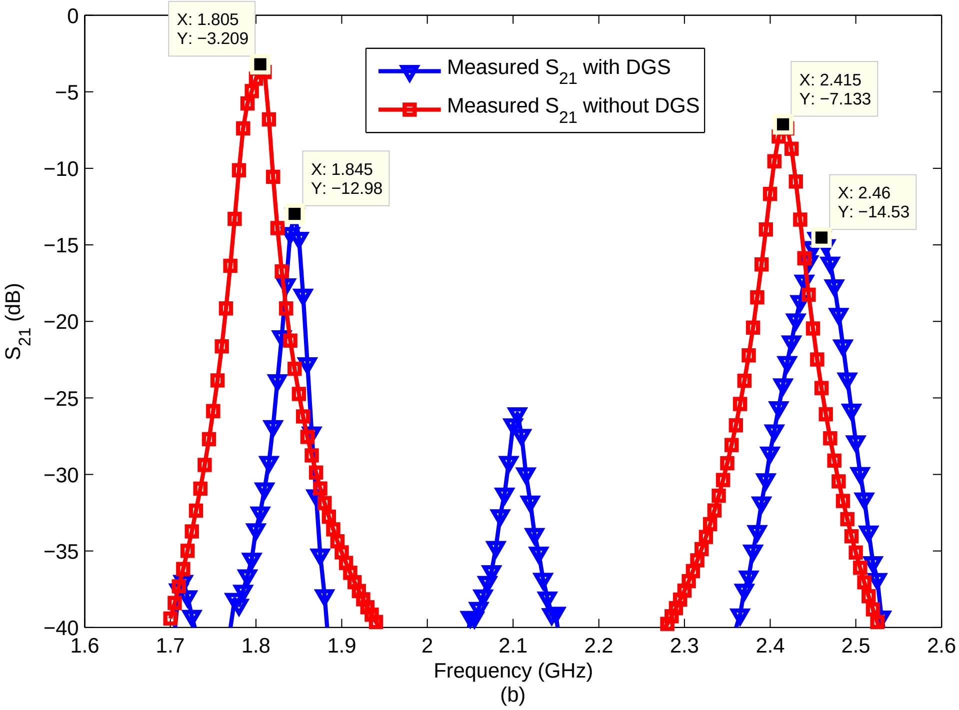

Figure 4.20: Isolation of MIMO antenna with and without DGS.

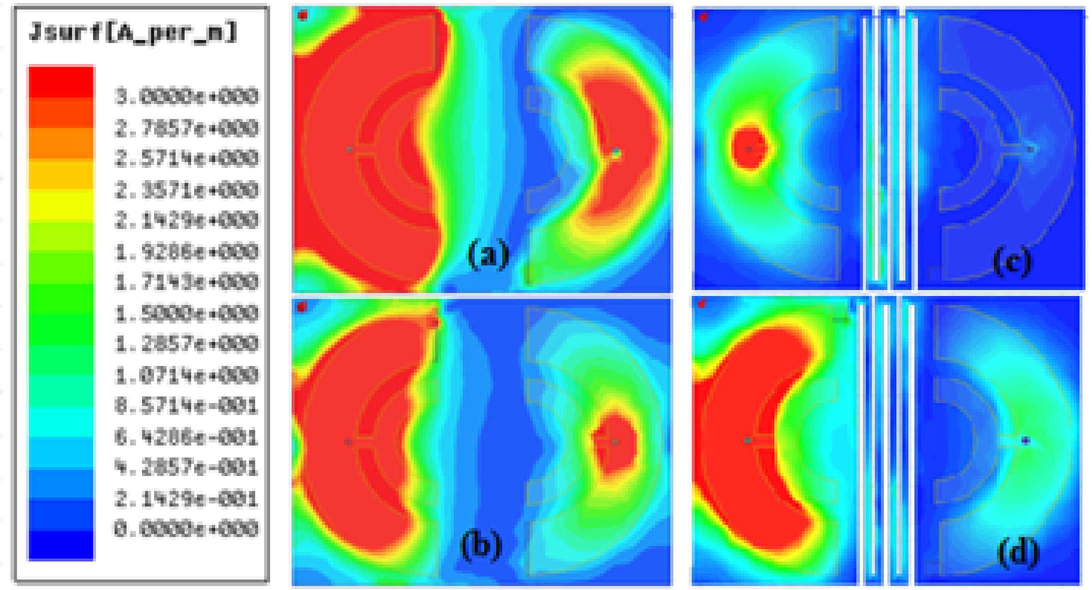

Figure 4.21: Ground plane current distribution without DGS: (a) at 1.84GHz, (b) at 2.45GHz, and with DGS: (c) at 1.84GHz and (d) at 2.45GHz when element 1 is excited.

use of the input capacitance to reduce the inductive input impedance played a major role in limiting the operating bandwidth of this antenna. The use of the input capacitor is essential for impedance matching. All of these factors lowered the bandwidth as well as the isolation (even after using the DGS, the isolation of 13dB is considered acceptable for MIMO operation, but higher isolation levels, i.e. more than 15dB are usually preferred).

The simulated gain pattern of the antenna at the lower band for antenna element1 and element2 are shown in Fig. 4.22. The maximum gain is found to be -1.93 dBi. The value of gain is a trade-off with isolation and antenna size. Without the DGS, the antenna gain is found to be 0.8 dBi which is reduced to -1.93 dBi after introducing the DGS structure. Similarly, the gain patterns of antenna element1 and antenna element 2 at 2.45GHz are also shown. The maximum gain is found to be 2.2dBi. From the gain patterns shown in Fig. 4.22, it can be observed that the radiation for each element is tilted from the other which produces lower correlation coefficient. The omni-directional radiation pattern at 1.85 GHz compared to the directional pattern at 2.45 GHz is due to the miniaturization of the antenna as we know that smaller antennas show lesser directivity. The efficiency of the two element MIMO antenna is found to be 71% at 2.45 GHz and 41% at 1.85 GHz.

The radiation patterns are measured at 1.846 and 2.461 GHz for the proposed MIMO antenna system in a Satimo Star-Lab Chamber. The 2-D normalized radiation patterns of $E_\phi(dB)$ and $E_\theta(dB)$ components for $\phi = 0^\circ$ and $\phi = 90^\circ$ plane are shown in Fig. 4.23 for antenna element 1 and antenna element 2 at both lower

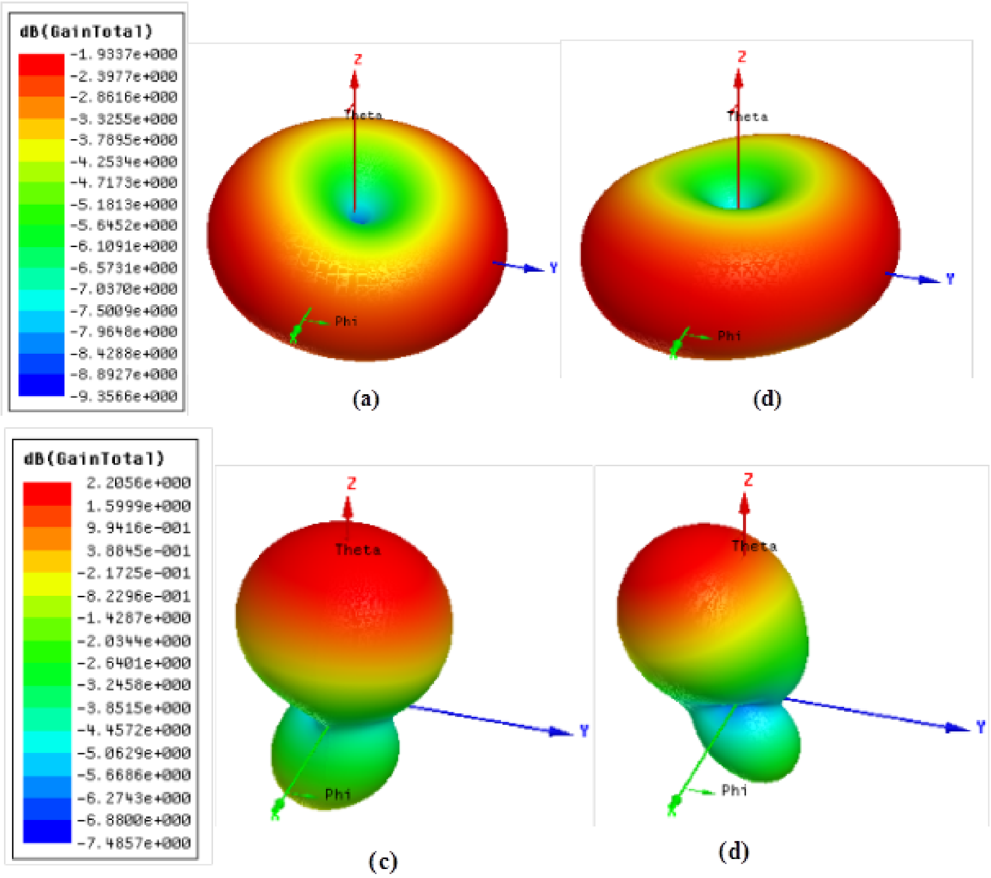

Figure 4.22: Simulated gain patterns: (a) element1 at 1.845GHz, (b) element2 at 1.845GHz, (c) element 1 at 2.45 GHz, (d) element 2 at 2.45 GHz.

and higher bands. Similarly, the normalized $E_{\phi}(dB)$ and $E_{\theta}(dB)$ components for $\theta = 90^{\circ}$ are shown in Fig. 12. Fig. 4.24. The measured maximum gain values are -2.5d Bi and 1 dBi for the two bands, respectively. These components represent the radiation field in ϕ and θ direction. Generally, co-pol and cross-pol information are intended to report by $E_{\phi}(dB)$ and $E_{\theta}(dB)$. Either $E_{\phi}(dB)$ or $E_{\theta}(dB)$ represents co-pol components which is greater than the other. For a pure linearly polarized antenna, the magnitude of co-pol component is much higher than the cross-pol component and for electrically small antennas; polarization impurity exists where co-pol and cross pol components have magnitude of same order.

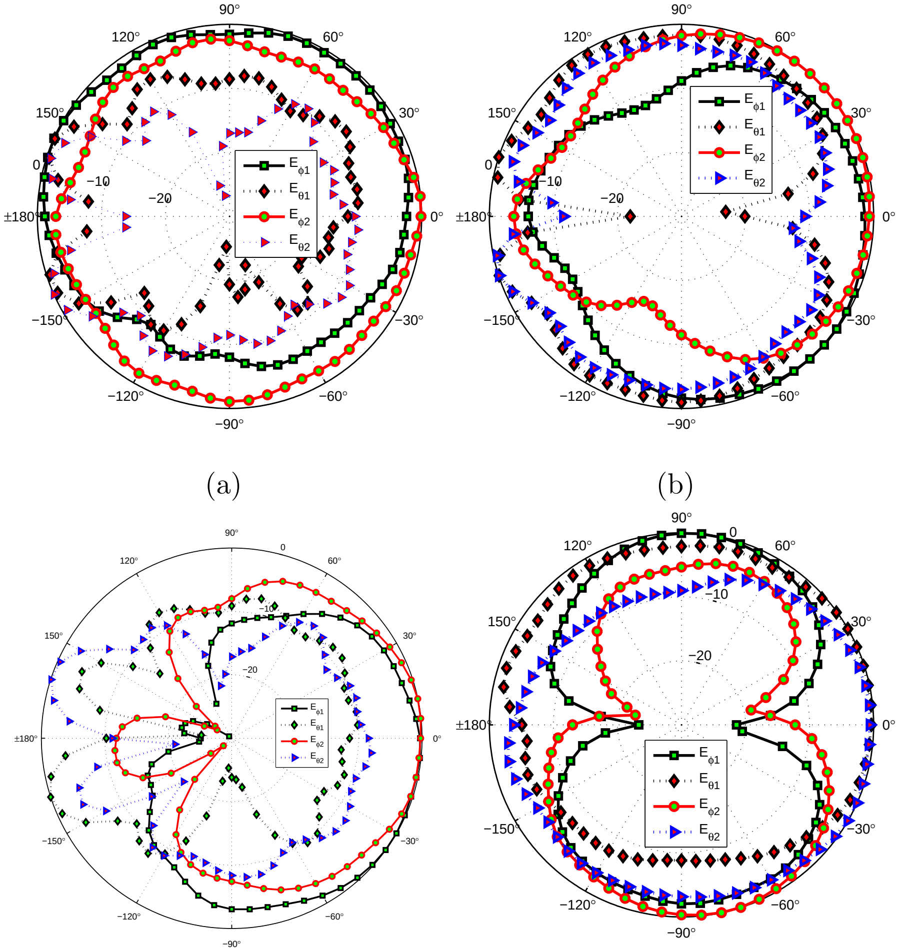

(a) (b)

(c) (d)

Figure 4.23: Measured normalized 2-D radiation patterns for: (a) at 1.846GHz $\phi = 0^{\circ}$ plane, (b) at 2.461GHz $\phi = 0^{\circ}$ plane, (c) at 2.46 GHz $\phi = 90^{\circ}$ plane and (d) 2.46 GHz $\phi = 90^{\circ}$ plane.

To evaluate the diversity performance of the MIMO antenna, ECC is evaluated from the measured S-parameters and radiation patterns as discussed in Section 2.2.3. The ECC values at different frequency points are listed in Table 4.1. For both bands, the values from measured S-parameters and radiation patterns are below the recommended value of 0.5 which gives good channel isolation behavior of the MIMO antenna for wireless communication. Note that since the proposed

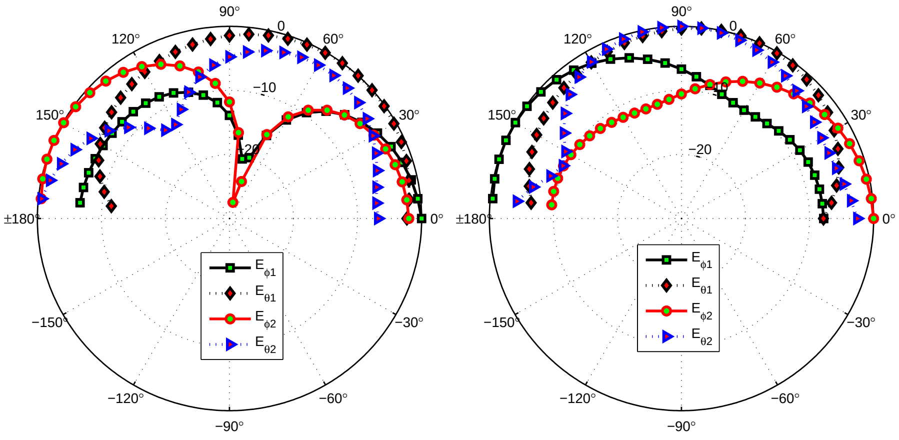

(a) (b)

Figure 4.24: Measured normalized 2-D radiation patterns for: (a) at 1.846GHz $\theta = 90^{\circ}$ plane, (b) at 2.461GHz $\theta = 90^{\circ}$ plane.

antenna is of limited efficiency (i.e. lossy), calculation of ECC from S-parameters underestimate the actual ECC value and it is imperative to evaluate ECC from radiation patterns instead. Usually cross-polar patterns are lower than their co-polar counterparts, and thus are not investigated in terms of their correlation coefficients. But if the polarization of the antenna is not pure (i.e. cross-polar and co-polar levels are comparable), then the correlation coefficient can be assessed on these patterns as well, since the receiver will be receiving comparable levels from both polarizations.

Table 4.1: Envelop correlation coefficient (ECC).

Frequency (GHz)	ECC from S-parameter	ECC from Radiation Patterns
1.837	0.1197	–
1.845	0.0300	0.2922
1.850	0.0968	–
2.440	0.0594	–
2.455	0.0097	0.2288
2.469	0.0673	–

To conclude, A dual-band semi-ring two-element MIMO antenna with enhanced isolation is designed. The MIMO antenna covers both 1.85 GHz and 2.4 5GHz band with the gain and efficiency of -2.5 dBi, 41% and 1 dBi and 71%, respectively. The isolation of the two antenna elements especially at 1.85 GHz band is enhanced using a DGS. The improved isolation is minimum 13 dB and 14.5d B at lower and higher bands, respectively. Low envelop correlation coefficients at both 1.85 and 2.45 GHz are found which promises good wireless channel behavior in MIMO environment. The prototyped design occupied $32 \times 43 \times 1.52\ mm^3$ including the two elements.

4.3 Bandwidth Enhancement Using SRFT

Overall, the two-element dual band semi-ring MIMO antenna designed in the previous section shows excellent results in terms of matching, gain, efficiency and ECC considering its compact size. However, the bandwidth of the antenna is quite low (15 MHz and 30MHz respectively at 1.85 and 2.45 GHz). It should be noted that this bandwidth limit is due to the fundamental limit of the passive structure. In this perspective, it is of interest if a matching network can be designed using SRFT so that bandwidth enhancement is possible.

To investigate the feasibility of the bandwidth enhancement, a broadband matching network is designed using SRFT. To do so, the antenna is taken as a complex load and a single matching problem is approached as shown in Fig. 4.2. However, it is not necessary in SRFT to model the antenna with a lumped component network (an advantage claimed in SRFT [96]-[100]) since the required load reflection coefficient for SRFT procedure can be easily retrieved from the HFSS simulation as port reflection coefficient. Following the procedure described in Section 4.1.2. In reality, several problems are faced while designing matching network for narrowband antenna structure:

1. First of all, the convergence of the SRFT is found to be poor compared to the other built in optimization tool for matching network design in ADS (optimization toolbox) or Optenni Lab (a software for matching circuit design for antennas).
2. The SRFT technique described in [96]-[100] cannot overcome problems due to the local minima. Moreover, the solutions found for $g(p)$ are not unique and more importantly all solutions for $g(p)$ does not guarantee achievable lumped component values (for example, some solution results of $g(p)$ give complex value for L and C which are not acceptale) and thus several trials are necessary which is time consuming.
3. Although, a matching network is developed using SRFT after several trials, it was only for single band and for multi-band operation, the solution stopped due to the local minima. Moreover, even for a single band, the optimum results are found as shown in Fig. 4.25 using 4 element matching network. Thus, -6 dB bandwidth is found to be 35 MHz and at a single band only.

To conclude, it is observed that the SRFT although can be used for wideband

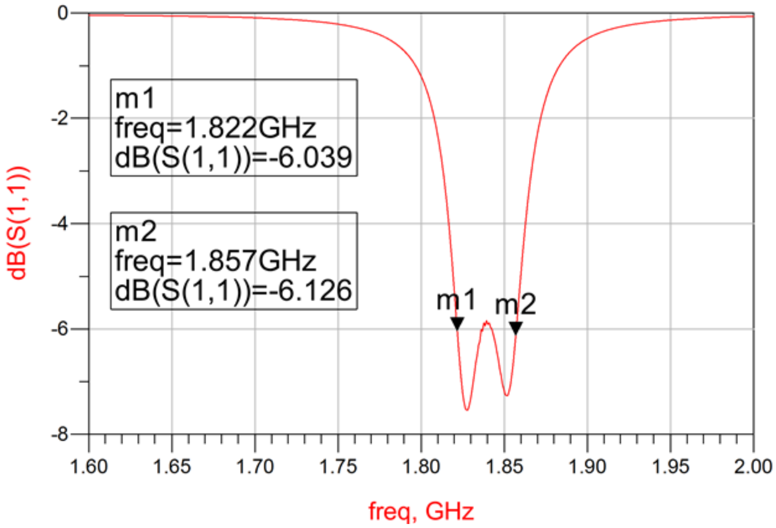

Figure 4.25: Optimum matching of the semi-ring MIMO antenna using SRFT.

matching network design but it cannot enhance the bandwidth of a load which itself is of narrow impedance bandwidth. In fact, this is expected (although bandwidth enhancement is claimed in [96]-[100]) according to the well-known Bode-Fano criterion. According to this criterion, the impedance bandwidth of a load is defined by its quality factor, Q, which was first addressed by *H. W. Bode* in 1945 [102].

$$\Delta\omega \ \ln \frac{1}{|\rho|_{max}} \leq \frac{\pi}{RC} \tag{4.13}$$

In this work, *H. W. Bode* mentioned the bandwidth limit of a parallel RC load as expressed in (4.13) where $\Delta\omega$ is the achievable bandwidth with the maximum reflection coefficient $|\rho|_{max}$. The bandwidth limit of different other passive loads are further described and generalized by *R. M. Fano* in 1950 [103]. It can be seen that for a definite passive load, the product of bandwidth and passband reflection coefficient is constant which is defined by the quality factor of the load. Thus, with passive lossless matching circuit, it is not possible to increase bandwidth keeping the matching of the load constant. That's why SRFT is not able to increase the bandwidth of a passive narrowband antenna structure. For bandwidth enhancement of narrowband structures, the non-fostering technique discussed in Chapter 3 shows excellent results. Again, it is not violating the Bode-Fano criterion. In non-fostering technique, the reactance value of the load is cancelled out by negative reactance which theoretically can give infinite impedance bandwidth as can be found from (4.13) too (C=0).

4.4 Conclusions

In this chapter, detailed wideband MN design using SRFT is presented with examples. A study on SRFT is performed to find its feasibility to design wideband matching network for narrowband antenna so that bandwidth enhancement can be achieved. It is found that the technique although can design wideband MN (subjected to the load of low quality factor) but cannot improve the bandwidth of a narrowband antenna. The reason behind is explained by Bode-Fano criterion. Moreover, the SRFT faces convergence problem due to local minima which are generally taken care by advanced algorithms in recent optimization techniques base on neural network/genetic algorithm.

CHAPTER 5

MINIATURIZED AIA: A CO-DESIGN METHOD

The interest in small antennas has been a necessity from the beginning of wireless communications. Today's multifunctional systems with compact devices further drive this interest for mobile terminals like handsets, radio frequency identification (RFID) tags among many others used for data transmission. Different approaches of antenna miniaturization like material loading, bending, folding, meandering and slot loading appeared in literature [104]. Antenna miniaturization generally presents trade-offs among gain, efficiency and bandwidth. Indeed, it is highly challenging to design miniaturized antennas with good gain, efficiency and bandwidth. Besides, difficulties are often faced when matching such miniaturized (electrically small) antennas to the consecutive stages in the wireless system (the radio frequency (RF) front-end) due to their high quality factor. Considering these aspects, antenna miniaturization techniques along with their matching procedures are of high interest to antenna and system designers.

In this Chapter, a co-design methodology for antenna miniaturization with an integrated radio frequency (RF) amplifier is proposed for efficient and compact RF front-ends. This approach relaxes the standalone antenna matching requirement which is of interest in miniaturized antenna designs. The detailed design and measurement procedure is presented and the concept is demonstrated with two examples for both narrowband and wideband scenarios considering transmitting and receiving front-ends. The amplifiers and the antennas are co-designed so that optimum performance is achieved concurrently in terms of gain, noise figure and efficiency. The antenna design example considered is miniaturized from its natural resonance frequency of 3.5 GHz to 2.45 GHz having a patch dimension of $20 \times 25mm^2$ which is equivalent to 51.1% of size reduction. The antenna has the size of $0.033\lambda_0^2$ which is smaller than [28] and offers better gain and efficiency. The bandwidth of the active antenna is at least 37 and 150 MHz for narrowband and wideband scenarios, respectively.

5.1 Transmitting AIA Simulation and Design Steps

In this work, a new approach of antenna miniaturization through the integration of RF amplifiers is presented. To prove the concept, a transmitting RF front-end is considered first for a narrowband case which is further discussed with a wideband and receiving front-end. The block diagram of a transmitting active antenna system is shown in Fig. 5.1.

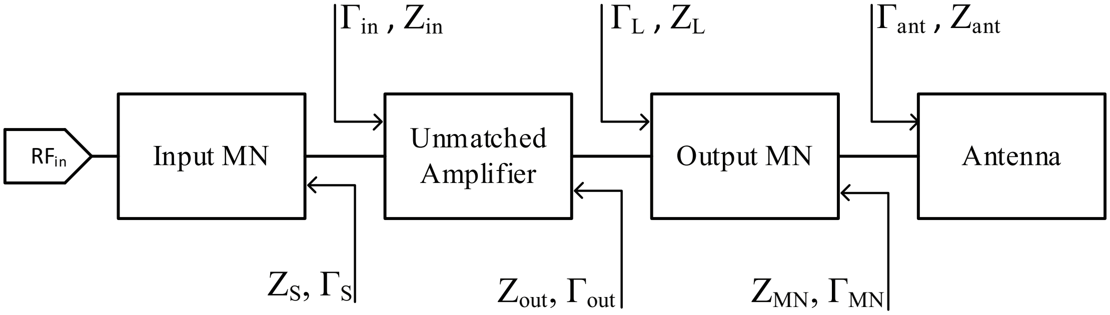

Figure 5.1: Amplifier integrated active antenna block diagram: transmitting front-end.

In the proposed AIA, the key concept toward antenna miniaturization is the conjugate matching of Z_{ant} and Z_{MN} at the band of interest. The design steps can be described as follows:

1. First, the antenna structure is modeled in an electromagnetic field solver and its reflection coefficient Γ_{ant} is obtained. In this work, Computer Simulation Technology (CST) Microwave Studio (MS) is used to model and simulate the antenna structure.

2. After amplifier stabilization, noise and gain circles are drawn over the band of interest. Based on the selected gain while having a trade-off with noise figure, Γ_S is determined. Then, Γ_{out} can be calculated according to the required Γ_S by (5.1) where S_{11}, S_{12}, S_{21} and S_{22} are the measured S-parameters of the unmatched amplifier. This optimization procedure is carried out in Advanced Design System (ADS).

$$\Gamma_{out} = S_{22} + \frac{S_{12}S_{21}\Gamma_S}{1 - S_{11}\Gamma_S} \tag{5.1}$$

3. Once Γ_S and Γ_{out} are determined, input and output matching networks (MN) are then designed and optimized to convert 50 Ω to Γ_S and Γ_{ant} to Γ_L=Γ^*_{out}.

4. For the integrated system, the antenna input port is not accessible and its reflection coefficient $\Gamma_{ant}(int)$ cannot be measured but the integrated antenna reflection coefficient can be calculated from Z_{MN} and Z_{ant} according to (5.2) where Z^*_{MN} is the complex conjugate of Z_{MN}.

$$\Gamma_{ant}(int) = \frac{Z_{ant} - Z^*_{MN}}{Z_{ant} + Z_{MN}} \tag{5.2}$$

5. To calculate the gain and noise figure of the integrated system shown in Fig. 5.1, ADS requires the system under consideration to have two ports. One possible way is to model the antenna in Fig. 5.1 with one port device having the same impedance as the antenna at a particular frequency. This will allow us to perform the complete analysis at a single frequency of the integrated system per simulation. To be able to assess the behavior over a given frequency range, CST Design Studio (DS) is used. In this work, both ADS and CST are used to get flexibility in design process. ADS is of interest in amplifier design while CST is used for the integrated system assessment.

6. Finally, the radiation behavior of the integrated system is evaluated, and

the system behavior based on the chosen parameters and designed MN is assessed along with the total system efficiency in CST. The above procedure is repeated starting from the second stage by selecting an alternative Γ_s.

Following the aforementioned procedure, the co-design of a rectangular patch and an RF amplifier is demonstrated for a narrowband case and is discussed in Section 5.2. The integrated system shows antenna miniaturization along with relaxed matching conditions for active antenna design. The co-design approach is also demonstrated considering a receiving front-end with an LNA and a slotted patch for wideband operation and is discussed in Section 5.3.

5.2 Transmitting Active Integrated Antenna

5.2.1 Antenna Characterization

The active antenna implementation process starts with measuring the S-parameter data of the antenna and the amplifier. A simple rectangular patch antenna structure is modeled in CST as shown in Fig. 5.2a with an FR4 substrate having the height of 1.52 mm, ϵ_r=4.0 and loss tangent 0.02. The fabricated prototype of the antenna is shown in Fig. 5.2b. The antenna is measured and its impedance characteristics are shown in Fig. 5.2c compared to the simulated results where it can be observed that the natural resonance frequency of the antenna occurs at 3.5 GHz. The difference between simulated and measured results can be attributed to the mismatch in material modeling and the effect of the connector.

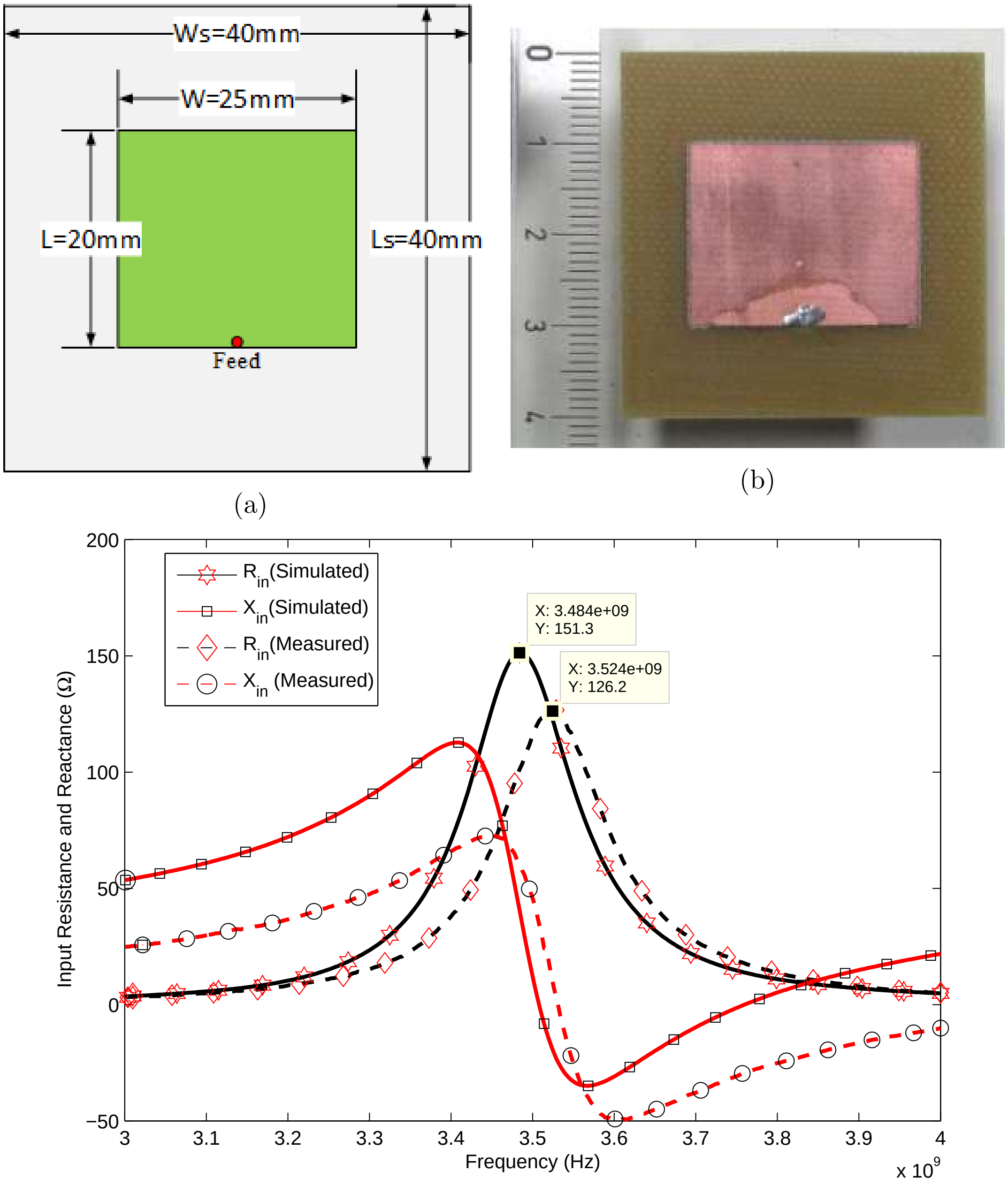

(a)

(b)

(c)

Figure 5.2: Patch antenna characteristics: (a) model, (b) fabricated prototype and (c) measured and simulated input impedance.

5.2.2 Amplifier Characteristics

In this work, a commercially available umatched RF amplifier is used from Avago Technologies (mga31689) which requires input and output MNs for optimum performance. Its S-parameters were measured by the test circuit shown in Fig. 5.3a. The fabricated prototype of the board is shown in Fig. 5.3b where low cost FR4 substrate is used with similar characteristics as the one for the antenna. The width of the transmission lines were 2.9 mm with the lengths of $TL_1 = TL_3 = 3mm$ and $TL_2 = TL_4 = 5mm$. The lumped element values were $C_1 = C_2 = 100pF$, $C_3 = 0.1\mu F$, $C_4 = 2.2\mu F$, $C_5 = 10pF$, $L_1 = 1\mu H$ and $V_{DC} = 5V$.

Based on the measured S-parameters, stability factors (Δ and k) and gain of the amplifier are calculated and shown in Fig. 5.3c. It can be seen that over the frequency band 2.2 GHz to 2.8 GHz, the amplifier is unconditionally stable since $|\Delta| < 1$ and $k > 1$. The minimum noise figure of the amplifier is found to be 1.37 dB at 2.45 GHz.

However, It is very important to de-embed the SMA connector effect from the all measured S-parameters so that the phase calculation for the integrated antenna system remains unaffected by the connector length which will affect conjugate matching severely if not properly compensated for. The SMA connectors are characterized and de-embedded from unmatched amplifier S-parameter data. To characterize the SMA connectors, they are modeled in CST as shown in Fig. 5.4a and simulated with a bandpass structure as shown in Fig. 5.4b. To make the connector characterization more accurate in the range of 2-3 GHz (since the target application was 2.45GHz), such bandpass structure ($25mm \times 25mm$) is chosen on the substrate of RO3003 (Rogers board shows well defined stable characteristicsm

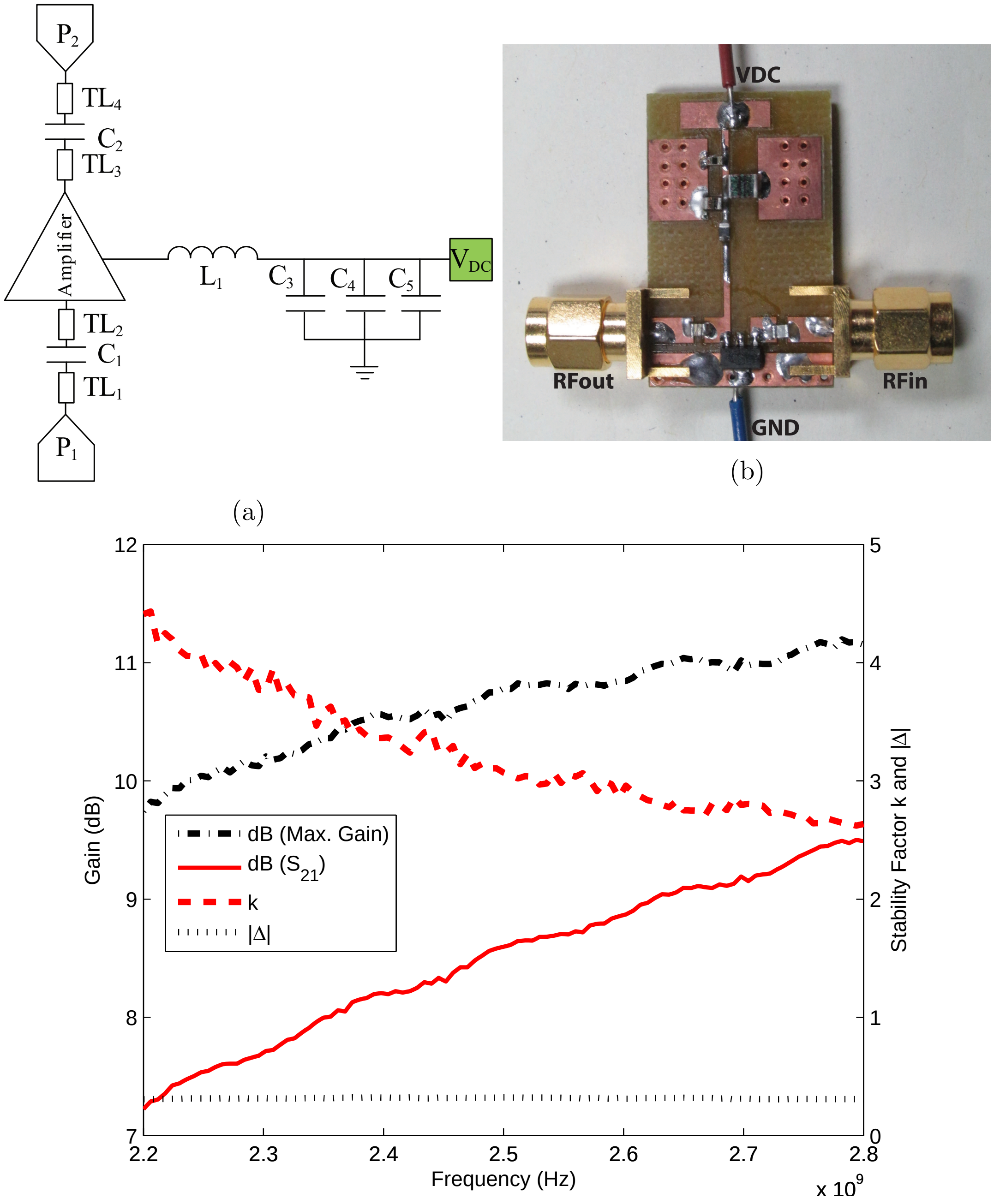

(a)

(b)

(c)

Figure 5.3: Amplifier S-parameter measurement: (a) schematic, (b) fabricated prototype and (c) measured gain and stability factors.

in terms of its loss and di-electric constant) instead of transmission lines. The fabricated design is shown in Fig. 5.5. The simulated and fabricated models are compared and thus connector S-parameters are extracted by comparing simulations and measurements using ABCD parameters. The connector S-parameters for edge SMA connector are shown in Fig. 5.6. It can be seen from Fig. 5.6a that the connectors are well matched to 50 Ω in the region of 2-3 GHz as expected which indicates the connector impedance to be 50 Ω as well. And the loss by the connector is 0 dB over the region of operation which can be neglected. The most important measurement is the phase for conjugate matching in this work which is shown in the Fig. 5.6b. From this measurement results, the connector effect can be perfectly de-embedded from the measurements will be carried later.

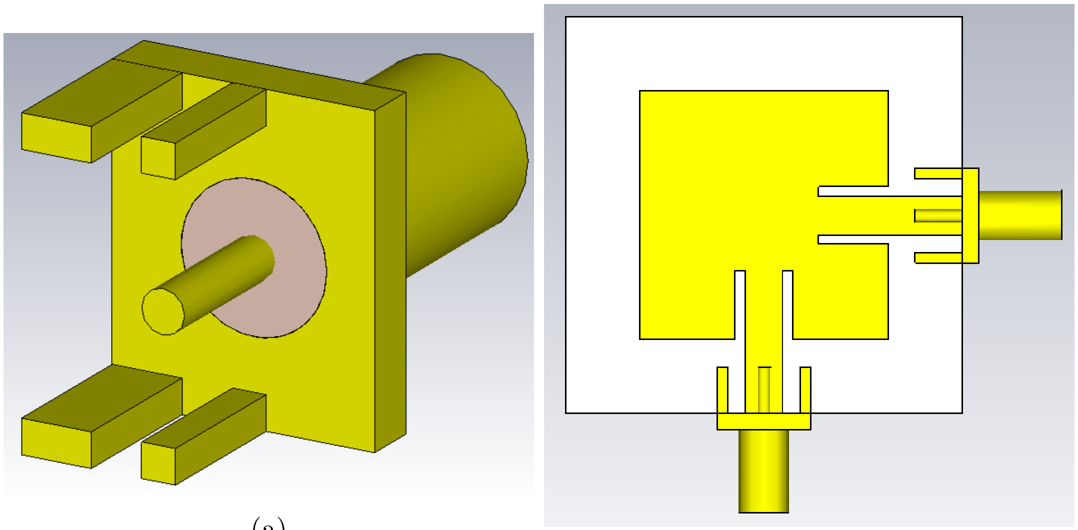

(a)

(b)

Figure 5.4: SMA connector characterization: (a) 3-d edge port SMA connector model and (b) 3-d SMA connector model simulation with bandpass structure.

The design process starts with optimized amplifier gain selection from the gain and noise circles. Fig. 5.7 illustrates different noise and gain circles at 2.45 GHz and it can be observed that different Γ_S positions can be selected by trading-off gain and noise figures. For example, at the point m1 in Fig. 5.7, gain will be at maximum while noise figure will be around 1.9 dB. In this way, Γ_S can be

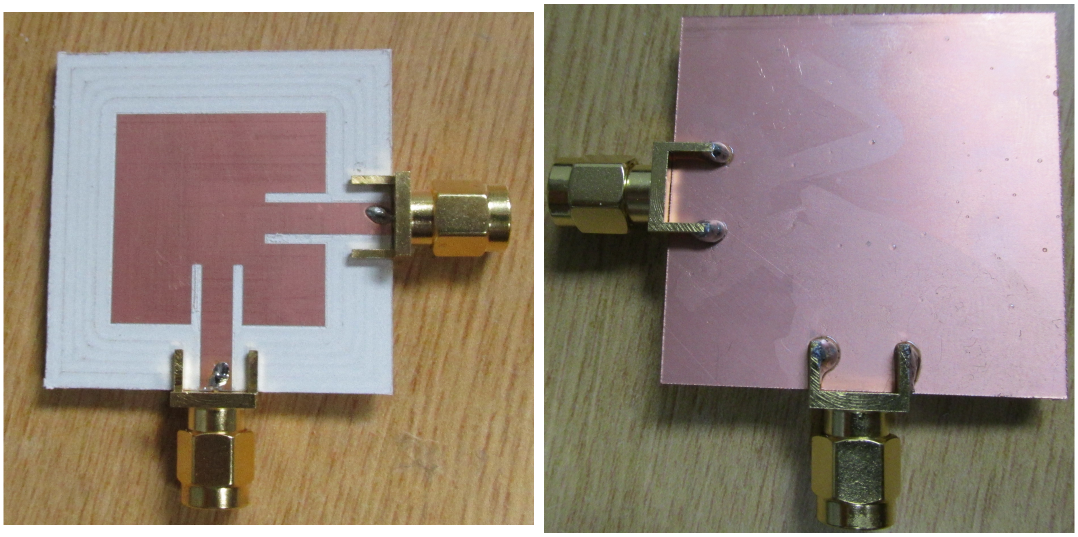

(a) (b)

Figure 5.5: Fabricated prototype for SMA edge port characterization: (a) top view and (b) bottom view.

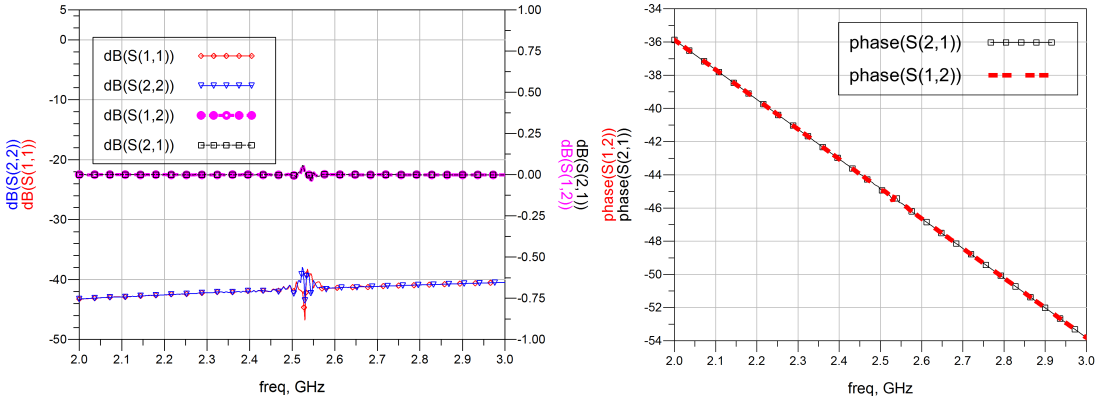

(a) (b)

Figure 5.6: S-parameters of the edge port SMA connectors: (a) magnitude plots and (b) phase plots.

selected from which Γ_{out} can be calculated using (5.1). Once Γ_S and Γ_{out} are determined, input and output MNs can be designed to match 50 Ω and Γ_{ant} to Γ_S and $\Gamma_L = \Gamma_{out}^*$, respectively. However, matching the antenna complex impedance to Γ_L might not guarantee the optimum matching at the input of the antenna over the desired frequency band of miniaturization in terms of bandwidth and radiation efficiency. Consequently, design optimization requires to provide optimum matching at the input of the antenna which is accomplished by designing the output MN so that optimum $\Gamma_{ant}(int)$ is achieved as defined by (5.2). This approach although differs from the traditional one but includes the antenna reflection as a design parameter along with amplifier gain and noise figure. Thus, optimum antenna reflection efficiency can be achieved which is crucial for the total RF front-end radiation performance.

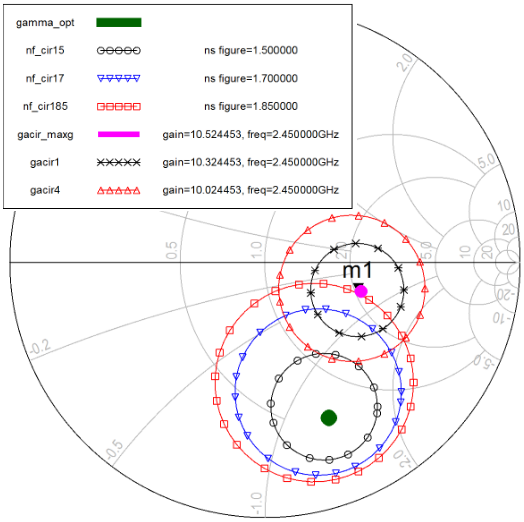

Figure 5.7: Noise and available gain circles at 2.45 GHz.

5.2.3 Transmitting AIA Results and Discussion

Based on the Z_{ant} and Z_{out} (calculated from Γ_{out}), an output MN is designed and optimized for optimum $\Gamma_{ant}(int)$ defined by (5.2) and an input MN is designed for matching the input 50 Ω port to Γ_S. After getting the optimized input and output MN, antenna reflection coefficient is calculated in ADS as described in design step 4 and the AIA system is simulated in CST as described in design steps 5 and 6 of Section 5.1. The finalized schematic of the transmitting AIA in a two port arrangement is shown in Fig. 5.8 having $TL_1 = 5mm$, $TL_2 = 3mm$, $TL_3 = 3mm$, $C_1 = 1.2pF$, $C_2 = 0.2pF$, $C_3 = 0.6pF$, $L_1 = 8.2nH$ and $L_2 = 3.9nH$ where the width of the transmission lines are 2.9 mm. It should be noted that port2 impedance in Fig. 5.8 is loaded by the measured input impedance of the antenna instead of 50 Ω. The small signal simulation results are shown in Fig. 5.9. It can be observed that the integrated antenna reflection coefficient calculated in ADS using (5.2) is almost similar to the results found from CST. The simulated bandwidth is found to be 37 MHz. The maximum simulated gain of the amplifier is found to be 8.7 dB at 2.45 GHz.

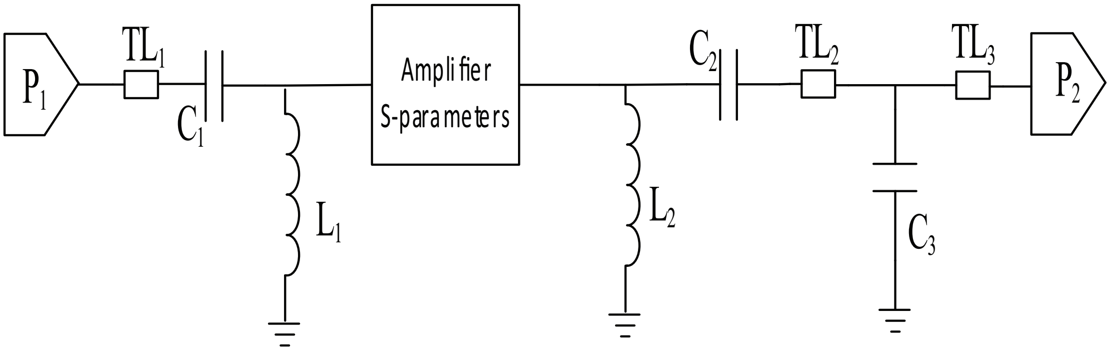

Figure 5.8: Two port simulation of AIA in CST design studio (DS).

However, after finalizing the integrated antenna circuit, it is extremely important to see the radiation characteristics of the integrated antenna. To do so, a co-simulation using CST is performed. The realized gain of the AIA at 2.45 GHz is shown in Fig. 5.10 and found to be 10.43 dBi which was − 8.36 dBi before amplifier integration when the antenna was fed with a 50 Ω input feed. This higher

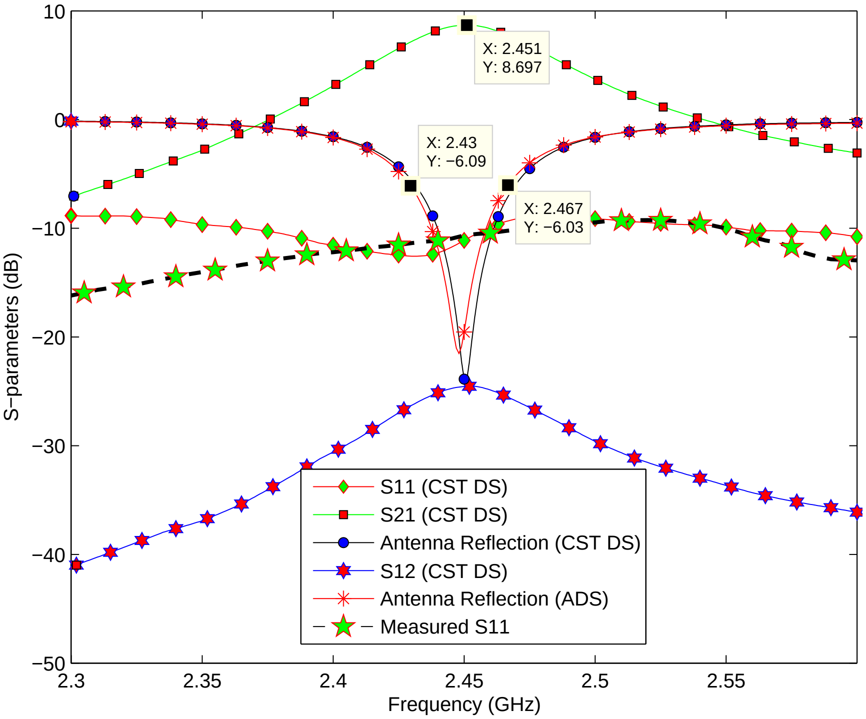

Figure 5.9: Simulated and measured S-parameters of the transmitting AIA.

realized gain of the AIA can be directly tied to the appropriate input loading of the antenna. The realized system gains at 2.43 and 2.47 GHz are found to be 10.29 and 9.42 dBi, respectively, and verify that the antenna is well matched over the operating band of the system. The standalone antenna gain after integration can be estimated from the two port amplifier gain as shown in Fig. 5.8 and integrated system gain is found by the co-simulation as shown in Fig. 5.10. Thus, antenna gain after integration at 2.45 GHz is found to be 1.73 dBi. The antenna radiation efficiencies are found to be 53.6%, 54.6% and 53.5% at 2.43, 2.45 and 2.47 GHz, respectively. From these results, it can be verified that the co-design technique presented in this paper can effectively miniaturize an antenna at a desired band by careful co-design between the active and antenna parts.

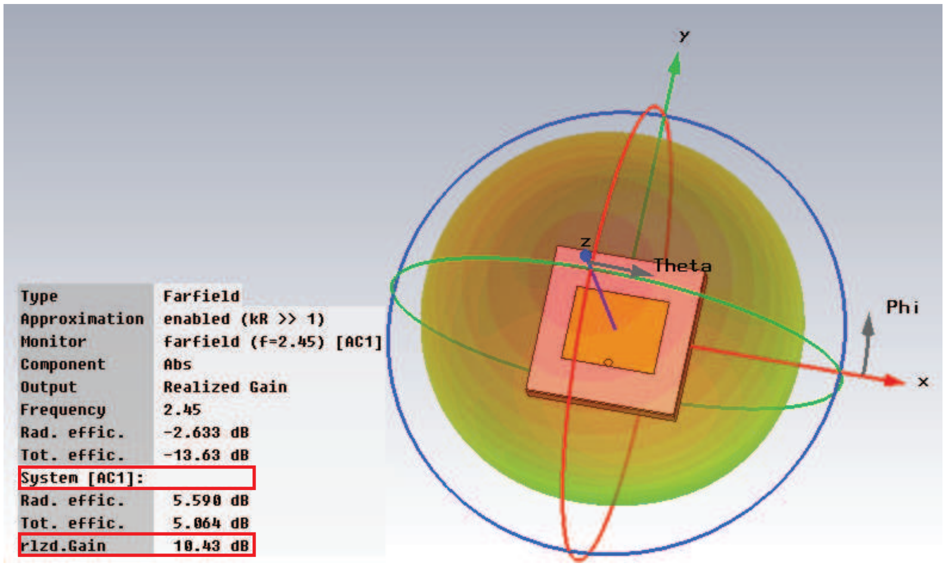

```
Type            Farfield
Approximation   enabled (kR >> 1)
Monitor         farfield (f=2.45) [AC1]
Component       Abs
Output          Realized Gain
Frequency       2.45
Rad. effic.     -2.633 dB
Tot. effic.     -13.63 dB
System [AC1]:
Rad. effic.      5.590 dB
Tot. effic.      5.064 dB
rlzd.Gain        10.43 dB
```

Figure 5.10: Realized gain of the transmitting AIA.

After finalizing the AIA system based on the simulation and analysis discussed above, an RF amplifier based transmitting prototype is fabricated as shown in Fig. 5.11. The input reflection coefficient of the integrated system is shown in Fig. 5.9. Since the input port of the integrated antenna is no more accessible, traditional S-parameters measurement cannot provide a reliable assessment of the antenna input reflection and the frequency of operation. One possible measurement setup is shown in Fig. 5.12 to check whether the integrated antenna is working fine when integrated using a vector network analyzer (VNA). In this way, far field radiation of the AIA system is observed. Thus, the transmitting AIA system gain can be calculated by observing $S_{12}(dB) = P_{Received}(dB) - P_{Generated}(dB)$ from (5.3) where free space path loss is calculated according to (5.4) [105]. The measured S_{12} is shown in Fig. 5.13 and it can be seen that the maximum power is transmitted at 2.59 GHz. The antenna system gain is measured to be 11.43 dBi at

2.59 GHz knowing the cable loss (measured), path loss and reference antenna gain to be 3 dB, 42.31 dB and 3.77d B, respectively. From this measurement setup, the frequency of operation of the AIA system can be ensured. Although the system has been designed at 2.45 GHz, the shift in the fabricated design is due to the component non-idealities (especially the FR4 substrate and lumped components) and fabrication tolerances.

$$AIA_G(dB) = S_{12}(dB) + CL(dB) - RA_G(dB) + PL(dB) \tag{5.3}$$

$$PL(dB) = 20log(d) + 20log(f) - 147.55 \tag{5.4}$$

where,

AIA_G (dB)= AIA system gain in dB

$CL(dB)$= Cable loss in dB

$RA_G(dB)$= Reference Antenna (RA) gain in dB

d= Free space separation of RA and antenna under test (AUT)

$PL(dB)$= Free space path loss in dB and

f= Frequency of interest.

After confirming the operating frequency range, the AIA system was measured in Satimo STARLAB anechoic chamber in transmitting mode as shown in Fig. 5.14. The maximum measured gain of the AIA system at 2.55, 2.57, 2.59 and 2.61 GHz were found to be 9.85, 11.52, 11.93 and 11.15 dBi, respectively. These results also show that the maximum radiation of the AIA system occurred

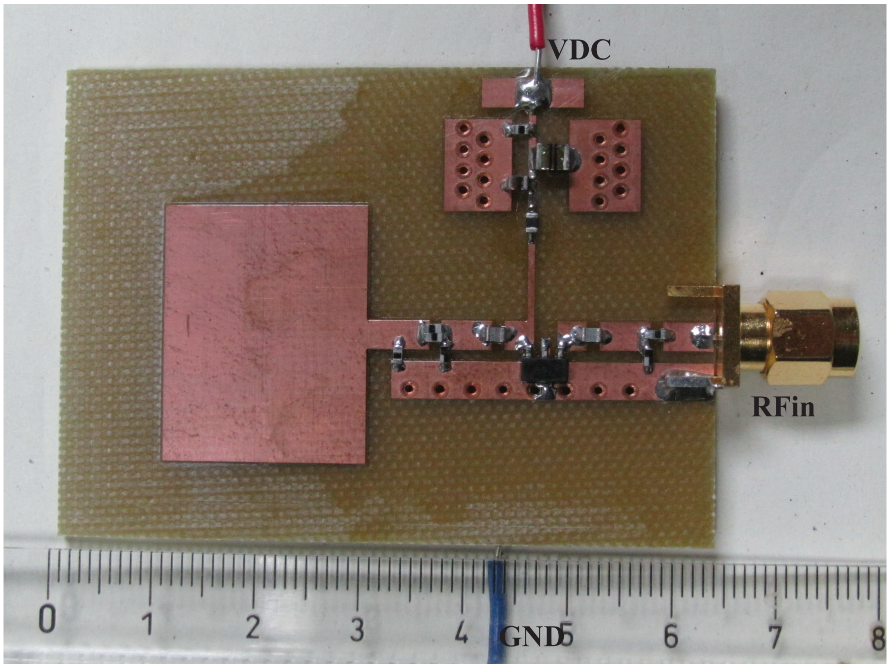

Figure 5.11: Fabricated transmitting AIA prototype.

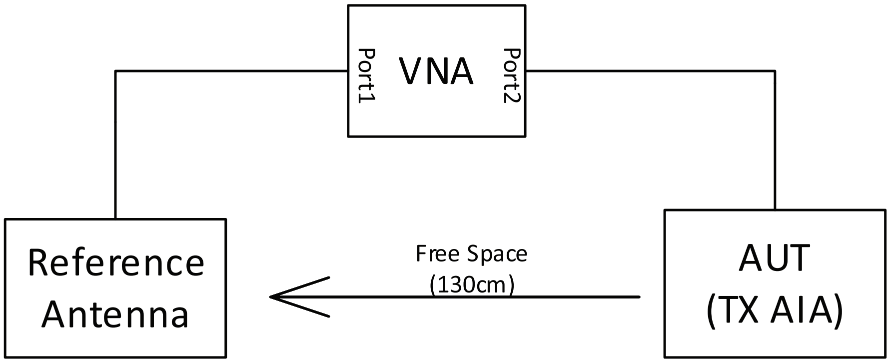

Figure 5.12: Transmitting (TX) AIA measurement setup using VNA.

at 2.59 GHz. The normalized E_θ and E_ϕ components in $\phi = 0°$ and $\phi = 90°$ of the measured transmitting AIA system are shown in Fig. 5.15. It can be seen that the co-pol components are higher than the cross-pol components by about 10 dB. The active antenna efficiency is calculated from the input and measured radiated power which is found to be more than 53% provided that the measured AIA system draws 142 mA DC current with 5 V DC supply and the amplifier has

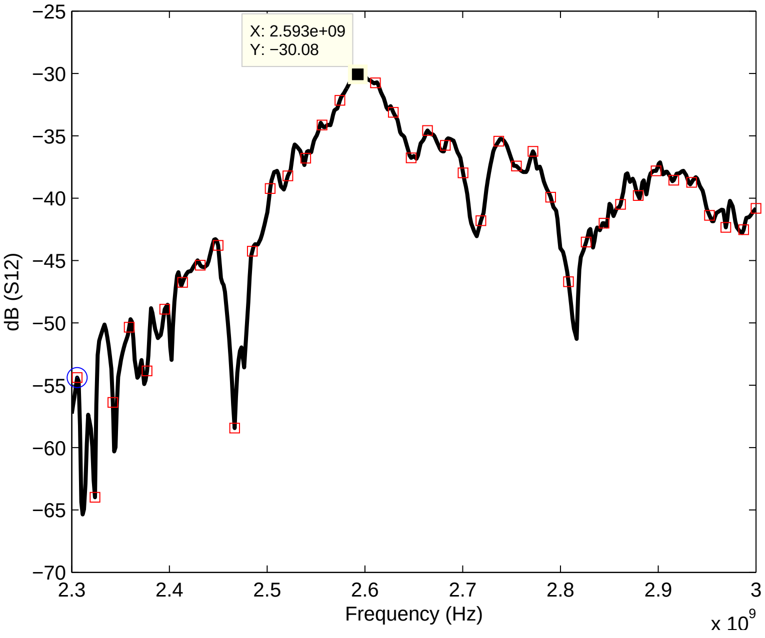

Figure 5.13: S12 of the measurement setup.

the efficiency of 48%. From all these measured results, it can be claimed that the antenna is effectively miniaturized from its nature resonant frequency 3.5 GHz to 2.6 GHz with good radiation gain and efficiency which works in the range of 2.55-2.61 GHz.

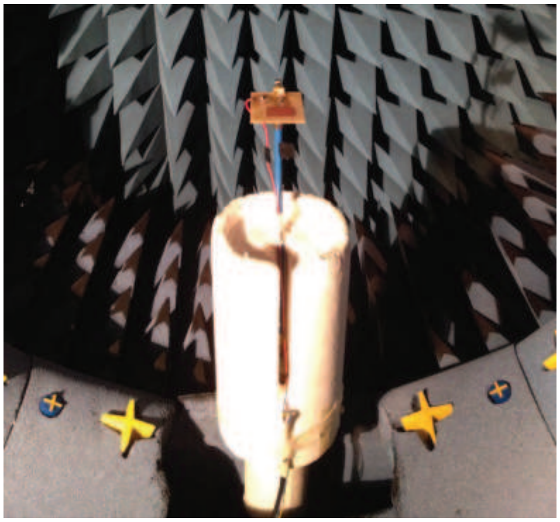

Figure 5.14: Radiation measurement setup in a Satimo chamber.

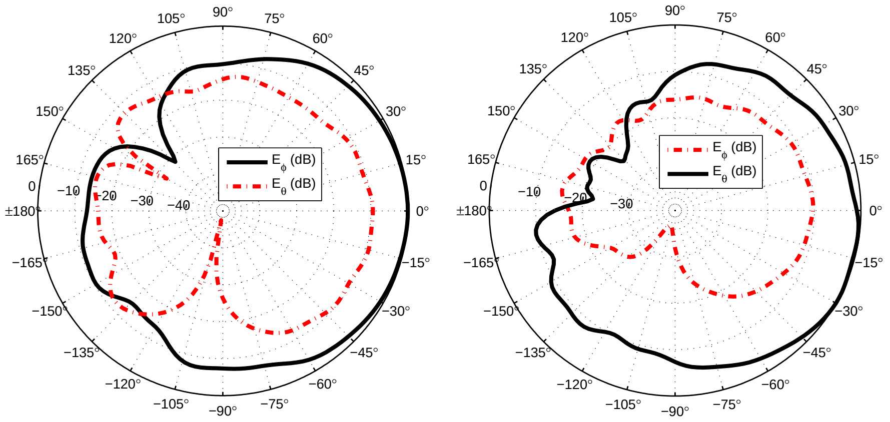

(a) (b)

Figure 5.15: Measured normalized 2-d radiation pattern at 2.59 GHz:(a) $\phi = 0°$ plane and (b) at $\phi = 90°$ plane.

5.3 Active Integrated Wideband Receiving Antenna

Because of the narrow impedance bandwidth of the simple rectangular patch antenna, the transmitting AIA system shows narrow bandwidth of operation (as shown in the previous section). To prove the applicability of the co-design process in a wideband system and also to show the procedure to be equally applicable to a receiving RF system, an LNA based slotted patch wideband AIA is also investigated.

The slotted patch antenna model and its fabricated prototype are shown in Fig. 5.16a and 5.16b, respectively. The slot in the antenna introduces dual band characteristics. By tuning the dimensions of the slot, the current paths can be varied and it is possible to bring them closer thus providing wideband behavior. The antenna impedance characteristics are measured and shown in Fig. 5.16c. It is observed that the antenna shows same normalized impedance of 0.045+0.495j at 2.45 and 2.6 GHz and if compensated for the reactance, dual resonance behavior can be achieved. The AIA design approach takes care of this mismatch and compensation which relaxes the standalone antenna matching requirement. The measured antenna characteristics are used for the LNA design procedure instead of simulated characteristics to avoid FR4 material tolerance. It should also be noted that the antenna is measured with a 3 mm transmission line to take into account the effect of the transmission line feeding when integrated with the LNA.

The LNA based AIA system block diagram is shown in Fig. 5.17. To optimize the integrated antenna performance in terms of its bandwidth, realized gain and total efficiency, the antenna reflection at its input ($\Gamma_{ant}(int)$) defined by (5.2) is crucial which depends on Γ_{in} and sequentially Γ_L. As a consequence, design optimization starts by the selection of Γ_L in the load plane from a set of operating gain circles instead of the available gain circles which define Γ_S to be the conjugate of Γ_{in} calculated from (5.5). Thus, for every set of Γ_L and Γ_S, different integrated antenna reflection, noise figure and operating gain are observed and the input MN is finalized based on their optimum values. After getting the optimized Γ_L, an output MN is designed to see the 50 Ω RF output port to be Γ_L.

$$\Gamma_{in} = S_{11} + \frac{S_{12}S_{21}\Gamma_L}{1 - S_{22}\Gamma_L} \tag{5.5}$$

The optimized LNA based AIA schematic is shown in Fig. 5.18 with the same unmatched amplifier (mga31689) as in the previously designed transmitting AIA

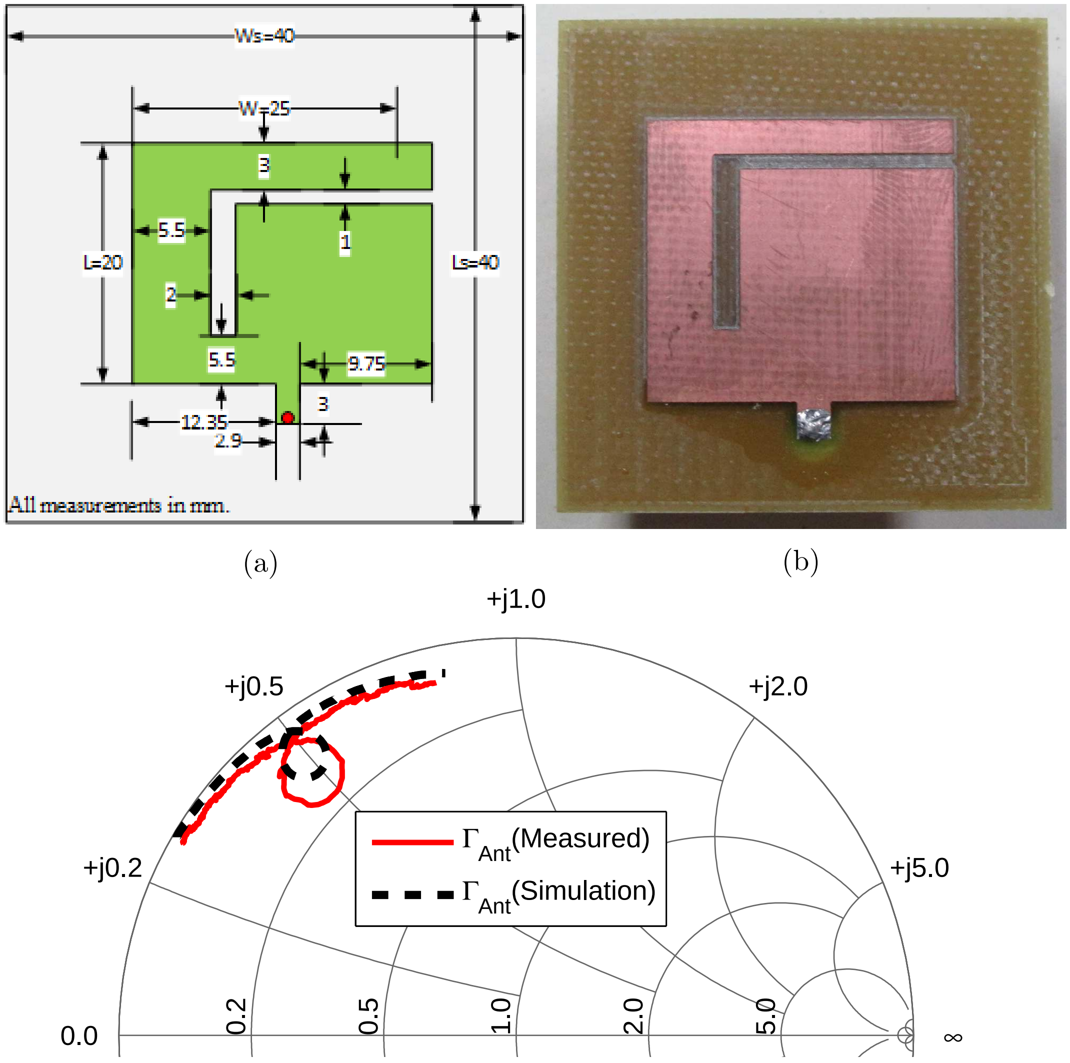

(a) (b)

(c)

Figure 5.16: Slotted patch antenna: (a)model, (b) fabricated prototype and (c) measured and simulated reflection coefficient.

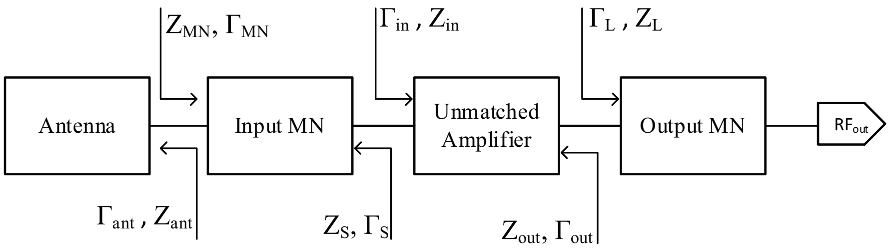

Figure 5.17: LNA based AIA system block diagram: Receiving mode.

with $TL_1 = 3mm$, $TL_2 = 5mm$, $TL_3 = 5mm$, $C_1 = 1pF$, $C_2 = 2.1pF$, $C_3 = 1pF$, $L_1 = 68nH$ and $L_2 = 3.9nH$ where the width of the transmission lines are 2.9 mm. It should be noted that the port1 impedance is loaded as the complex antenna impedance to evaluate the receiving AIA system performance in a continuous frequency band. Simulated and measured S-parameters of the LNA based AIA when integrated are shown in Fig. 5.19. It can be seen that the integrated antenna covers 2.45-2.6 GHz. The amplifier shows approximate flat gain of 10 dB in the operating frequency band. The noise figure simulation is performed in ADS at discrete frequencies and found to be less than 1.7 dB. The radiation characteristics of the AIA system is evaluated by cosimulation. The realized gain is found to be 11.9 dBi at 2.45 GHz which was -8.86 dBi before integration (i.e with 50 Ω termination). The increased realized gain proves the well matched behavior of the integrated antenna at 2.45 GHz.

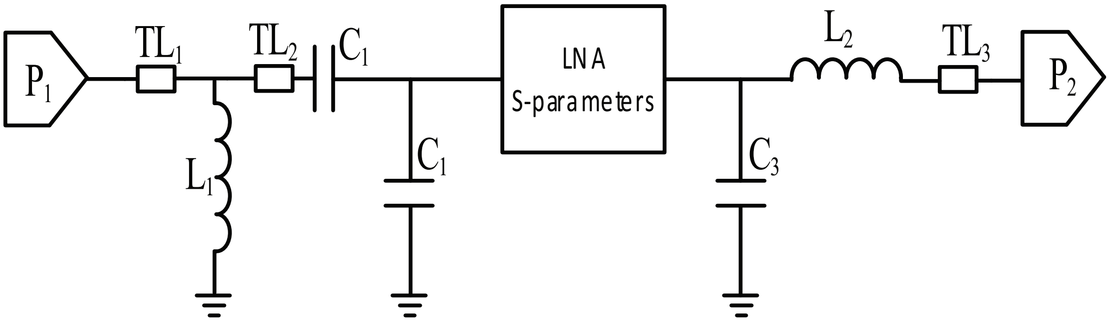

Figure 5.18: LNA based two port receiving AIA schematic.

The fabricated receiving AIA prototype is shown in Fig. 5.20. A similar test as shown in Fig. 5.12 is performed (AUT is in receiving mode this time and S21 is evaluated instead of S12) and found that the integrated active antenna

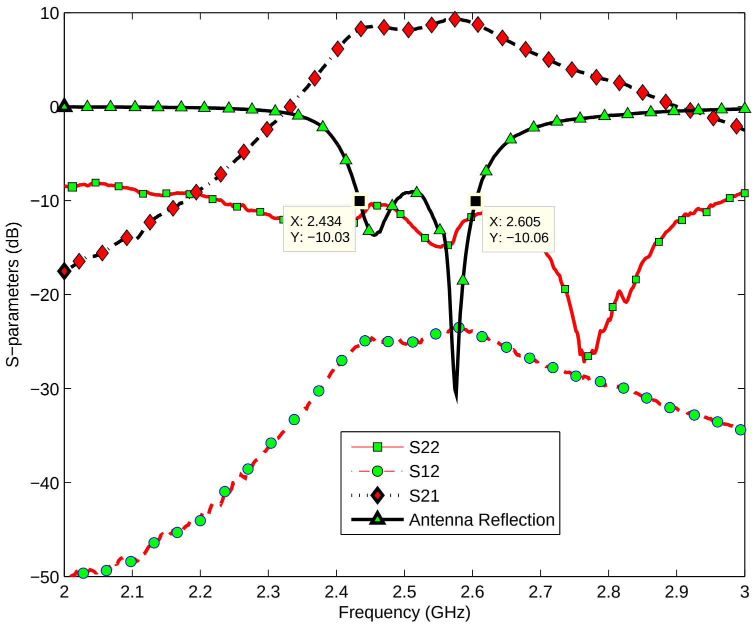

Figure 5.19: Simulated and measured S-parameters of LNA based AIA.

system operates with the designed performane from 2.45 GHz-2.6 GHz and the AIA gain is found to be more than 9.5 dBi over this band. The AIA system radiation characteristics were then measured in an anechoic chamber in receiving mode. The system gains were 10.87 and 9.87 dBi at 2.45 GHz and 2.55 GHz , respectively. The efficiency of the integrated antenna is calculated from the input power (received by the antenna) and output power which is found to be 47% and 51% in the two bands, respectively, provided that the measured AIA system draws 157 mA DC current with 5 V DC supply. The normalized co-pol and cross-pol components of the measured LNA based AIA are shown in Fig. 5.21 at 2.45 and 2.55 GHz. The antenna is linearly polarized and it can be seen that the co-pol components have around 7 dB higher magnitude than the cross-pol components.

From the simulation and measurement results found for the both transmit-

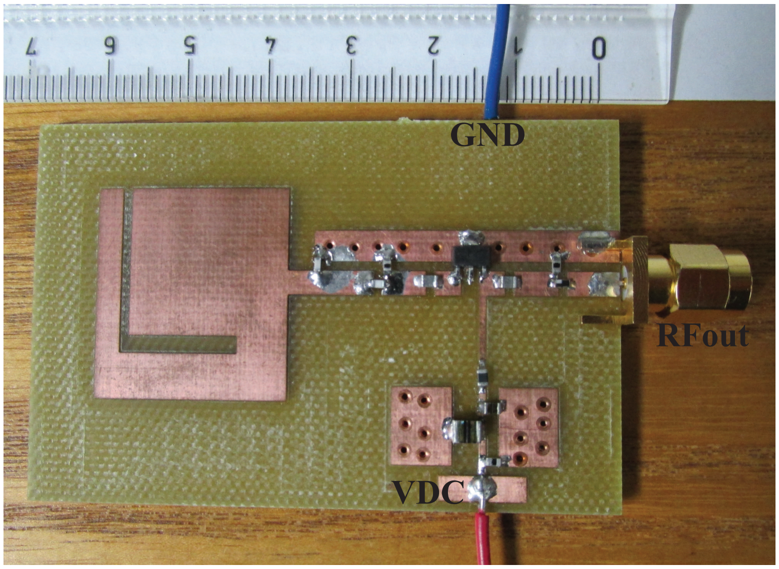

Figure 5.20: Fabricated LNA based AIA prototype.

ting and receiving AIAs presented, it can be claimed that the co-design approach prsented in this work shows a generic and effective antenna miniaturization technique with good gain and efficiency. The measured results for both transmitting and receiving AIA systems are summarized in Table 5.1. To estimate the standalone antenna gain after integration, two port systems as shown in Fig. 5.8 and Fig. 5.18 were measured by two test boards where the matching networks were designed to transfer the 50 Ω port impedance to the equivalent Γ_L and Γ_S at the frequencies 2.59 GHz and 2.45 GHz for transmitting and receiving systems, respectively. Thus, amplifier gains can be measured at a single frequency and antenna gains can be estimated from the overall measured system gains. It can be seen that the proposed miniaturized active antenna has 20% smaller size compared to the active antenna reported in [28] but provides better gain (1.91 dBi compared to -0.77 dBi). This improvement is attributed to the co-design approach

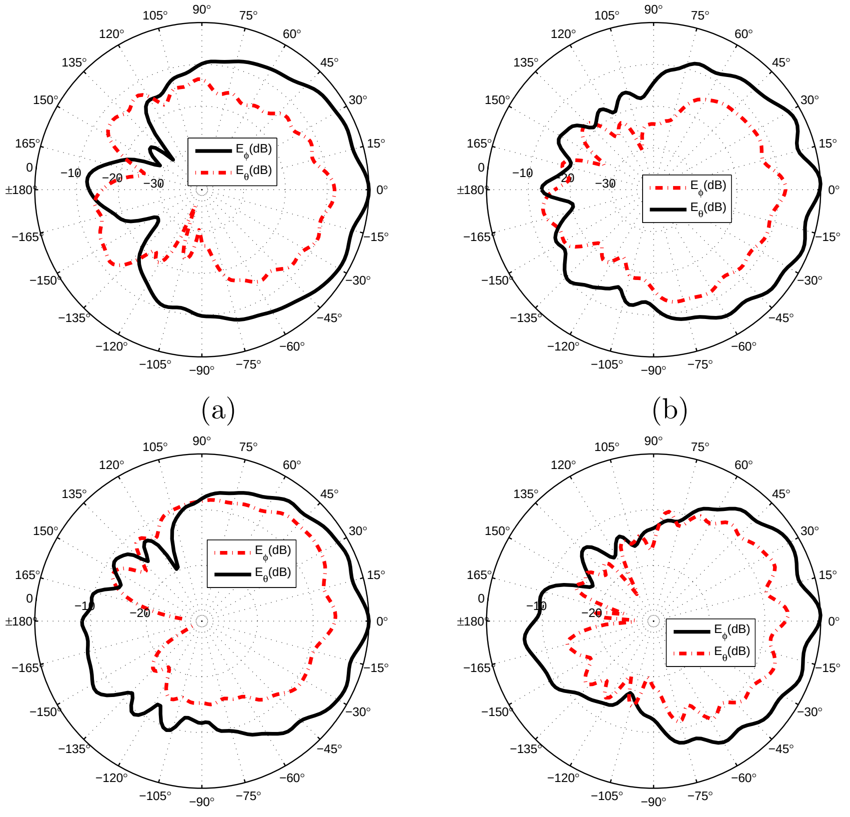

(a) (b)

(c) (d)

Figure 5.21: Measured 2-D radiation patterns: (a) $\phi = 0°$ plane at 2.45 GHz, (b) $\phi = 90°$ plane at 2.45 GHz, (c) $\phi = 0°$ plane at 2.55 GHz and (d) $\phi = 90°$ plane at 2.55 GHz.

which ensures better input reflection efficiency of the antenna and subsequently provides higher antenna efficiency and gain (Total efficiency and realized gain can be found from: $\eta(total) = (1 - \Gamma^2) \times \eta(rad)$, G(realized)=$\eta(total)$×Directivity).

Table 5.1: Summary of the measured performance metrics of the transmitting and receiving AIA systems.

Parameters	Transmitting AIA	Receiving AIA
Max. System Gain	11.93 dBi at 2.59 GHz	10.87 dBi at 2.45 GHz
Noise Figure	<1.9 dB	<1.7 dB
Antenna Efficiency	>53%	>47%
Antenna Gain	2.1 dBi at 2.59 GHz	1.91 dBi at 2.45 GHz
Bandwidth	2.55 GHz-2.61 GHz	2.45 GHz-2.6 GHz

5.4 Conclusions

A new approach to antenna miniaturization is introduced through the co-design with RF front-ends. Two examples are considered based on RF amplifier integration for narrowband and wideband antenna structures, respectively, where the antenna is miniaturized from its natural resonance frequency of 3.5 GHz to 2.45 GHz which is a size reduction of 51%. The miniaturization technique presented here also relaxes the antenna matching requirement which is crucial for small and compact antenna designs. Step by step procedures for designing, simulation and measurements are presented. Measurement results show the AIA systems to work effectively in the band of 2.45-2.6 GHz having the overall system gain of more than 10 dBi and efficiency more than 47%. Standalone antenna gain is calculated to be more than 1.9 dBi in the operating band. Such antenna miniaturization scheme along with relaxed antenna matching is highly desireable for compact integrated RF system design.

CHAPTER 6

ACTIVE INTEGRATED UWB MIMO ANTENNA

MIMO technology has received significant interest in recent years because of its exotic features like providing high data throughput, better transmission quality and increased coverage. The design of antennas for these MIMO systems is a challenging task. On the other hand, due to the requirement of low power, low cost and multi-functionality, ultra-wideband (UWB) wireless systems are highly desirable. Thus, the demand for compact UWB MIMO antennas that are suitable for low cost, low power and multifunctional high speed mobile terminals is on rise. In this chapter, a compact UWB two-element MIMO antenna structure is presented with its design details and integration of an RF amplifier with UWB antenna structure is examined for several design advantages like: 1) enhanced port isolation, 2) improved impedance matching of the antenna and 3) improved total radiation efficiency and realized gain. A co-design approach will be followed based on the procedure devised in Chapter 5.

6.1 UWB Antenna Design

Designing a UWB MIMO antenna is highly challenging considering the size of the device and different MIMO antenna parameters especially port isolation and envelop correlation coefficient (ECC). Mutual coupling between MIMO antenna elements degrades the isolation and ECC which consequently affect the radiation efficiency and diversity of the antenna. Although, different techniques are found in literature for reducing mutual coupling like neutralization lines, defected ground structure (DGS), decoupling networks and material loading [9], these methods are narrowband in nature. Thus, it is highly challenging when considered for a UWB scenario. In this section, a UWB antenna structure is presented covering 1.85-10.6 GHz band. Such antennas allows integration of GSM/LTE/WLAN bands with UWB that can provide lucrative features like simultaneous sensing and communication.

6.1.1 Proposed Antenna Geometry

The proposed antenna geometry is shown in Fig. 6.1. It is designed on an FR4 substrate with height, dielectric constant and loss tangent of 1.52mm, 4.0 and 0.02, respectively. It can be seen from Fig. 6.1 that the overall size of the MIMO antenna system is $50 \times 90mm^2$ and each radiator has the size of $12 \times 24mm^2$. The antenna is fed by a $6.5 \times 2.9mm^2$ transmission line where the width of 2.9mm is optimized for better impedance matching over the whole operating band 1.85-10.6 GHz. The antenna was modeled and optimized using CST.

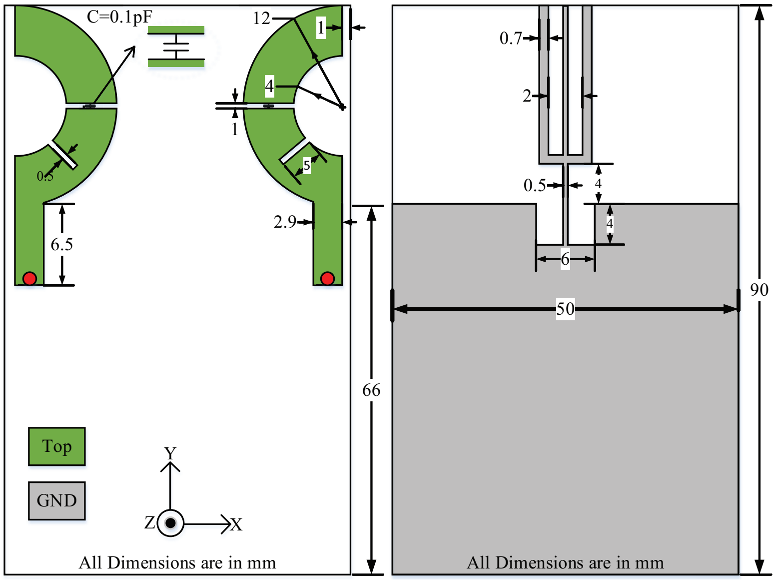

Figure 6.1: Proposed antenna geometry.

The UWB impedance bandwidth of the antenna is realized by manipulating the radii of the inner and outer circles by which the semi-ring is formed. By varying these two parameters, two different modes can be excited. UWB impedance bandwidth can be obtained if these modes are merged. The reflection coefficient and isolation curves of the two-element semi-ring MIMO antenna are shown in Fig. 6.2 and 6.3, respectively. It can be seen from Fig. 6.2 that the semi-ring shows UWB impedance bandwidth over the frequency 1.7-10.6 GHz (this is -6 dB impedance bandwidth, but if -10 dB is considered, the range covered is from 1.7-2 GHz and 3-10.58 GHz). But, the isolation of the semi-ring is less than 10 dB over the band 1.8-3 GHz and 4-5.2 GHz as can be seen from Fig. 6.3. In this work, a fork shaped structure in the ground plane is used to improve the isolation as shown in Fig. 6.1. The structure generally works as a resonant structure and a reflector that reduces mutual coupling. Thus, it improves port isolation and envelop correlation coefficient. The middle arm of the fork improves isolation around 2 GHz which is optimized by varying its width and length and it can be seen from the Fig. 6.3 that the isolation is improved to 30 dB from its initial value of 6dB. On the other hand, side arms of the fork improves isolation around 4-6 GHz. However, fork structure affect the -10 dB impedance bandwidth by its reactive effect as can be observed from Fig. 6.2. With the fork structure in the ground plane, the matching over 1.8-5 GHz is degraded. To improve the impedance bandwidth, the semi-ring is loaded with a 0.1pF capacitor and a slit of $0.5 \times 5mm^2$ which improve the matching at 3-6 GHz and 6-9 GHz, respectively, as shown in Fig. 6.3.

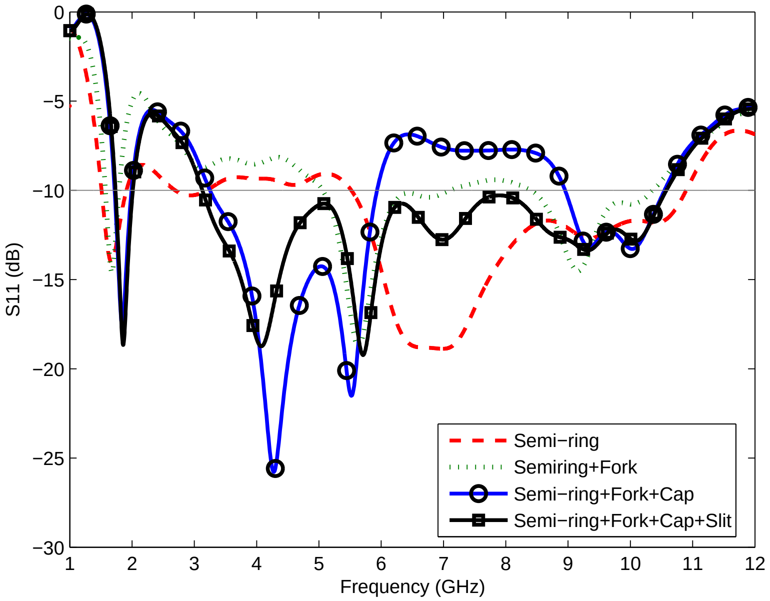

Figure 6.2: Effect of different elements on input reflection coefficient.

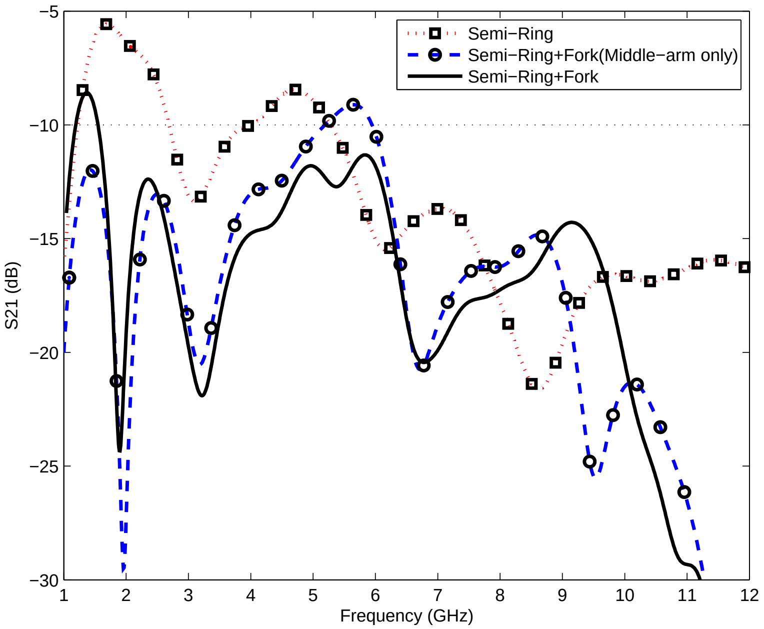

Figure 6.3: Effect of fork structure on port isolation.

The performance of the fork shaped structure on isolation enhancement can also be observed by looking at the ground plane current distribution by exciting one port while terminating other by 50 Ω. The current distribution with and without the fork structure at 1.85GHz and 5.2GHz are shown in Fig. 6.4 when port1 is excited and port2 is terminated with 50 Ω. It can be seen that the current between the two radiators is greatly reduced by the fork at both frequencies and consequently reduces mutual coupling.

6.1.2 Results and Discussions

To validate the simulation results, a fabricated prototype as shown in Fig. 6.5 is tested. The S-parameters of the antenna are measured using Agilent N9918A VNA

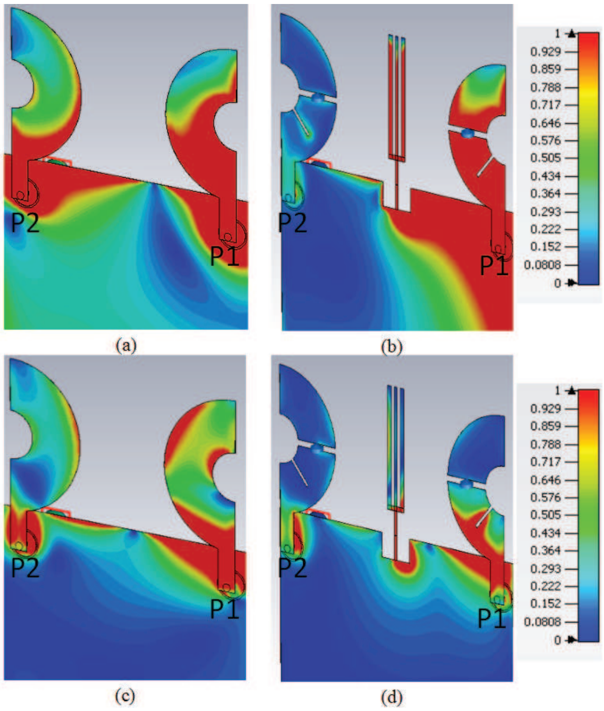

Figure 6.4: Current distribution with and without fork at 1.85GHz [(a) and (b)] and at 5.2GHz [(c) and (d)].

and shown in Fig. 6.6 compared to the simulated results. It can be seen that the measured antenna shows better impedance matching compared to the simulation from 2-3 GHz and shows -10 dB bandwidth covering 1.85-10.6 GHz. The isolation is also more than 10 dB over the entire frequency range. A two-element semi-ring antenna without the fork shaped structure is also measured and shown in Fig. 6.6. It can be seen that the fork significantly improves the isolation over the whole operating frequency range. The measured results show well agreement to the simulations and slight degradation in the simulated reflection coefficient at the lower bands can be attributed to the fixed component values and not taking effect of the connectors and fabrication process (soldering) in the model that might have improved the matching in the 2-3 GHz band.

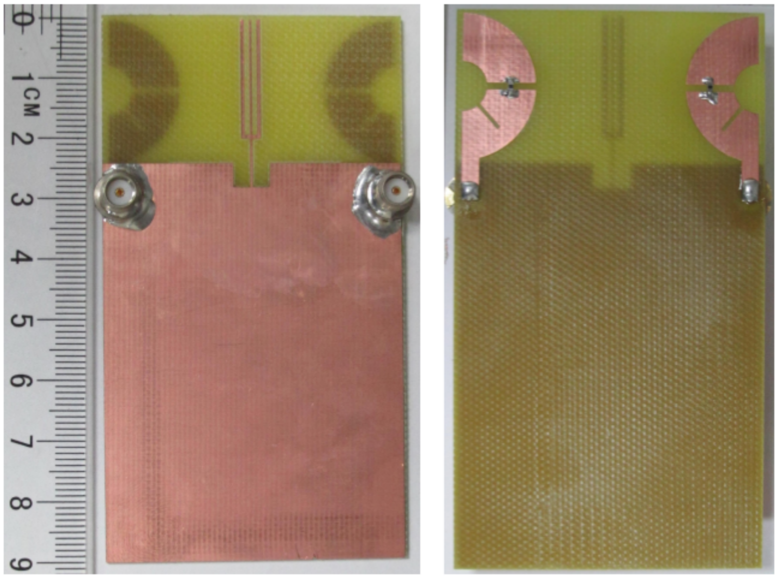

(a) (b)

Figure 6.5: Fabricated prototype: (a) bottom and (b) top layer.

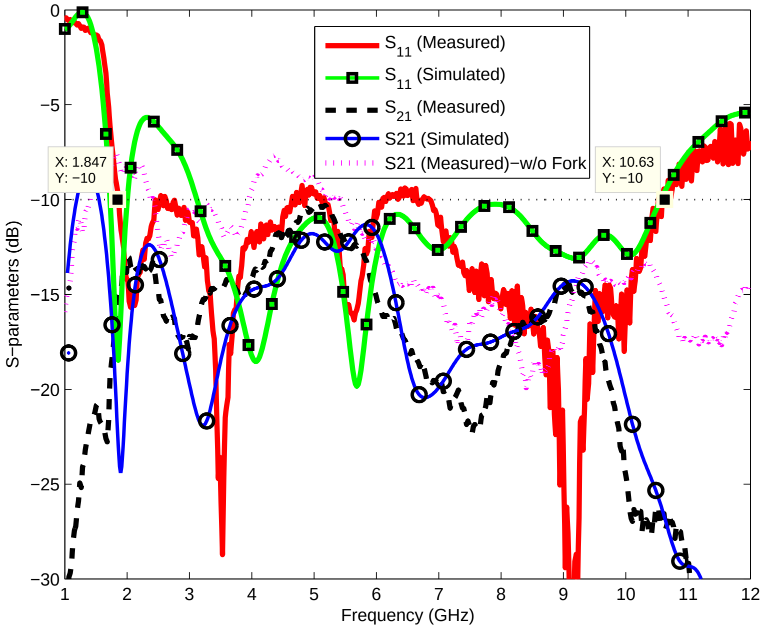

Figure 6.6: Measured and simulated S-parameters.

To evaluate the radiation characteristics of the antenna, it was measured in a Satimo STARLAB anechoic chamber. The measured and simulated results for the gains and efficiencies of the antenna are shown in Fig. 6.7. The minimum measured gain and efficiency of the antenna are found to be 1.9 dBi at 1.85 GHz and 51.8% at 2 GHz, respectively. The measured results shows similar trends to the simulations where the mismatch might be attributed to the component non-idealities, cable loss and misalignment of the antenna during far-field measurement which have not been considered in simulations. The simulated gain and efficiency of the antenna at 10.6 GHz are found to be 5.33 dBi and 76%, respectively. The normalized measured radiation patterns in terms of E_θ and E_ϕ at 1.85, 2.4 and 5.8 GHz are illustrated in Fig. 6.8 for the major planes $\phi = 0^{\circ}$ and $\theta = 90^{\circ}$. It can be observed that the measured patterns are tilted in the $\phi = 0^{\circ}$ and $\theta = 90^{\circ}$ planes which will result in low correlation between the MIMO channels.

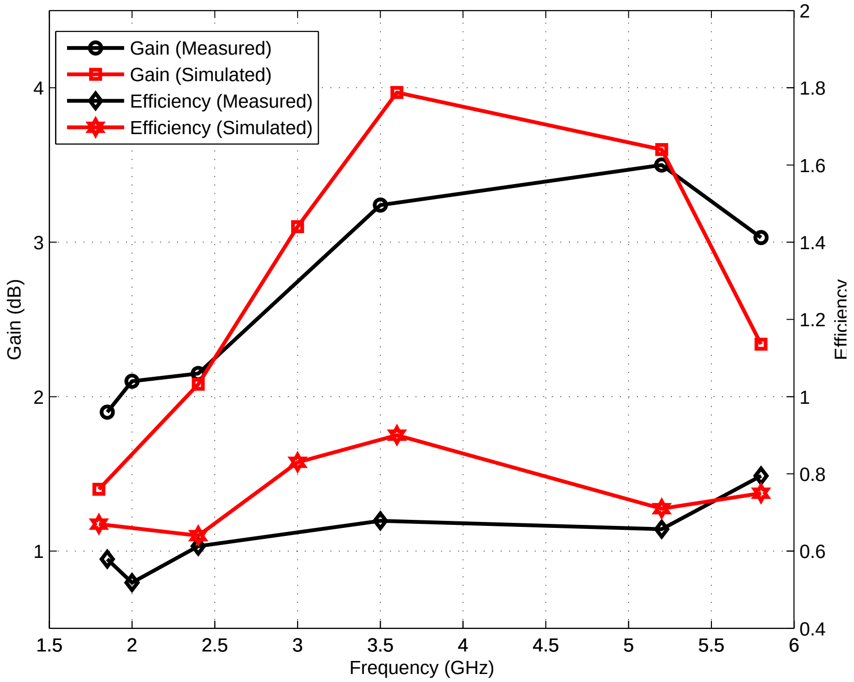

Figure 6.7: Measured and simulated gain and efficiency of the antenna.

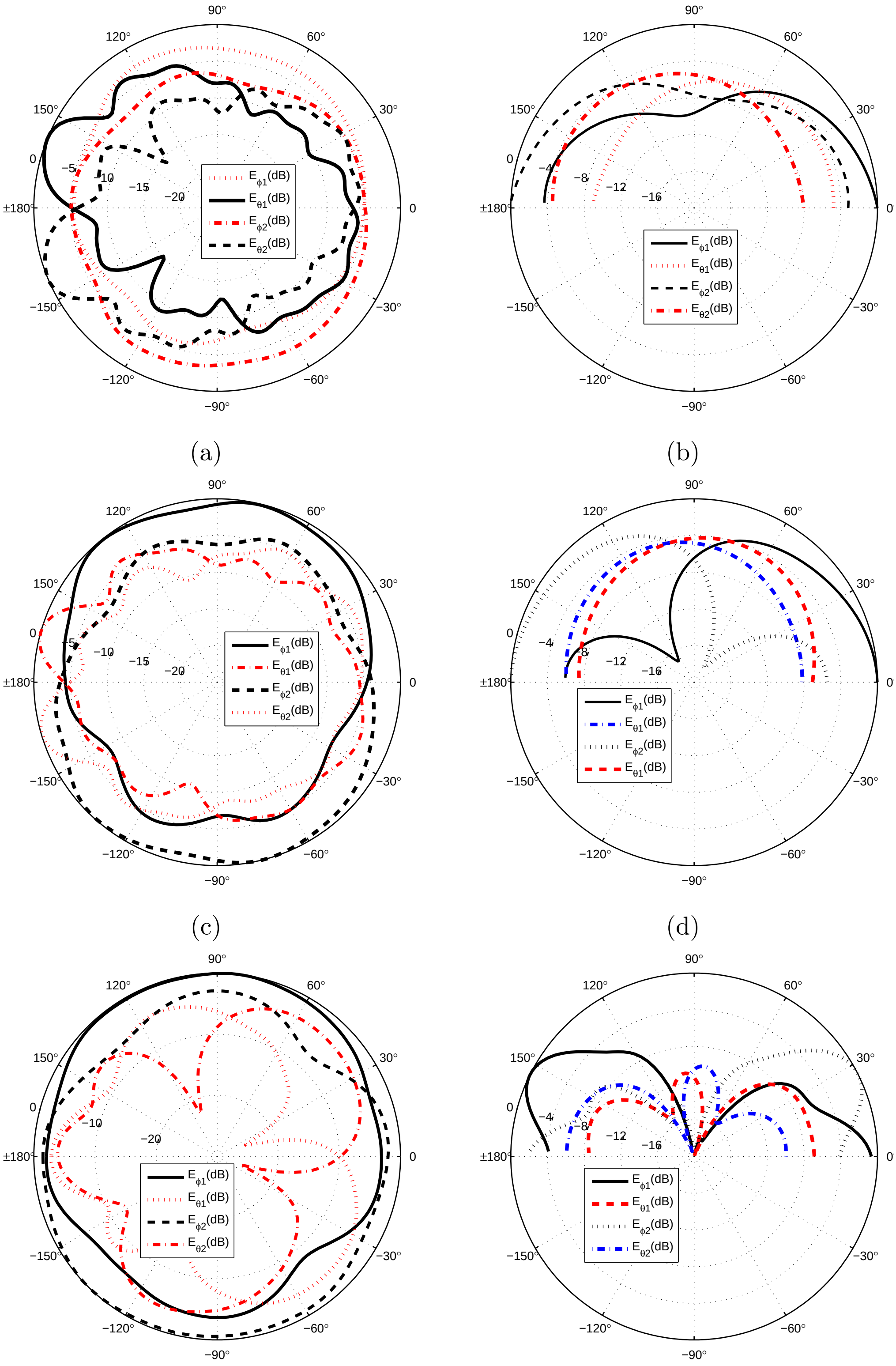

(a) (b) (c) (d) (e) (f)

Figure 6.8: Normalized radiation patterns E_θ and E_ϕ: at 1.85 GHz- (a) $\phi = 0^\circ$ and (b) $\theta = 90^\circ$; at 2.4 GHz- (c) $\phi = 0^\circ$ and (d) $\theta = 90^\circ$; and at 5.8 GHz- (e) $\phi = 0^\circ$ and (f) $\theta = 90^\circ$.

Table 6.1: Measured and Simulated ECC and DG from 3D radiation patterns.

Frequency (GHz)	ECC (Measured)	ECC (Simulated)	Measured DG (dB)	Simulated DG (dB)
1.85	0.1619	0.1450	9.1546	9.2466
2.00	0.0927	0.0481	9.5254	9.7565
2.40	0.1538	0.0475	9.1991	9.7596
3.50	0.1449	0.0115	9.2473	9.9423
5.20	0.0104	0.0229	9.9477	9.8848
5.80	0.0208	0.0018	9.8956	9.9910

To evaluate the diversity performance of the designed MIMO antenna, ECC and DG are evaluated from the simulated and measured radiation fields. ECC is calculated according to the expression described in Section 2.2.3 and listed in Table 6.1. It can be seen that the measured ECC shows similar results to the simulations and maximum ECC is found to be 0.1619 at 1.85 GHz which is below the acceptable ECC value of 0.5 with a significant margin. Similarly, DG of the antenna is calculated from radiation patterns of the antennas as described in chapter 2 and listed in Table 6.1. It can be seen that the measured results are in well agreement to the simulations and shows the DG to be more than 9 dB.

A summary of the proposed antenna parameters comparing to recent works from the literature is presented in Table 6.2. It should be noted that the reference works in the figure of table calculated ECC values from S-parameters and this is not completely correct for lossy antennas, and thus it should be evaluated based on the radiated fields instead as done in this work. However, it can be seen that the antenna presented in this work shows the highest fractional bandwidth covering the entire range 1.85-10.6GHz with $S_{11} \leq -10dB$ having comparable radiator size, gain and ECC. Considering these results, the proposed UWB MIMO antenna can be a good candidate for UWB systems with integrated communication networks.

In summary, an ultra-wideband (UWB) two-element multiple-input-multiple-output (MIMO) antenna is designed. The antenna is designed on a low cost FR4 substrate having an overall size of $50 \times 90 \times 1.52mm^3$. The measured -10 dB impedance bandwidth covers 1.85 to 10.6 GHz. The size of each radiator is $12 \times 24mm^2$ which is $0.011\lambda_0^2$ where λ_0 is the free space wavelength at 1.85 GHz. The minimum measured gain and efficiency are found to be 1.22 dBi and 51.8%, respectively. The isolation of the antenna is enhanced using a fork shaped structure. The measured isolation is more than 10 dB over the entire operating band. The measured ECC is less than 0.16 while a diversity gain (DG) of approximately 9.5dB is achieved. The antenna shows lucrative figures of merits which makes it a good candidate for handheld mobile device application.

6.2 UWB Integrated MIMO Antenna Design

In the previous chapter, antenna miniaturization through active device (amplifier) integration was discussed. A patch antenna was miniaturized and 51% of size reduction was achieved for a narrowband and a broadband patch antenna. In this section, features of active integration in a MIMO system is intended to present targeting enhanced port isolation, improved impedance matching and UWB RF front-end integration covering the region of 1.8-6 GHz. A transmitting two-element MIMO antenna is designed to prove the idea of AIA MIMO

Table 6.2: Comparison of antenna parameers to the recent wideband/UWB MIMO antenna systems.

Parameters	[106]	[107]	[108]	[109]	[110]	[111]	[112]	This Work
Size (mm^2)	0.011 λ_0^2	0.007 λ_0^2	0.012 λ_0^2	0.0132 λ_0^2	0.0076 λ_0^2	0.029 λ_0^2	0.009 λ_0^2	0.011 λ_0^2
Substrate (mm^3)	100× 60×0.8	100× 50×1.6	90×40 × 0.8	40×30 ×0.8	30 × 27 ×0.8	56×28 ×1	86×55 ×0.8	90×50 ×1.5
Spacing	0.08 λ_0	0.18 λ_0	0.19 λ_0	0.52 λ_0	0.17 λ_0	0.1 λ_0	0.145 λ_0	0.15λ_0
Frequency Band (GHz)	1.66-2.84	1.8-3.77	2.4-4.2	3.1-3.4, 4-5, 6-11	3.1-3.3, 3.7-5.1, 5.8-11	2.4-2.49 3.1-10.6	1.9-5.1	1.85-10.6
Min. Isolation (dB)	15	13	17	15	20	15	17.2	10
Fractional Bandwidth (%)	52.44	71.22	54.5	9.23, 22.2 58.8	6.2,31.8, 61.9	3.7, 109.5	91.37, 57.75	140.56
Min. Eff.	0.81	—	—	-.53	0.65	0.85	0.91	0.52
Min. Gain (dBi)	—	2.86	1	2.2	—	-2	4.25	1.9
Max. ECC	0.05	0.16	0.005	0.05	0.002	0.01	0.18	0.15

and to examine its features mentioned above. The similar design procedure is followed that is described in the Section 5.1 except the final optimization is now run for a two-element UWB antenna system. In the following sections, detailed amplifier and antenna characterization, integrated antenna design and its results are discussed.

6.2.1 Amplifier Characterization

In this design, a commercially available UWB prematched RF amplifier is used from Mini-Circuits (GVA 63+). Its S-parameters were measured by the test circuit shown in Fig. 6.9a. The fabricated prototype of the board is shown in Fig. 6.9b where RO4350B substrate is used having dielectric constant, loss tangent and height of 3.5, 0.004 and 0.762 mm, respectively. The width of the transmission lines were 1.7 mm with the lengths of $TL_2 = TL_3 = 3mm$ and $TL_1 = TL_4 = 5mm$. The lumped element values were $C_1 = C_2 = 1nF,\ C_3 = 0.1\mu F$ and $V_{DC} = 5V$.

The amplifier s-parameters are measured and the connectors effect is de-embedded. The measured two port reflection co-efficients of the amplifier after de-embedding are shown in Fig. 6.10. Afterwards, gain and stability parameters (Δ and k) are calculated and shown in Fig. 6.11. It can be seen that over the frequency band 1 GHz to 6 GHz, the amplifier is unconditionally stable since $|\Delta| < 1$ and $k > 1$. The minimum noise figure of the amplifier is found to be 3.5-4 dB over the range of 1-6 GHz.

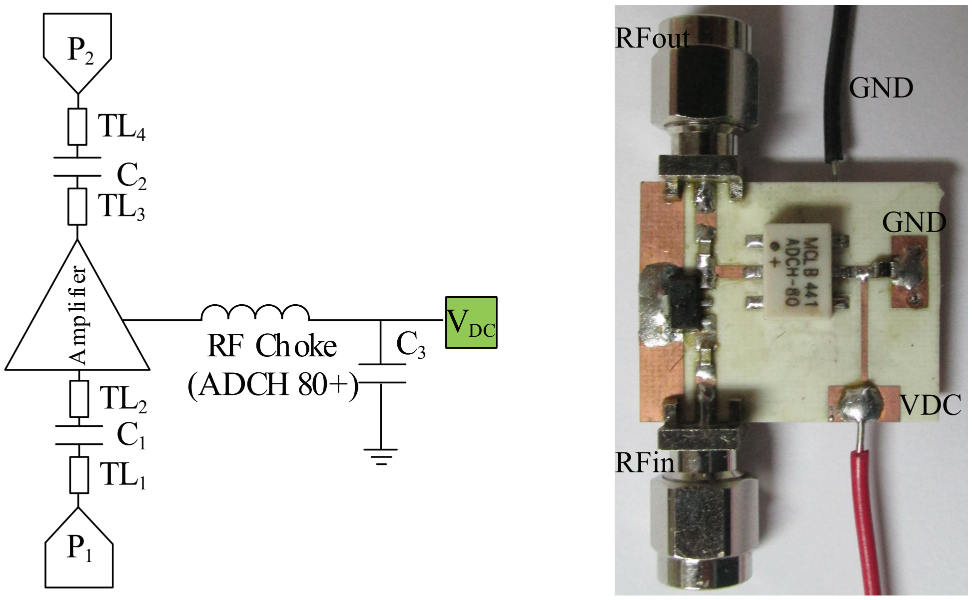

(a) (b)

Figure 6.9: Amplifier test board: (a) schematic and (b) fabricated prototype.

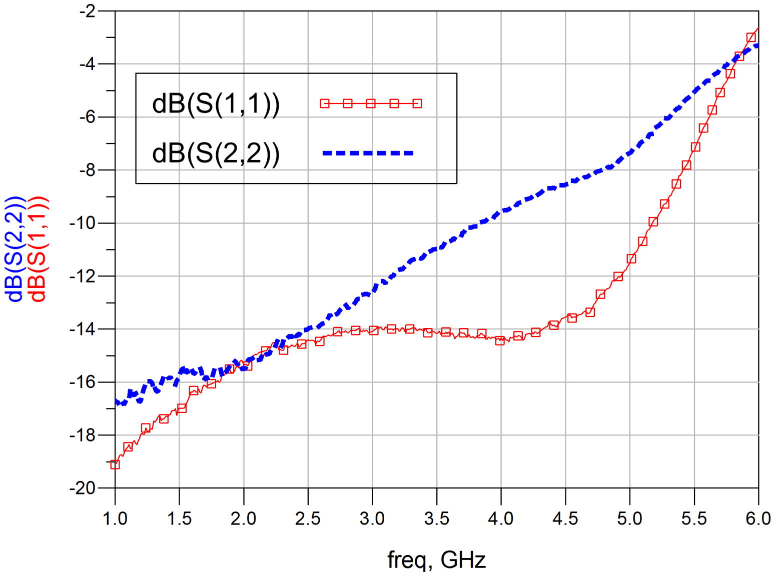

Figure 6.10: Measured port reflection coefficients of the UWB amplifier.

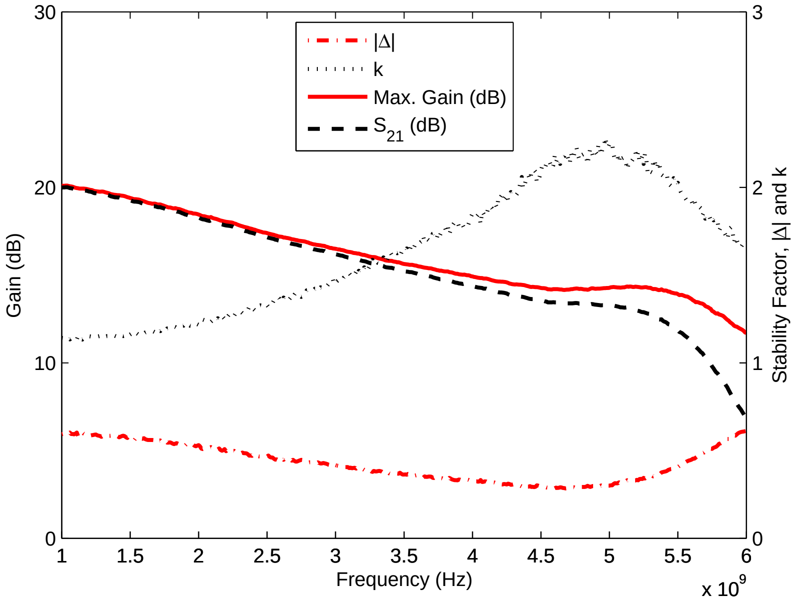

Figure 6.11: Measured port reflection coefficients of the UWB amplifier.

6.2.2 UWB Antenna Characterization

The amplifier was characterized using a RO4350B substrate because of its better response at high frequencies compared to low cost FR4 substrate. That's why to test integrated UWB MIMO antenna behavior on same substrate, the UWB antenna persented in the Section 6.1 is characterized again with the same substrate (i.e. RO4350B). Again, to examine the port isolation enhancement, the UWB semi-ring antenna without the fork shape in the ground plane is chosen. The semi-ring antenna is modeled and simulated in CST Microwave Studio as shown in Fig. 6.12.

The fabricated prototype is shown in Fig. 6.13. To characterize the antenna, the s-parameters of the antenna are measured using an Agilent N9918A VNA. The measured and simulated s-paremeters of the antenna are shown in Fig. 6.14.

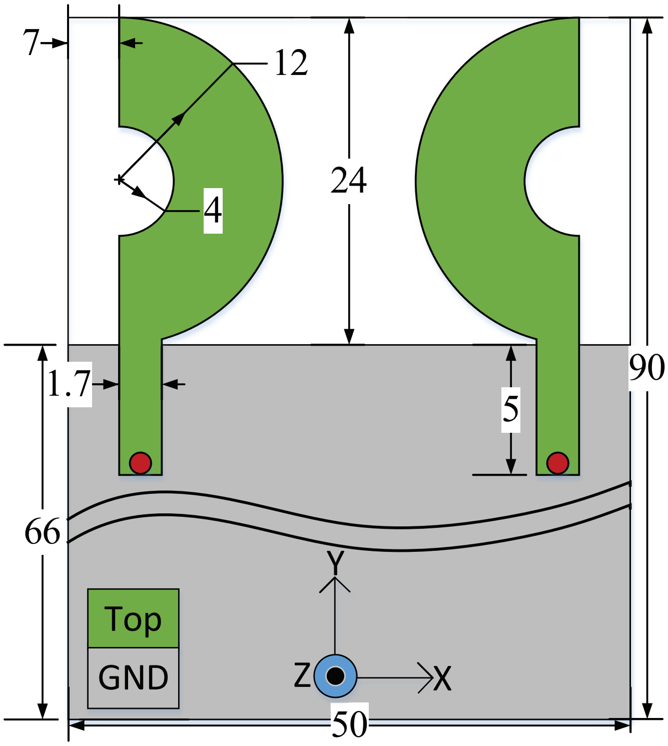

Figure 6.12: UWB semi-ring MIMO antenna model.

It can be seen that the measured results are in well agreement to the simulations. The slight deviation might be attributed to the difference in material modeling during simulation. Anyway, to avoid carrying errors in afterward steps, measured results are used for further design steps. It can be seen that the fabricated antenna (as well as the simulated one) does not match (-10dB) over the whole band 1.8-5.8 GHz and the isolation is also less than the minimum standard 10 dB. Thus, improvement in matching and port isolation enhancement is left for the integrated antenna design approach to take care of and this way, tedious optimization process of antenna structure is avoided.

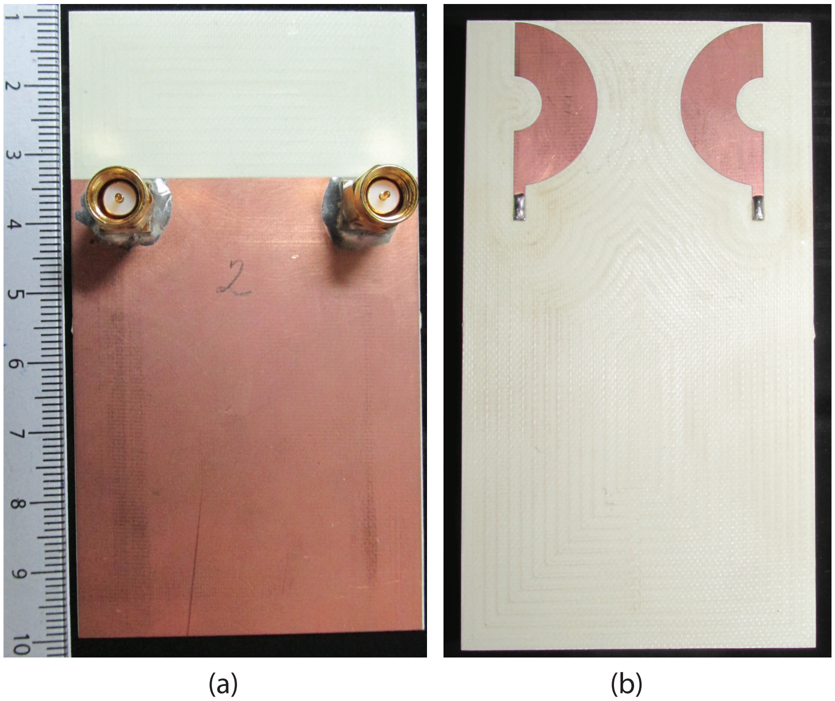

Figure 6.13: UWB semi-ring MIMO antenna fabricated prototype: (a) bottom view and (b) top view.

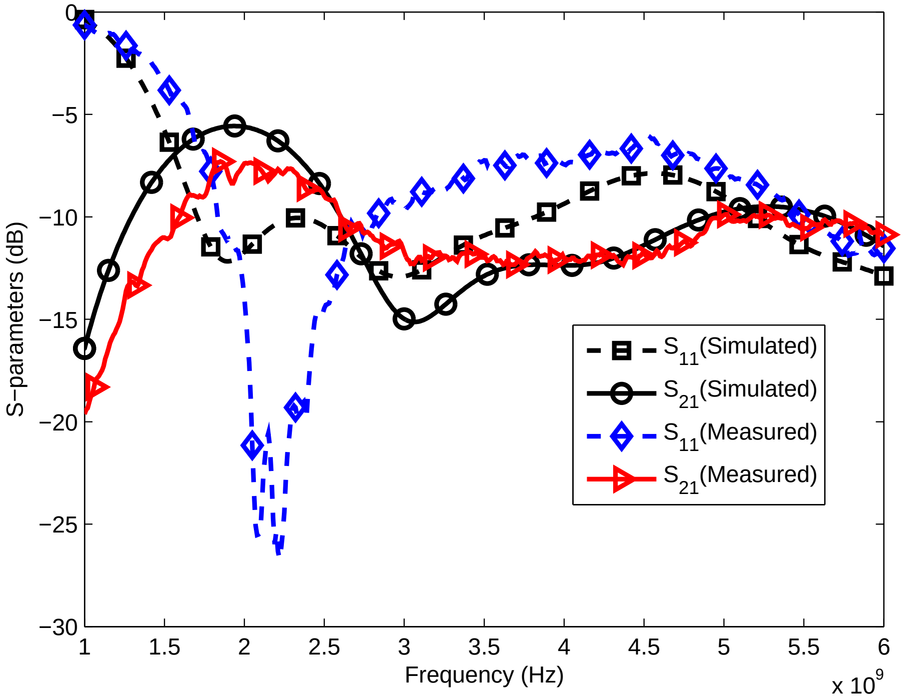

Figure 6.14: UWB antenna s-parameters.

6.2.3 Integrated UWB MIMO Antenna

In the previous chapter, co-designing of antennas and RF amplifiers was presented by which antenna miniaturization was achieved through conjugate matching. Traditionally, antennas and RF front-end electronic systems are designed separately based on 50 Ω port impedance. Generally, -10 dB (or minimum -6dB) matching of input and output ports for any RF subsystems is taken as the standard. But, it is observed that when two such 50 Ω based subsystems (individually matched) are cascaded directly, integrated system performance is degraded due to the mismatch at the interface. This is because of the reason that when two subsystems are cascaded together, they actually no more interface through 50 Ω and see each others real impedance which may not give -10 dB matching anymore over the band of interest met by individual subsystems. The situation will be worst when -6 dB matching of individual subsystem is adopted. And for a UWB system, the mismatch effect comes with greater impact- the integrated system may not show UWB matching at all. For example, the measured results of the UWB antenna and the UWB amplifier are directly cascaded as shown in Fig. 6.15 and the integrated antenna reflection coefficient is calculated according to (6.1) and shown in Fig. 6.16. It can be seen that the antenna matching is significantly degraded after direct integration in the range of 2.3-4 GHz. Thus, it is obvious that co-designing RF subsystems is important for an optimized integrated system performance. In this work, improvement of MIMO antenna performance is examined in terms of matching and port isolation which in other words will provide better realized gain and total radiation efficiency of the antenna.

$$\Gamma_{ant}(int) = \frac{Z_{ant} - Z^*_{out}}{Z_{ant} + Z_{out}} \tag{6.1}$$

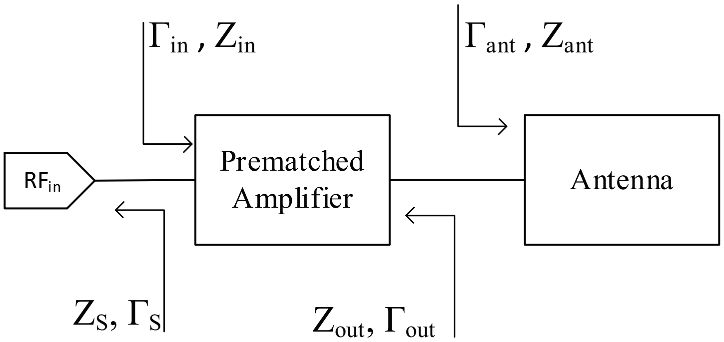

Figure 6.15: Block diagram of direct integration- amplifier and antenna.

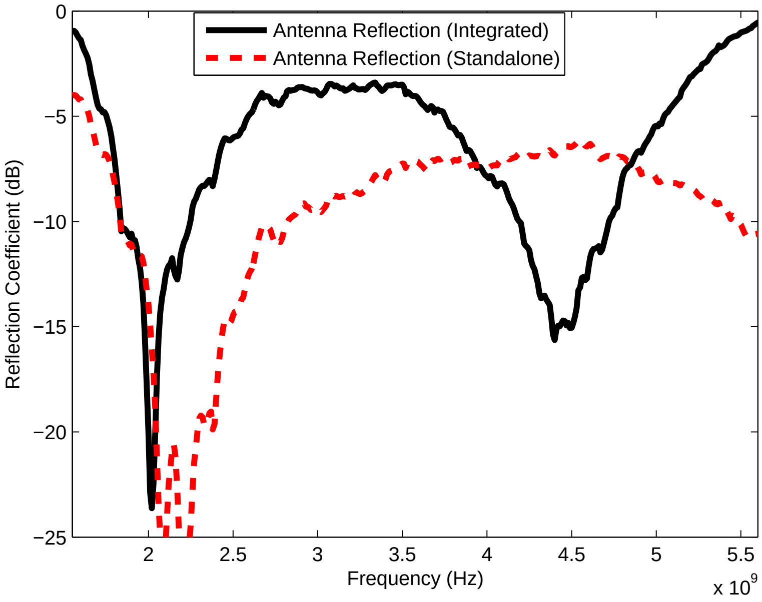

Figure 6.16: Antenna reflection before and after cascading with RF amplifier (Direct Integration).

The block diagram of a two-element RF amplifier integrated transmitting

MIMO antenna adopted in this work is shown in Fig. 6.17. Similar design procedure is adopted as in patch antenna based transmitting AIA design presented in Chapter 5 except two changes which are considered for UWB and MIMO antenna:

1. Design process starts by selecting Γ_S for optimum gain and noise performance as described in patch AIA design. However, for a UWB design approach, Γ_S selected for a single frequency cannot guarantee the same gain and noise figure over the desired UWB range. To tackle this issue, a set of gain and noise circles are plotted for a specific gain and noise figure over the entire range of interest. Thus, Γ_S is selected for optimum gain and noise figure looking over the desired band and a locus of Γ_{out} is calculated. This simulation approach is shown in Fig. 6.18.

2. Matching network design optimization for optimum antenna matching and port isolation is carried out in a MIMO integrated arrangement as shown in Fig. 6.17 instead of single antenna element as it was performed in the patch AIA design.

Thus, input and output matching network are designed through the optimization toolbox of ADS for optimum integrated antenna matching, system gain and port isolation. The finalized circuit diagram is shown in Fig. 6.19 having the lumped component values of $C_1 = C_4 = 0.1pF$, $C_2 = 0.4pF$, $C_3 = 0.7pF$, $L_1 = 1nH$, $L_2 = 0.5nH$ and trnsmission line length of $TL_1 = 10mm$ and $TL_2 = TL_3 = TL_4 = TL_5 = 3mm$ having the width of 1.7mm. The improvement in port isolation is achieved by the loop gain from port 1 to port 2. The antenna

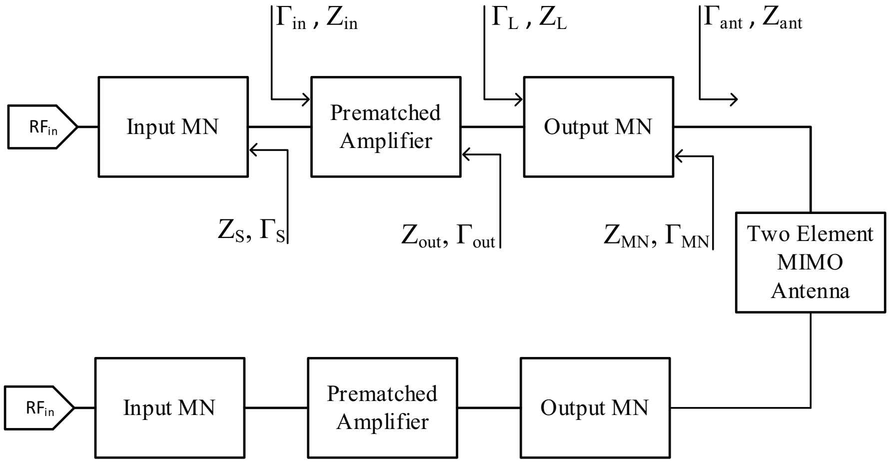

Figure 6.17: Integrated two-element MIMO antenna system block diagram.

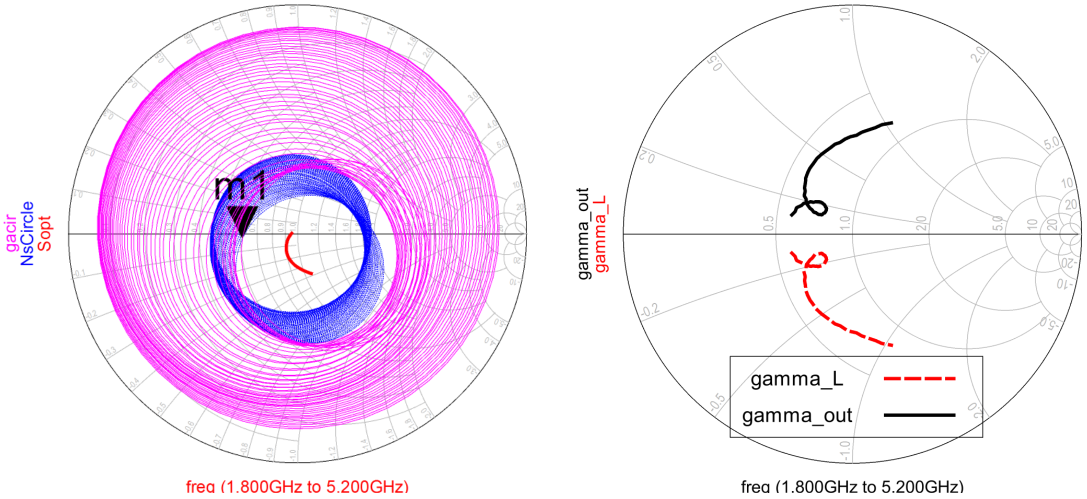

Figure 6.18: UWB active integrated MIMO antenna design: selecting Γ_S and finding Γ_{out}.

reflection coefficient after integration is calculated and shown in Fig. 6.20 compared to the standalone antenna. It can be seen that the antenna matching is improved over the band 1.75-5.5 GHz. This will improve the realized gain and total radiation efficiency of the antenna and thus total system performance.

The simulated s-parameters of the MIMO antenna system are shown in Fig. 6.21. It can be seen that the port isolation is improved and found to be

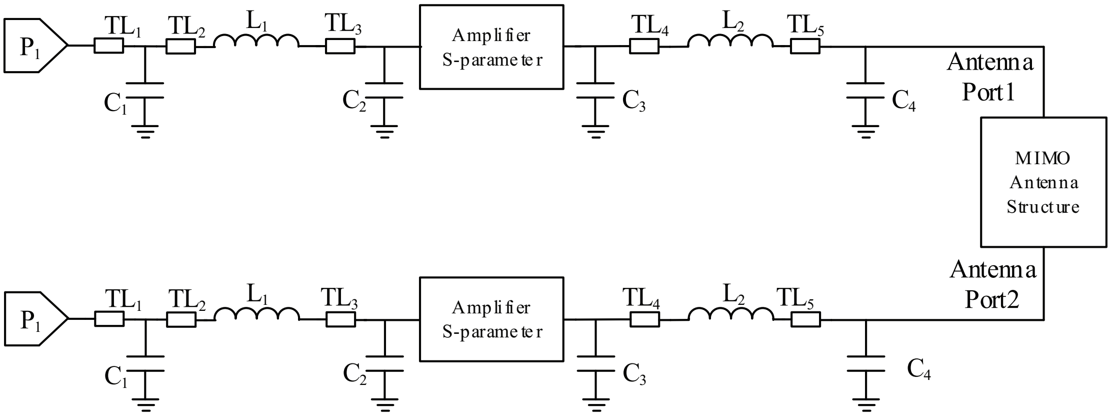

Figure 6.19: Active integrated two-element MIMO antenna schematic.

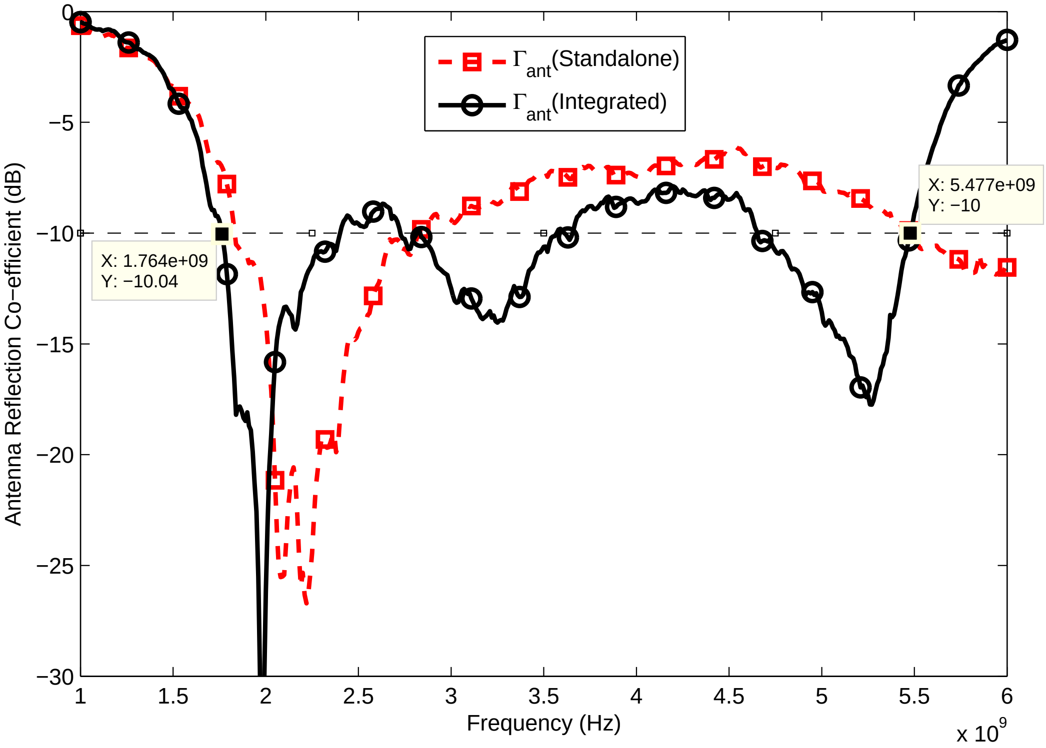

Figure 6.20: Simulated antenna reflection co-efficient: before and after integration.

more than 12 dB over the entire band which is around 7 dB of isolation improvement. The system also shows good input port matching (low input VSWR) as well which will also improve overall system efficiency. The circuit is simulated in CST Design Studio to see the integrated amplifier gain and found to be more than

12dB over the band 1.8-5.5 GHz.

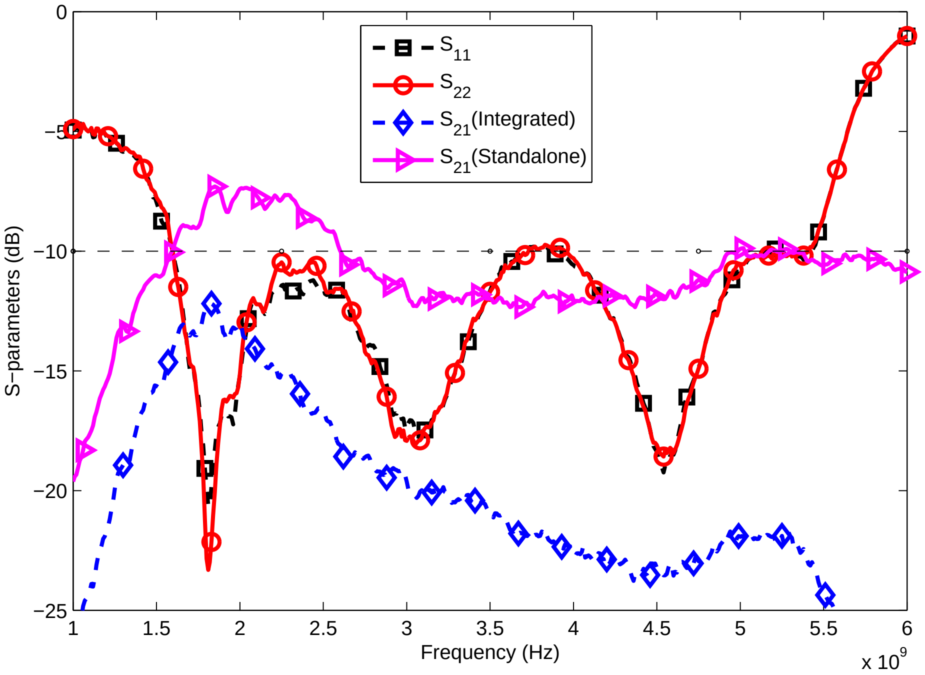

Figure 6.21: Simulated s-parameters of the active integrated MIMO antenna system.

To see the radiation characteristics of the optimized MIMO active integrated system, a co-simulation is performed in CST as described in Chapter 5. The simulated 3-d gain patterns of the integrated system are shown in Fig. 6.22. The gain plots are self explaining having the frequency points, realized gain and total radiation efficiency listed (in the left side legends) both for the cases before and after integration. The values after integration are shown as "System [AC1]. It can be seen that the integrated antenna shows excellent realized gain over the frequency band (more than 12dB) which indicates good matching at the antenna port.

The finalized active integrated transmitting MIMO antenna system is fabri-

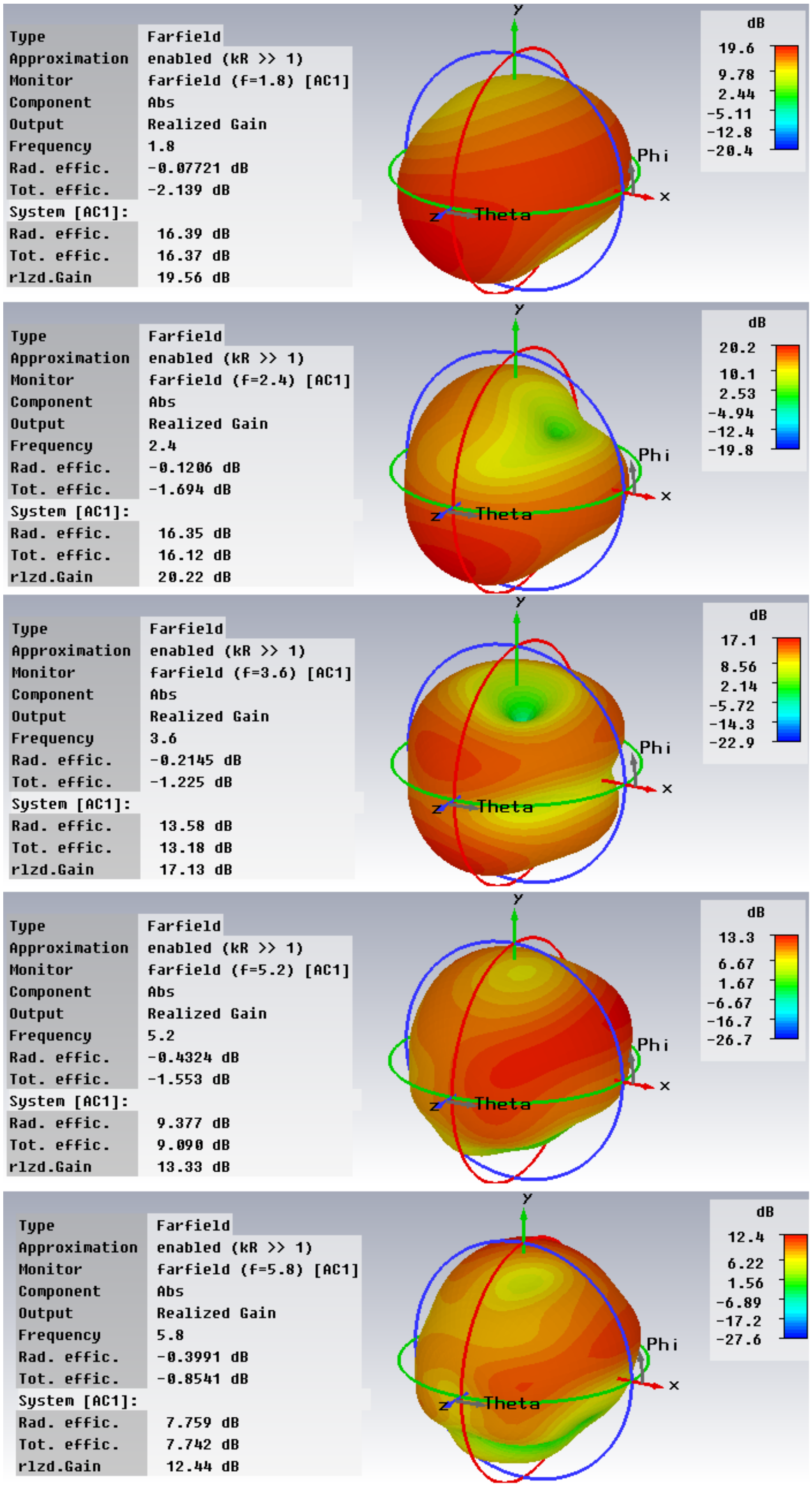

Type	Farfield
Approximation	enabled (kR >> 1)
Monitor	farfield (f=1.8) [AC1]
Component	Abs
Output	Realized Gain
Frequency	1.8
Rad. effic.	-0.07721 dB
Tot. effic.	-2.139 dB
System [AC1]:	
Rad. effic.	16.39 dB
Tot. effic.	16.37 dB
rlzd.Gain	19.56 dB

Type	Farfield
Approximation	enabled (kR >> 1)
Monitor	farfield (f=2.4) [AC1]
Component	Abs
Output	Realized Gain
Frequency	2.4
Rad. effic.	-0.1206 dB
Tot. effic.	-1.694 dB
System [AC1]:	
Rad. effic.	16.35 dB
Tot. effic.	16.12 dB
rlzd.Gain	20.22 dB

Type	Farfield
Approximation	enabled (kR >> 1)
Monitor	farfield (f=3.6) [AC1]
Component	Abs
Output	Realized Gain
Frequency	3.6
Rad. effic.	-0.2145 dB
Tot. effic.	-1.225 dB
System [AC1]:	
Rad. effic.	13.58 dB
Tot. effic.	13.18 dB
rlzd.Gain	17.13 dB

Type	Farfield
Approximation	enabled (kR >> 1)
Monitor	farfield (f=5.2) [AC1]
Component	Abs
Output	Realized Gain
Frequency	5.2
Rad. effic.	-0.4324 dB
Tot. effic.	-1.553 dB
System [AC1]:	
Rad. effic.	9.377 dB
Tot. effic.	9.090 dB
rlzd.Gain	13.33 dB

Type	Farfield
Approximation	enabled (kR >> 1)
Monitor	farfield (f=5.8) [AC1]
Component	Abs
Output	Realized Gain
Frequency	5.8
Rad. effic.	-0.3991 dB
Tot. effic.	-0.8541 dB
System [AC1]:	
Rad. effic.	7.759 dB
Tot. effic.	7.742 dB
rlzd.Gain	12.44 dB

Figure 6.22: Simulated 3-d radiation patterns of the integrated MIMO antenna system.

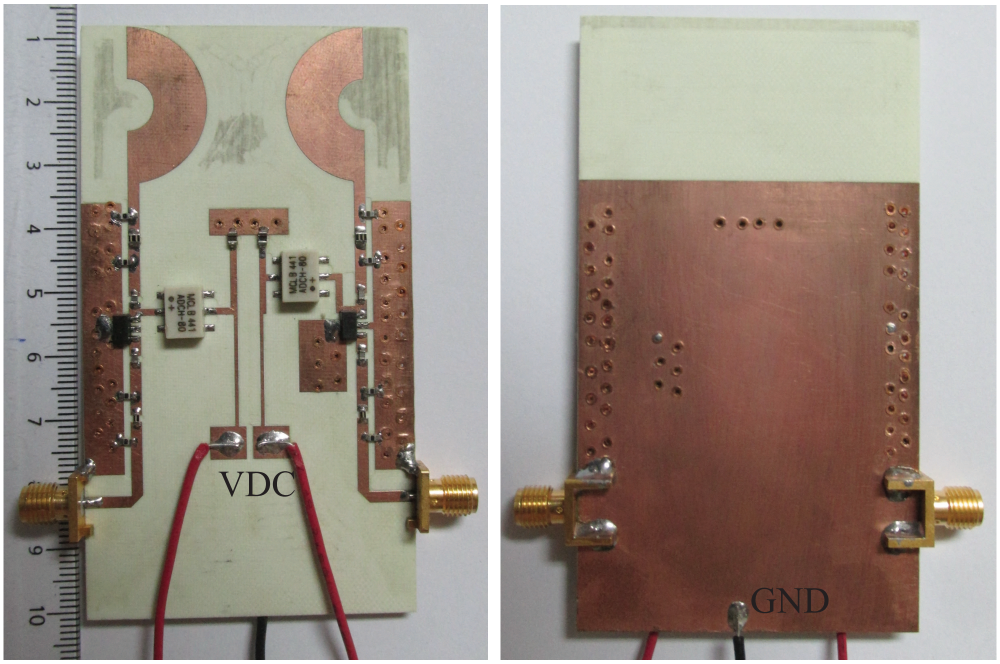

(a) (b)

Figure 6.23: Fabricaetd Prototype of the active integrated MIMO Antenna system: (a)top view and (b) bottom view.

cated and populated with the lumped components. The implemented prototype is shown in Fig. 6.23. The measured input reflection co-efficients are shown in Fig. 6.24. It can be seen that the measured results are almost following the simulation one up to 4 GHz. The deviation after 4 GHz is due to the non-idealities of lumped components and hand soldering. Although two-element MIMO are built with same components, deviation is observed which might be attributed to the hand soldering. The measured port isolation is shown in Fig. 6.25 comparing to the simulated one. It can be seen that the measured isolation is also greater that 10 dB over the operating band 1.8-5.5 GHz.

To check the radiation characteristics of the fabricated prototype, it has measured in Satimo StarLab anechoic chamber. The maximum realized gain of the

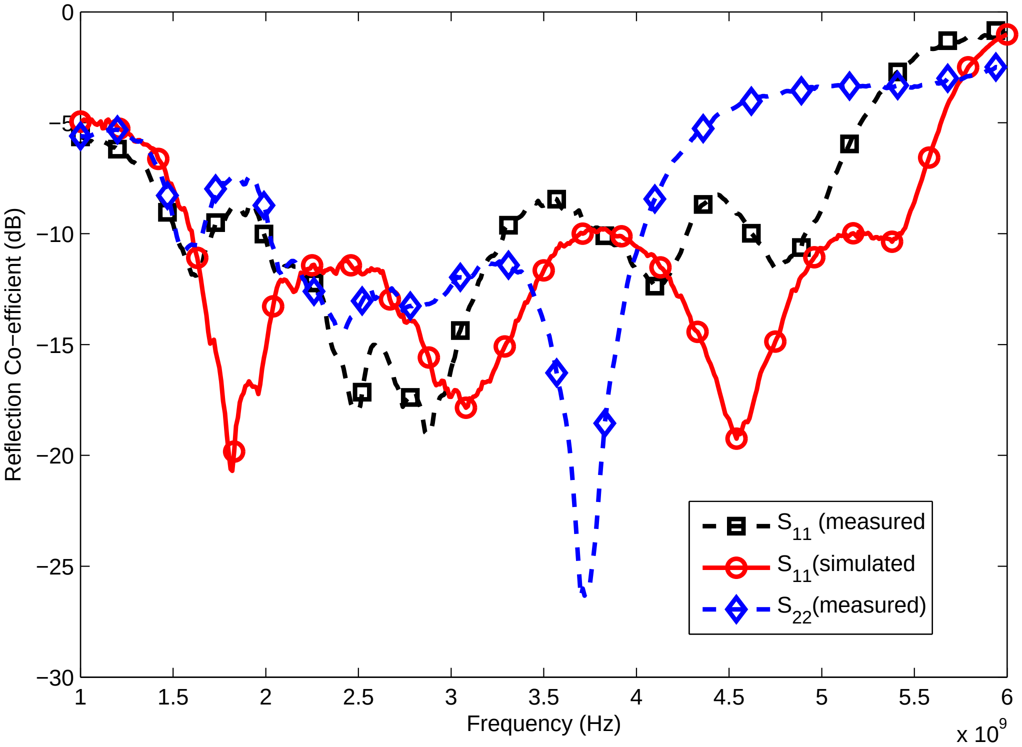

Figure 6.24: UWB active MIMO antenna reflection coefficient.

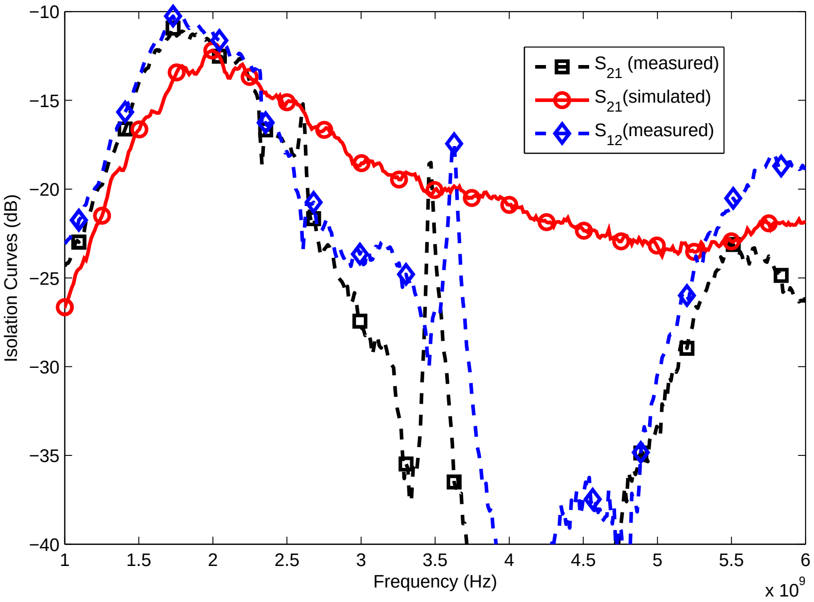

Figure 6.25: UWB active MIMO antenna measured port isolation.

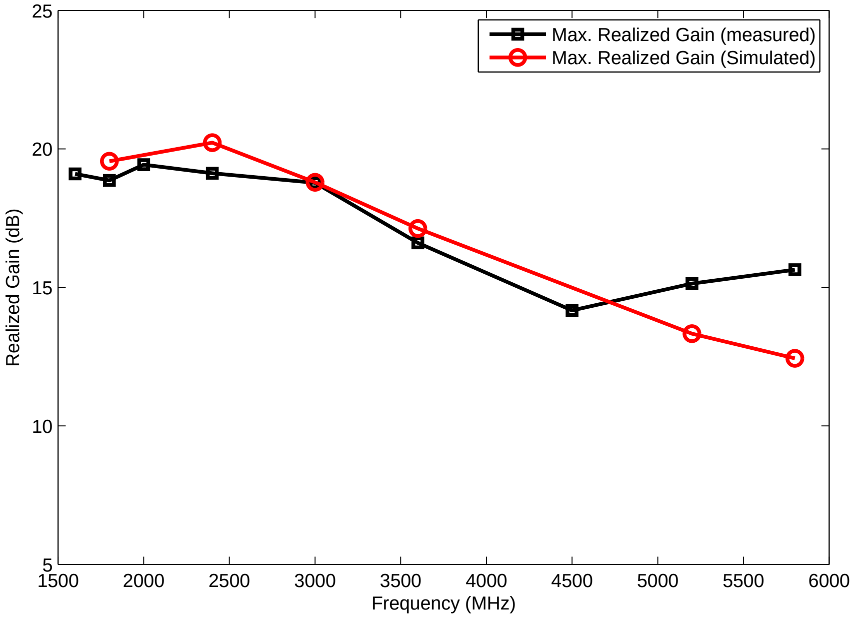

Figure 6.26: Realized gain of the active integrated MIMO antenna system.

active integrated MIMO antenna system is shown in Fig. 6.26 compared to its simulated counterpart. It can be seen that the gain of the fabricated prototype is in well agreement to the simulation result. Efficiency of the antenna after integration is estimated from input power to the integrated system, amplifier gain and radiated power. It can be shown that the integrated MIMO antenna shows efficiency greater that 60% as shown in Fig. 6.27.

To evaluate the diversity performance of the integrated MIMO antenna system, ECC from both simulated and measured radiation patterns are calculated and shown in Fig. 6.28. The ECC values are found to be less than the acceptable maximum value of 0.5. It can be seen that the simulated ECC of the integrated MIMO antenna is lower than the simulated ECC of the standalone MIMO antenna. This might be attributed to the isolation improvement by the active integration.

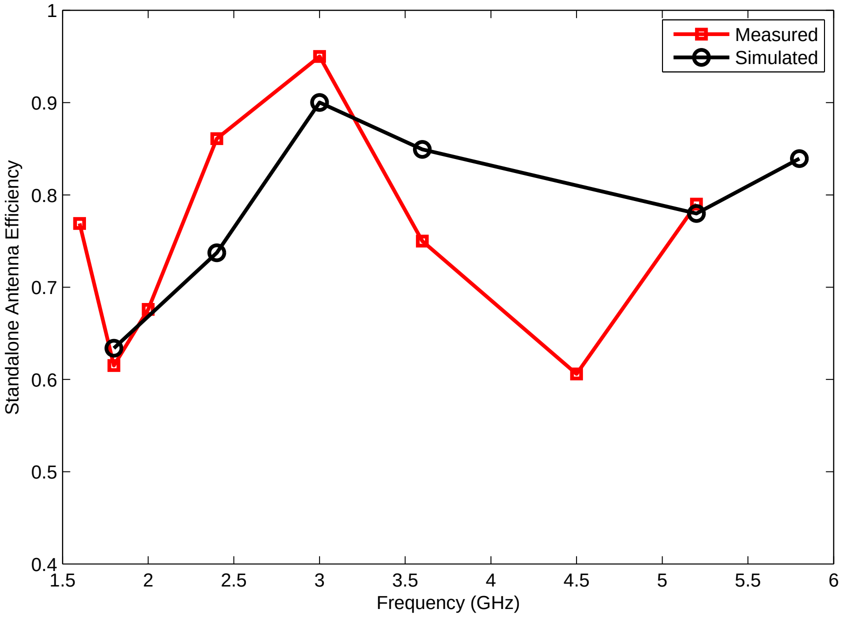

Figure 6.27: Total radiation efficiency of the integrated antenna.

However, the ECC values from the measured integrated antenna system is found to be higher than the simulated ECC. Care should be taken during measurement considering orientation mismatch which is not the case in simulation. However, still the maximum measured ECC value of the integrated MIMO antenna is 0.33 which is below the acceptable standard of 0.5 with a significant margin.

6.3 Conclusions

In this chapter, an active integrated transmitting MIMO antenna is presented. The integrated system is designed to operate in the range of 1.8-5.8 GHz. Through such integration and co-designing, better antenna input reflection coefficient and port isolation improvement is observed and verified through experimental results.

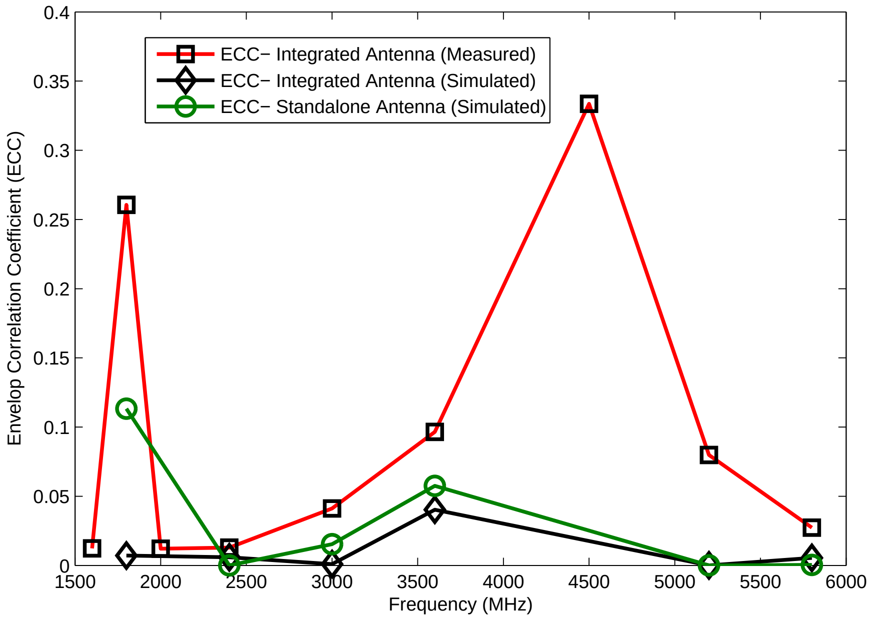

Figure 6.28: Measured and simulated ECC of the UWB MIMO antenna system.

Through such co-design approach, improved antenna matching and isolation are achieved without tedious electromagnetic parametric study. Detailed design procedure is presented with simulation and measurement results. Thus, a new technique of isolation enhancement and antenna matching is presented through the integration of antenna and RF amplifier which is not appeared before in the literature.

CHAPTER 7

CONCLUSIONS AND FUTURE WORK

7.1 Conclusions

In this work, active antennas and their different features are investigated. Active antennas are of significant interest because of their advantages over passive antennas. In this work, a co-design approach of antennas and RF front-ends is adopted for active integrated antenna realization and different features especially miniaturization and port isolation improvement are examined. Apart from this, a feasibility analysis on a technique of wideband matching network design called SRFT for the bandwidth enhancement of narrowband antenna structure is investigated. It is found that the SRFT although can design wideband matching network but cannot improve the bandwidth of a narrow band structure.

The miniaturization of patch antennas are presented through co-design of RF amplifiers. To do so, conjugate matching of patch antennas with the amplifiers at the desired frequency bands is performed and a 51% size reduction of a patch antenna is achieved. The concept is verified for both transmitting and receiving front ends and for narrowband and broadband scenarios. It is observed that such approach can improve antenna radiation efficiency and gain by reducing mismatch loss in integrated RF system. Moreover, this co-design approach relaxes antenna matching of miniaturized antennas. The built-in matching network of the RF front-ends takes care of it while co-designed properly.

In addition, port isolation, ultra-wideband operation and improved antenna matching performance are investigated for a MIMO active antenna. Thus, a UWB two-element MIMO antenna geometry is presented. Later, based on the UWB antenna geometry, a two-element active integrated UWB MIMO antenna is implemented. A minimum port isolation improvement of 7 dB is achieved with better antenna matching behavior. MIMO antenna parameters are also examined and well agreement between simulation and measurement results are found.

Considering all the results achieved by simulation and experimental results, it is obvious that the co-design approach adopted in this work can significantly improve antenna matching and can increase port isolation and electrical length of passive antenna (miniaturization). The most important thing is the generic characteristics of the approach i.e. the approach is equally applicable to any structure and in a systematic way which is of ultimate interest in antenna and RF system design. Such approach will help in compact RF system design and can be easily adopted in system-on-chip (SoC) or system-on-package (SoP) realization for antenna miniaturization which is of ultimate interest. This work present the first systematic approach of co-designing antennas and RF amplifiers without 50 Ω requirement. It also shows the miniaturization obtained with such integration along with the first active integrated MIMO antenna system.

7.2 Future Work

The approach of integrating RF-amplifier with antennas can be extended to bandwidth enhancement of miniaturized antennas by non-fostering technique. It should be noted that the non-fostering antennas so far presented in the literature uses NIC for compensating fostered reactance by miniaturized antennas. Thus an extra NIC is required which will consume power for their biasing, space and cost. So, it is ultimate interest if such non-fostering antennas can be developed around RF-amplifier. And, care should be taken considering unstable behavior of such non-fostering antenna system in high frequency applications. Thus, major fundamental limits of passive antennas i.e. size and bandwidth can be taken care of active amplifier integration with more convenience.

REFERENCES

[1] D. Emerson, "The work of Jagadis Chandra Bose: 100 years of millimeter-wave research," *IEEE Transactions on Microwave Theory and Techniques*, vol. 45, no. 12, pp. 2267–2273, 1997.

[2] D. Raychaudhuri and N. B. Mandayam, "Frontiers of wireless and mobile communications," *Proceedings of the IEEE*, vol. 100, no. 4, pp. 824–840, 2012.

[3] A. J. Paulraj, D. A. Gore, R. U. Nabar, and H. Bolcskei, "An overview of mimo communications-a key to gigabit wireless," *Proceedings of the IEEE*, vol. 92, no. 2, pp. 198–218, 2004.

[4] Q. Li, G. Li, W. Lee, M.-i. Lee, D. Mazzarese, B. Clerckx, and Z. Li, "Mimo techniques in wimax and lte: a feature overview," *Communications Magazine, IEEE*, vol. 48, no. 5, pp. 86–92, 2010.

[5] H. A. Wheeler, "Small antennas," *IEEE Transactions on Antennas and Propagation*, vol. 23, no. 4, pp. 462–469, 1975.

[6] J. Lin and T. Itoh, "Active integrated antennas," *IEEE Transactions on Microwave Theory and Techniques*, vol. 42, no. 12, pp. 2186–2194, 1994.

[7] C. W. Pobanz and T. Itoh, "Active integrated antennas," *Potentials, IEEE*, vol. 16, no. 2, pp. 6–10, 1997.

[8] K. Chang, R. A. York, P. S. Hall, and T. Itoh, "Active integrated antennas," *IEEE Transactions on Microwave Theory and Techniques*, vol. 50, no. 3, pp. 937–944, 2002.

[9] M. S. Sharawi, "Printed multi-band mimo antenna systems and their performance metrics," *IEEE Antennas and Propagation Magazine*, no. 55, p. 218, 2013.

[10] B. Razavi, *Design of Analog CMOS Integrated Circuits*, 1st ed. McGraw-Hill Science/Engineering/Math, Aug. 2000.

[11] G. Papotto, F. Carrara, A. Finocchiaro, and G. Palmisano, "A 90-nm cmos 5-mbps crystal-less rf-powered transceiver for wireless sensor network nodes," *Solid-State Circuits, IEEE Journal of*, vol. 49, no. 2, pp. 335–346, 2014.

[12] H. Lakdawala, M. Schaecher, C. Fu, R. Limaye, J. Duster, Y. Tan, A. Balankutty, E. Alpman, C. C. Lee, K. M. Nguyen *et al.*, "A 32 nm soc with dual core atom processor and rf wifi transceiver," *Solid-State Circuits, IEEE Journal of*, vol. 48, no. 1, pp. 91–103, 2013.

[13] M. Naser-Moghadasi, A. Danideh, A. Bakhtiari, and R. Sadeghifakhr, “Compact slot antenna for mimo applications in the wlan bands,” *Microwave and Optical Technology Letters*, vol. 55, no. 10, pp. 2490–2493, 2013.

[14] G. A. Deschamps, “Microstrip microwave antennas,” in *Third USAF symposium on Antennas*, vol. 84, 1953.

[15] M. S. Sharawi, *Printed MIMO Antenna Engineering.* Boston: Artech House, Apr. 2014.

[16] “Simulation of Mobile Phone Antenna Performance.” [Online]. Available: https://www.cst.com/Applications/

[17] C. A. Balanis, *Antenna theory: analysis and design.* John Wiley & Sons, 2012.

[18] S. H. Chae, S.-k. Oh, and S.-O. Park, “Analysis of mutual coupling, correlations, and tarc in wibro mimo array antenna,” *IEEE Antennas and Wireless Propagation Letters*, vol. 6, pp. 122–125, 2007.

[19] M. Manteghi and Y. Rahmat-Samii, “Multiport characteristics of a wideband cavity backed annular patch antenna for multipolarization operations,” *IEEE Transactions on Antennas and Propagation*, vol. 53, no. 1, pp. 466–474, 2005.

[20] S.-W. Su, C.-T. Lee, and F.-S. Chang, “Printed mimo-antenna system using neutralization-line technique for wireless usb-dongle applications,” *IEEE*

Transactions on Antennas and Propagation, vol. 60, no. 2, pp. 456–463, 2012.

[21] K. Rosengren and P.-S. Kildal, "Radiation efficiency, correlation, diversity gain and capacity of a six-monopole antenna array for a mimo system: theory, simulation and measurement in reverberation chamber," in *Microwaves, Antennas and Propagation, IEE Proceedings*, vol. 152, no. 1. IET, 2005, pp. 7–16.

[22] T. Taga, "Analysis for mean effective gain of mobile antennas in land mobile radio environments," *IEEE Transactions on Vehicular Technology*, vol. 39, no. 2, pp. 117–131, 1990.

[23] L. Reinhold and B. Pavel, "Rf circuit design: theory and applications," pp. 463–515, 2000.

[24] T. H. Lee, *The design of CMOS radio-frequency integrated circuits.* Cambridge university press, 2004.

[25] R. C. Li, *RF circuit design.* John Wiley & Sons, 2008, vol. 90.

[26] G. Gonzalez, *Microwave transistor amplifiers: analysis and design.* Prentice-Hall Englewood Cliffs, NJ, 1984, vol. 61.

[27] K. Chang, K. Hummer, and G. Gopalakrishnan, "Active radiating element using fet source integrated with microstrip patch antenna," *Electronics Letters*, vol. 24, no. 21, pp. 1347–1348, 1988.

[28] C.-H. Wu and T.-G. Ma, “Self-oscillating semi-ring active integrated antenna with frequency reconfigurability and voltage-controllability,” *IEEE Transactions on Antennas and Propagation*, vol. 61, no. 7, pp. 3880–3885, 2013.

[29] Y.-Y. Lin, C.-H. Wu, and T.-G. Ma, “Miniaturized self-oscillating annular ring active integrated antennas,” *IEEE Transactions on Antennas and Propagation*, vol. 59, no. 10, pp. 3597–3606, 2011.

[30] Y.-C. Liu and H.-Y. Chang, “Design of a v-band active integrated antenna (aia) with voltage controlled oscillator,” in *Antennas and Propagation Society International Symposium (APSURSI), 2012 IEEE*. IEEE, 2012, pp. 1–2.

[31] C.-H. Wu and T.-G. Ma, “Self-oscillating dual-ring active integrated antenna,” in *Antennas and Propagation (APSURSI), 2011 IEEE International Symposium on*. IEEE, 2011, pp. 2457–2460.

[32] K.-J. Lee, K.-I. Jeon, and Y.-S. Kim, “Aperture-coupled active antenna with push–pull oscillator,” *Electronics letters*, vol. 47, no. 19, pp. 1059–1060, 2011.

[33] G. Ponchak, M. Scardelletti, and J. Jordan, “270 c, 1 ghz oscillator-type active antenna,” *Electronics letters*, vol. 45, no. 8, pp. 386–387, 2009.

[34] G. Yun, “Compact oscillator-type active antenna for uhf rfid reader,” *Electronics Letters*, vol. 43, no. 6, pp. 314–315, 2007.

[35] F. Urbani, F. Bilotti, A. Alu, and L. Vegni, "Vco active integrated antenna with reactive impedance surfaces," *Microwave and optical technology letters*, vol. 47, no. 1, pp. 82–86, 2005.

[36] D.-H. Choi and S.-O. Park, "A varactor-tuned active-integrated antenna using slot antenna," *Antennas and Wireless Propagation Letters, IEEE*, vol. 4, pp. 191–193, 2005.

[37] D. Choi and S. Park, "Active integrated antenna using a t-shaped microstrip coupled-patch antenna," *Microwave and optical technology letters*, vol. 44, no. 5, pp. 434–436, 2005.

[38] D. Bonefačić, J. Bartolić, and Z. Mustić, "Circular active integrated antenna with push-pull oscillator," *Electronics Letters*, vol. 38, no. 21, pp. 1238–1240, 2002.

[39] J. Liu, P. Lu, D. Chang, and C. Chang, "Double-ring active microstrip antenna and self-mixing oscillator in c-band," *IEE Proceedings-Microwaves, Antennas and Propagation*, vol. 147, no. 6, pp. 479–482, 2000.

[40] S. Baek, G.-S. Lee, K. Lee, and Y. Jee, "Multi-band active integrated antenna using clapp oscillator circuit," in *Telecommunication Systems, Services, and Applications (TSSA), 2011 6th International Conference on.* IEEE, 2011, pp. 69–72.

[41] A. Khoshniat and R. Baktur, “A linearly polarized active integrated square microstrip patch antenna,” in *Antennas and Propagation (APSURSI), 2011 IEEE International Symposium on.* IEEE, 2011, pp. 3082–3084.

[42] Y. Qin, S. Gao, and A. Sambell, “Broadband high-efficiency circularly polarized active antenna and array for rf front-end application,” *IEEE Transactions on Microwave Theory and Techniques*, vol. 54, no. 7, pp. 2910–2916, 2006.

[43] A. Genc, T. Turpin, T. Yasin, and R. Baktur, “Active integrated meshed patch antennas for small satellites,” *Microwave and Optical Technology Letters*, vol. 54, no. 7, pp. 1593–1595, 2012.

[44] D. Segovia-Vargas, V. González-Posadas, J. Vazquez, E. Rajo, L. Inclan, and C. Martin, “An active broadband-transmitting patch antenna for gsm-1800 and umts,” *Microwave and optical technology letters*, vol. 41, no. 5, pp. 350–354, 2004.

[45] G. A. Ellis and S. Liw, “Active planar inverted-f antennas for wireless applications,” *IEEE Transactions on Antennas and Propagation*, vol. 51, no. 10, pp. 2899–2906, 2003.

[46] X.-D. Wu and K. Chang, “Integrated active slot dipole antenna amplifier,” *Microwave and Optical Technology Letters*, vol. 6, no. 15, pp. 856–857, 1993.

[47] ——, “Compact wideband integrated active slot antenna amplifier,” *Electronics Letters*, vol. 29, no. 5, pp. 496–497, 1993.

[48] X.-D. Wu, K. Leverich, and K. Chang, "Novel fet active patch antenna," *Electronics letters*, vol. 28, no. 20, pp. 1853–1854, 1992.

[49] H. Kim, I.-J. Yoon, and Y. J. Yoon, "A novel fully integrated transmitter front-end with high power-added efficiency," *IEEE Transactions on Microwave Theory and Techniques*, vol. 53, no. 10, pp. 3206–3214, Oct. 2005.

[50] H.-N. Lin, K.-W. Lin, C.-W. Kuo, and Y.-J. Huang, "Receiving Performance Enhancement of Active GPS Antenna with Periodic Structure," *Session 1P7*, p. 165, Jul. 2013.

[51] A. Dierck, H. Rogier, and F. Declercq, "A Wearable Active Antenna for Global Positioning System and Satellite Phone," *IEEE Transactions on Antennas and Propagation*, vol. 61, no. 2, pp. 532–538, 2013.

[52] Y. Taachouche, F. Colombel, and M. Himdi, "Very Compact and Broadband Active Antenna for VHF Band Applications," *International Journal of Antennas and Propagation*, vol. 2012, Feb. 2012. [Online]. Available: http://www.hindawi.com/journals/ijap/2012/193716/abs/

[53] S. Z. Fan and E. L. Tan, "A low cost omnidirectional high gain active integrated antenna for WLAN applications," 2012, pp. 124–125.

[54] "Active low noise differentially fed dipole antenna," 2012, pp. 290–293.

[55] D. N. Aloi and M. S. Sharawi, "An active tri-band (AMPS/PCS/GPS) antenna with enhanced cellular-to-GPS isolation

for automotive applications," *Microwave and Optical Technology Letters*, vol. 53, no. 8, pp. 1764–1767, 2011. [Online]. Available: http://onlinelibrary.wiley.com/doi/10.1002/mop.26117/abstract

[56] T. Peter, M. Rahim, J. Din, and T. Masri, "Design of low noise amplifier with Active Integrated Antenna at 5 GHz," in *Asia-Pacific Conference on Applied Electromagnetics, 2007. APACE 2007*, Dec. 2007, pp. 1 –5.

[57] D. Charrier and C. Collaboration, "Design of a low noise, wide band, active dipole antenna for a cosmic ray radiodetection experiment," 2007, pp. 4485–4488.

[58] R. Dehbashi, K. Forooraghi, and Z. Atlasbaf, "Active Integrated Antenna Based Rectenna using a New Probe-Fed U-Slot Antenna with Harmonic Rejection," 2006, pp. 2225–2228.

[59] W. Ismail, M. Mustami, and M. Mahadzir, "Gain comparison of low noise active integrated antenna (LNAIA) to the non-active integrated low noise antenna (on-AIA)," 2005, pp. 4 pp.–.

[60] S. Lin, Y. Qian, and T. Itoh, "A low noise active integrated antenna receiver for monopulse radar applications," in *Microwave Symposium Digest, 2001 IEEE MTT-S International*, vol. 2, 2001, pp. 1395–1398.

[61] W. Ismail and P. Gardner, "Low noise integrated active antenna as image reject mixer (IRM)," 2001, pp. 125–129.

[62] C. M. Montiel, L. Fan, and K. Chang, "A novel active antenna with self-mixing and wideband varactor-tuning capabilities for communication and vehicle identification applications," *IEEE Transactions on Microwave Theory and Techniques*, vol. 44, no. 12, pp. 2421–2430, 1996.

[63] M. K. A. Rahim, W. K. Chong, and T. Masri, "Active Integrated Antenna with Image Reject Mixer Design," 2007, pp. 1–4.

[64] A. Nesic, I. Radnovic, V. Brankovic, and D. Nesic, "Active antenna integrated with up converter for 5 to 24 GHz band," vol. 1, 1999, pp. 194–197 vol.1.

[65] ——, "Active antenna integrated with down converter for 24 to 5 GHz bands," vol. 1, pp. 198–201 vol.1.

[66] W. Choi, Changyul-Cheon, and Y. Kwon, "A V-band MMIC Self Oscillating Mixer Active Integrated Antenna Using a Push-Pull Patch Antenna," 2006, pp. 630–633.

[67] J. Tirado-Mendez, H. Jardon-Aguilar, R. Flores-Leal, M. Reyes-Ayala, and E. Andrade-Gonzalez, "Improving performance of non-duplexer active transceiver antenna with defected structures," *Microwaves, Antennas & Propagation, IET*, vol. 4, no. 3, pp. 342–352, 2010.

[68] F. J. Herraiz-Martinez, E. Ugarte-Munoz, V. Gonzalez-Posadas, L. E. Garcia-Munoz, and D. Segovia-Vargas, "Self-diplexed patch antennas based

on metamaterials for active rfid systems," *IEEE Transactions on Microwave Theory and Techniques*, vol. 57, no. 5, pp. 1330–1340, 2009.

[69] M. Rahim, Q. Feng, T. Masri, and M. Karim, "Simultenous transmit and receive circular polarized active integrated antenna," in *Antennas and Propagation, 2007. EuCAP 2007. The Second European Conference on.* IET, 2007, pp. 1–4.

[70] M. Cryan, P. Hall, K. Tsang, and J. Sha, "Integrated active antennas with simultaneous transmit-receive operation," in *Microwave Conference, 1996. 26th European*, vol. 2. IEEE, 1996, pp. 565–568.

[71] S. Sussman-Fort and R. Rudish, "Non-Foster Impedance Matching of Electrically-Small Antennas," *IEEE Transactions on Antennas and Propagation*, vol. 57, no. 8, pp. 2230–2241, Aug. 2009.

[72] J. Linvill, "Transistor Negative-Impedance Converters," *Proceedings of the IRE*, vol. 41, no. 6, pp. 725–729, Jun. 1953.

[73] C. White, J. Colburn, and R. Nagele, "A Non-Foster VHF Monopole Antenna," *IEEE Antennas and Wireless Propagation Letters*, vol. 11, pp. 584–587, 2012.

[74] N. Zhu and R. W. Ziolkowski, "Design and measurements of an electrically small, broad bandwidth, non-Foster circuit-augmented protractor antenna," *Applied Physics Letters*, vol.

101, no. 2, p. 024107, Jul. 2012. [Online]. Available: http://scitation.aip.org/content/aip/journal/apl/101/2/10.1063/1.4736996

[75] ——, "Broad-Bandwidth, Electrically Small Antenna Augmented With an Internal Non-Foster Element," vol. 11, pp. 1116–1120, 2012.

[76] M. N. Alam, R. A. Dougal, and M. Ali, "Electrically Small Broadband VHF/UHF Planar Antenna Matched Using a Non-Foster Circuit," *Microwave and Optical Technology Letters*, vol. 55, no. 10, pp. 2494–2497, Oct. 2013. [Online]. Available: http://onlinelibrary.wiley.com/doi/10.1002/mop.27818/abstract

[77] H. Mirzaei and G. Eleftheriades, "A Resonant Printed Monopole Antenna With an Embedded Non-Foster Matching Network," *IEEE Transactions on Antennas and Propagation*, vol. 61, no. 11, pp. 5363–5371, Nov. 2013.

[78] M.-C. Tang, N. Zhu, and R. Ziolkowski, "Augmenting a Modified Egyptian Axe Dipole Antenna With Non-Foster Elements to Enlarge Its Directivity Bandwidth," *IEEE Antennas and Wireless Propagation Letters*, vol. 12, pp. 421–424, 2013.

[79] A. Petosa, "An overview of tuning techniques for frequency-agile antennas," *Antennas and Propagation Magazine, IEEE*, vol. 54, no. 5, pp. 271–296, 2012.

[80] A. Sheta and S. F. Mahmoud, "A widely tunable compact patch antenna," *Antennas and Wireless Propagation Letters, IEEE*, vol. 7, pp. 40–42, 2008.

[81] D. Peroulis, K. Sarabandi, and L. P. Katehi, “Design of reconfigurable slot antennas,” *IEEE Transactions on Antennas and Propagation*, vol. 53, no. 2, pp. 645–654, 2005.

[82] N. C. Karmakar, “Shorting strap tunable stacked patch pifa,” *IEEE Transactions on Antennas and Propagation*, vol. 52, no. 11, pp. 2877–2884, 2004.

[83] J.-M. Laheurte, “Switchable cpw-fed slot antenna for multifrequency operation,” *Electronics letters*, vol. 37, no. 25, pp. 1498–1500, 2001.

[84] C. Luxey, L. Dussopt, J.-L. Le Sonn, and J.-M. Laheurte, “Dual-frequency operation of cpw-fed antenna controlled by pin diodes,” *Electronics letters*, vol. 36, no. 1, pp. 2–3, 2000.

[85] M. Abdallah, L. Le Coq, F. Colombel, G. Le Ray, and M. Himdi, “Frequency tunable monopole coupled loop antenna with broadside radiation pattern,” *Electronics letters*, vol. 45, no. 23, pp. 1149–1151, 2009.

[86] A. Gautam, “A frequency agile active microstrip antenna for cp operation,” *Microwave and Optical Technology Letters*, vol. 54, no. 9, pp. 2205–2209, 2012.

[87] Z. Wu, Q. Feng, and S. Liu, “A tunable internal antenna based on composite right/left handed transmission line for mobile handset application,” in *Wireless And Optical Communications Networks (WOCN), 2010 Seventh International Conference On.* IEEE, 2010, pp. 1–4.

[88] G. Jin, D. Zhang, and R. Li, “Optically controlled reconfigurable antenna for cognitive radio applications,” *Electronics letters*, vol. 47, no. 17, pp. 948–950, 2011.

[89] R. N. Lavallee and B. A. Lail, “Optically-controlled reconfigurable microstrip patch antenna,” in *Antennas and Propagation Society International Symposium, 2008. AP-S 2008. IEEE.* IEEE, 2008, pp. 1–4.

[90] S. Gao, A. Sambell, and S. Zhong, “Polarization-agile antennas,” *Antennas and Propagation Magazine, IEEE*, vol. 48, no. 3, pp. 28–37, 2006.

[91] S.-X. Cao, X.-X. Yang, B. Gong, and B.-C. Shao, “A reconfigurable microstrip antenna with agile polarization using diode switches,” in *Antennas and Propagation (APSURSI), 2011 IEEE International Symposium on.* IEEE, 2011, pp. 1566–1569.

[92] C. Vazquez, S. Hoeye, M. Fernandez, G. Leon, L. F. Herran, and F. Las Heras, “Receiving polarization agile active antenna based on injection locked harmonic self oscillating mixers,” *IEEE Transactions on Antennas and Propagation*, vol. 58, no. 3, pp. 683–689, 2010.

[93] V. Hoeye, L. Heras *et al.*, “Novel polarization agile microstrip antenna,” in *2008 IEEE Antennas and Propagation Society International Symposium*, 2008, pp. 1–4.

[94] X.-X. Yang, S.-S. Zhong, and S.-C. Gao, “A novel polarization-agile active microstrip antenna array with lna,” in *Antennas, Propagation and EM*

Theory, 2000. Proceedings. ISAPE 2000. 5th International Symposium on. IEEE, 2000, pp. 94–97.

[95] P. Haskins, J. Dahele, I. Merrow, and P. Hall, “Active polarization-agile microstrip patch antennas,” in *Antennas and Propagation, 1995., Ninth International Conference on (Conf. Publ. No. 407).* IET, 1995, pp. 163–165.

[96] B. Yarman, “A simplified real frequency technique for broad-band matching a complex generator to a complex load,” *RCA review*, vol. 43, no. 3, pp. 529–541, 1982.

[97] ——, “A dynamic cad technique for designing broadband microwave amplifiers,” *RCA review*, vol. 44, no. 4, pp. 551–565, 1983.

[98] ——, “Modern approaches to broadband matching problems,” in *IEE Proceedings H (Microwaves, Antennas and Propagation)*, vol. 132, no. 2. IET, 1985, pp. 87–92.

[99] B. S. Yarman, “Design of ultra wideband antenna matching networks,” in *Proceeding applied electromagnetics conference, IEEE Press, Kolkata, India.* Springer, 2007, pp. 1–4.

[100] ——, *Design of ultra wideband power transfer networks.* John Wiley & Sons, 2010.

[101] R. Garg, *Microstrip antenna design handbook.* Artech House, 2001.

[102] H. W. Bode, *Network analysis and feedback amplifier design.* D. van Nostrand New York, 1945.

[103] R. M. Fano, “Theoretical limitations on the broadband matching of arbitrary impedances,” *Journal of the Franklin Institute*, vol. 249, no. 1, pp. 57–83, 1950.

[104] J. Volakis, C.-C. Chen, and K. Fujimoto, *Small Antennas:Miniaturization Techniques & Applications*, 1st ed. New York: McGraw-Hill Professional, Jun. 2010.

[105] B. Sklar, *Digital Communications: Fundamentals and Applications*, 2nd ed. Upper Saddle River, N.J: Prentice Hall, Jan. 2001.

[106] Y. Wang and Z. Du, “A wideband printed dual-antenna with three neutralization lines for mobile terminals,” *IEEE Transactions on Antennas and Propagation*, vol. 62, no. 3, pp. 1495–1500, 2014.

[107] A. Toktas and A. Akdagli, “Wideband mimo antenna with enhanced isolation for lte, wimax and wlan mobile handsets,” *Electronics Letters*, vol. 50, no. 10, pp. 723–724, 2014.

[108] C. H. See, R. A. Abd-Alhameed, Z. Z. Abidin, N. J. McEwan, and P. S. Excell, “Wideband printed mimo/diversity monopole antenna for wifi/wimax applications,” *IEEE Transactions on Antennas and Propagation*, vol. 60, no. 4, pp. 2028–2035, 2012.

[109] T. Tang and K. Lin, “An ultrawideband mimo antenna with dual band-notched function,” 2014.

[110] J.-F. Li, Q.-X. Chu, Z.-H. Li, and X.-X. Xia, “Compact dual band-notched uwb mimo antenna with high isolation,” *IEEE Transactions on Antennas and Propagation*, vol. 61, no. 9, pp. 4759–4766, 2013.

[111] S. Mohammad, H. R. Hassani, A. Foudazi *et al.*, “A dual-band wlan/uwb printed wide slot antenna for mimo/diversity applications,” *Microwave and Optical Technology Letters*, vol. 55, no. 3, pp. 461–465, 2013.

[112] J.-M. Lee, K.-B. Kim, H.-K. Ryu, and J.-M. Woo, “A compact ultrawideband mimo antenna with wlan band-rejected operation for mobile devices,” *Antennas and Wireless Propagation Letters, IEEE*, vol. 11, pp. 990–993, 2012.

Vitae

- Name: Sagar Kumar Dhar
- Nationality: Bangladeshi
- Date of Birth: 01 December, 1986
- Email: *sagar378@gmail.com; sagar378@ieee.org*
- Permenant Address: Chittagong, Bangladesh.

- BSc. in Electrical and Electronic Engineering, Chittagong University of Engineering and Technology, Bangladesh.

PUBLICATIONS

Patent

1. M. S. Sharawi and S. K. Dhar, *Active Integrated MIMO Antennas*, Filed on April 2014 to USPO, Patent Pending.

Journal Papers

1. S. K. Dhar, M. S. Sharawi, O. Hammi and F. M. Ghannouchi, *An Active Integrated Ultra-Wideband MIMO Antenna*, To be Submitted to IEEE Transactions on Antennas and Propagation, March, 2015.
2. S. K. Dhar and M. S. Sharawi, *A UWB Semi-Ring MIMO Antenna with Isolation Enhancement*, Submitted, Microwave and Optical Technology Letters, Jan, 2015.
3. M. S. Sharawi, S. K. Dhar, O. Hammi and F. M. Ghannouchi, *Miniaturized Active Integrated Antennas: A Co-Design Approach*, Submitted to IEEE Transactions on Antennas and Propagation, Jan, 2015.
4. S. K. Dhar, M. S. Sharawi and K. Sarabandi, *A Compact Isolation Enhanced Dual Semi-Ring Multiband MIMO Antenna*, Submitted, IET Microwaves, Antennas and Propagation, Dec, 2014.

Conference Papers

1. S. K. Dhar, M. S. Sharawi and F. M. Ghannouchi, *Port Isolation Enhancement via Active Integration for a UWB MIMO Antenna System*, Accepted, IEEE International Symposium on Antennas and Propagation (APS), 2015.

2. S. K. Dhar and M. S. Sharawi, *An Isolation Enhanced Ultra-Wideband Semi-Ring Monopole MIMO Antenna*, Accepted, IEEE International Symposium on Antennas and Propagation (APS), 2015.

3. S. K. Dhar, O. Hammi, M. S. Sharawi and F. M. Ghannouchi, *Power Amplifier Based Integrated and Miniaturized Active Antenna*, Accepted, European Conference on Antennas and Propagation (EuCAP), 2015.

4. S. K. Dhar and M. S. Sharawi, *A Multi-band Isolation Enhanced Loaded Semi-Ring MIMO Antenna*, European Microwave Conference (EuMC), 2014.

5. S. K. Dhar and M. S. Sharawi, *A Multi-band Loaded Semi-ring MIMO Antenna*, IEEE Int. Symposium on Antennas and Propagation (APS), 2014.